



New concepts to control the load along the span of the blade, passive, active or mixed

Agreement n.:	308974
Duration	November 2012 – October 2017
Co-ordinator:	DTU Wind

Support by:



PROPRIETARY RIGHTS STATEMENT

This document contains information, which is proprietary to the "INNWIND.EU" Consortium. Neither this document nor the information contained herein shall be used, duplicated or communicated by any means to any third party, in whole or in parts, except with prior written consent of the "INNWIND.EU" consortium.

Document information

Document Name:	New concepts to control the load along the span of the blade, passive, active or mixed
Document Number:	Deliverable D2.3.1
Author:	Carlo L. Bottasso (POLIMI), Alessandro Croce (POLIMI), Federico Gualdoni (POLIMI), Pierluigi Montinari (POLIMI), Vasilis Riziotis (NTUA), Spyros Voutsinas (NTUA) Karakala Anargyros (UPAT), Dimitris Saravanos (UPAT), Christian Pavese (DTU), Jan-Willem van Wingerden (DUT)
Document Type	Report
Dissemination level	PU
Review:	Flemming Rasmussen (DTU)
Date:	14-8-2015
WP:	2
Task:	3
Approval:	Approved by WP Leader

EXECUTIVE SUMMARY

The objective of WP 2.3 is to improve the technology of distributed load control to a level where it can be demonstrated in real atmospheric conditions on medium size turbines before the final step of application to very large turbines. In this deliverable, the first step is taken and novel active and passive load alleviation concepts are investigated.

In this first step we will establish a framework for exploration of the passive built-in structural couplings and an evaluation of what couplings would be beneficial. This is done by aeroelastic simulations on a wind turbine modified to include such couplings. The result is an overview of the perspectives and requirements for the structural design concerning the extent of couplings and e.g. morphing needed to achieve the beneficial overall characteristics. In parallel, aeroelastic simulations are performed of active control methodologies using novel controllers. In consecutive steps (D.2.3.2 and D.2.3.3) these passive load control and/or existing control systems (e.g. Individual Pitch Control) will be combined with active distributed load control to investigate the compatibility of different configurations.

In this deliverable, three different concepts are presented to control the load along the span of the blade. Some of the concepts have been introduced in previous EU projects and national project (e.g. UPWIND). However, the objective of this deliverable is to look at the technical feasibility and readiness of the different concepts and to quantify and compare the load reduction potential. The three concepts are listed below:

1. SMA morphing wing concept, in which Shape Memory Alloys are actively controlled to change the shape of the airfoil to reduce the variations in the aerodynamic forces that act on the airfoil.
2. Passive flap concept, in which the aerodynamic force itself is used to change the shape of the airfoil to reduce the variations in the aerodynamic forces that act on the airfoil.
3. Geometric and material coupling concepts in which passive control methods are regulated in order to obtain predefined loads on the wind turbine

If we look at the SMA morphing wing concept, we can conclude that the technical feasibility is promising. In this deliverable, technical solutions are proposed to increase the fatigue life-time and the bandwidth of the SMA actuator, which are critical technical breakthroughs required to make this concept feasible.

For the passive flap concept we can conclude that this is a novel concept by itself and the preliminary analysis conducted so far on a simplified model shows potential in the reduction of the loads on the rotor. High-fidelity simulations have to be performed to fully prove the concept and one or more technical solutions have to be found to develop a working prototype.

Material and geometric coupling concepts have already shown their potential as a concept. In this deliverable, technical design guidelines are introduced to enhance the technological readiness. The analysis carried out confirmed the potential of this passive

control strategy. Improvements to the optimization framework and to the comparison between the different configurations of the wind turbine used for the simulations must be introduced to further mature the concept.

Although the load reduction capabilities of the three concepts seem to be promising, it is believed that a combination of the different concepts will further significantly increase the design space to shape and alleviate the loads. We can also conclude that for the different concepts different readiness levels can be identified and, due to that, it is believed that it is not possible yet to, in a fair manner, compare the load reduction capabilities of the different concepts.

In the upcoming years, high fidelity simulations will be performed of several different combinations such as:

- Morphing+Individual Pitch Control
- Geometric coupling +Individual Pitch Control
- Material coupling + Individual Pitch Control

This will also enable us to quantify and compare the load reduction capabilities of the different concepts. The results of that study will be reported in D. 2.3.2 and the most promising concepts will be tested on wind tunnel prototypes (D.2.3.3).

TABLE OF CONTENTS

EXECUTIVE SUMMARY	5
1 INTRODUCTION.....	9
2 CONCEPT 1: SMA MORPHING WING CONCEPT	11
2.1 Description of the concept	11
2.2 Actuators and Simulation Procedures	11
2.3 Results.....	51
2.4 Conclusions/Outlook	58
2.5 References	59
3 CONCEPT 2: PASSIVE FLAP SYSTEM CONCEPT.....	61
3.1 Introduction	61
3.2 Description of the concept	62
3.3 Results.....	68
3.4 Conclusions	79
3.5 References	79
4 CONCEPT 3: GEOMETRIC AND MATERIAL COUPLING CONCEPTS.....	82
4.1 Introduction	82
4.2 Description of the concept	83
4.3 Model Description	84
4.4 Results.....	87
4.5 Conclusions/Outlook	111
4.6 References	112
5 CONCLUSIONS.....	114

1 INTRODUCTION

Offshore wind turbines are the largest rotating machines on earth, with the length of one blade almost equal to the entire span of a Boeing 747. As the dimensions of these machines keep increasing, the necessity of controlling costs related to production and maintenance becomes a key concern during their design process. Central among the requirements are the capabilities to mitigate the loading on the structure, maximizing wind yield and energy output. To match this requirement, the aim is to reduce the aerodynamic loads acting on the blades through the employment of more sophisticated control strategies. For example, aerodynamic devices like flaps had been developed by the aerospace industry in order to enhance load control potential on aircrafts. Development of similar devices and other control methods by the wind energy research is hence considered a natural outcome to fulfill the necessity of handling and regulating the larger loads acting on wind turbine structures of increasing sizes.

State of the art for wind energy technologies are pitch-controlled variable-speed machines. As previously mentioned, the design of larger rotors translate in handling increasing loads on the full wind turbine structure. Two possible paths can be followed: use the actual control technologies creating a generally heavier structure with consequent large increase in production related costs; develop new control technologies able to alleviate and better regulate the loading according to need, with the possibility of designing a machine with lighter blades and a guaranteed life-time of 20 years.

This report analyzes new approaches for alternative control methods to achieve load mitigations on wind turbines, highlighting the direction to bring these new strategies from concept to technology.

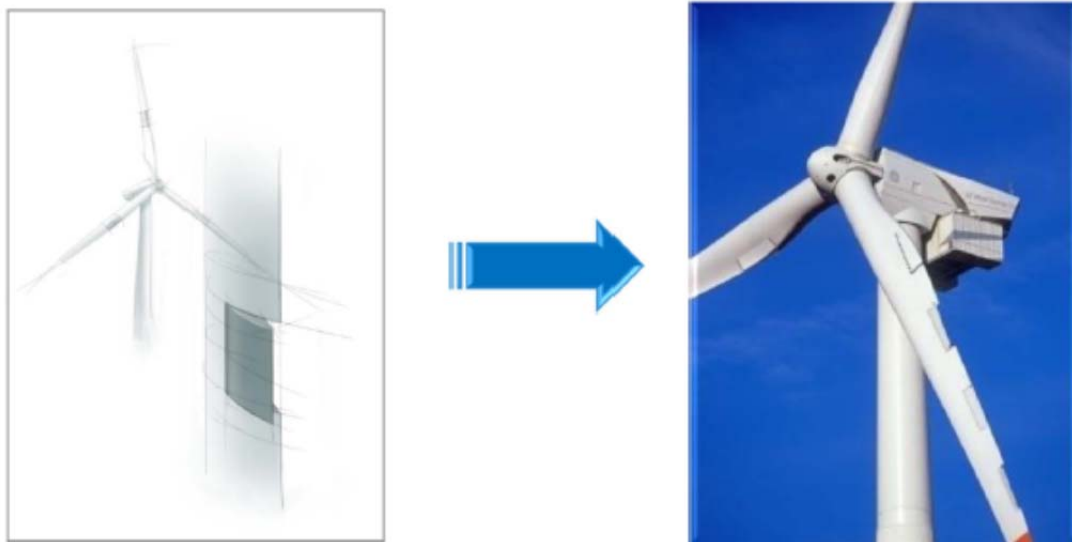


Figure 1, from concept to technology

Wind turbine control methods can be divided in two broad categories: active, when the machine is actively controlled through the automated assistance of actuators or aerodynamic devices; passive, when the control is embedded in designing a structure that achieves load reduction when loaded during operation.

Active and passive load mitigations solutions were proposed in the UPWIND project. Within this project and several national projects these concepts have shown great potential in achieving load reductions. Aiming to the design of a light weight rotor, the INNWIND project proposes the exploitation of the combination of different control methods concepts. In the deliverable 2.3.1, these control methods concepts, some of them already object of extensive academic research, are investigated using novel approaches. These new angles given to the analysis of these load control solutions have the final purpose to draw a route to bring these concepts towards the creation of new technologies to be implemented on real machines, with consequent benefit for the wind energy research.

In this deliverable the following four distinct technologies will be presented:

1. SMA morphing wing concept, in which Shape Memory Alloys are actively controlled to change the shape of the airfoil to reduce the variations in the aerodynamic forces that act on the airfoil.
2. Passive flap concept, in which the aerodynamic forces itself are used to change the shape of the airfoil to reduce the variations in the aerodynamic forces that act on the airfoil.
3. Geometric and material coupling concepts in which passive control methods are regulated in order to obtain predefined loads on the wind turbine

Each of the reported concepts has a dedicated chapter, in which the concept is described and positive and negative effects highlighted and discussed. In the final chapter, conclusions and outlook are reported.

2 CONCEPT 1: SMA MORPHING WING CONCEPT

2.1 Description of the concept

In this chapter a systematic effort for load alleviation of horizontal axis wind turbine blades (WTB) using shape morphing techniques is described. The load alleviation is based on the development of wind turbine blade sections capable of drastically varying their curvature with time. Morphing is considered as the ability of a structure to undergo pronounced geometry adaptations to optimally and timely respond to a variety of operational conditions. It is a bio-mimetic approach and has been identified as a disruptive future technology for maximizing efficiency of lightweight structures. Shape Memory Alloy (SMA) actuators are utilized for adapting the airfoil shape of a wind turbine blade section.

The present work is mainly focused on the design and evaluation of a trailing edge (TE) morphing mechanism and the corresponding control loop. Wind causes time varying loads on the blades thus, morphing of the airfoil's shape with respect to the wind is crucial for dynamic load alleviation. The aim of control loop presented herein is the reduction of the blade fatigue loads in normal operation. A feed-back control loop has been designed that receives input from either a load sensor (strain gauge) at the root of the blade or an acceleration sensor (accelerometer) at the blade tip. Particularly challenging was the selection of the appropriate filter that smoothes out high frequency fluctuation of the control signal that the SMA actuators cannot easily follow. Whereas a certain degree of adaptivity of the airfoil shape can be accomplished conventionally by means of mechanical systems (such as flaps moved via electric motors), solid-state systems without massive moving parts allow for substantial reversible deformability exhibiting far more potential as morphing strategy. Moving in this direction, a morphing blade section with an articulated trailing edge rib structure was designed and assessed. Skin continuity can be achieved by flexible material selection for specific skin regions.

2.2 Actuators and Simulation Procedures

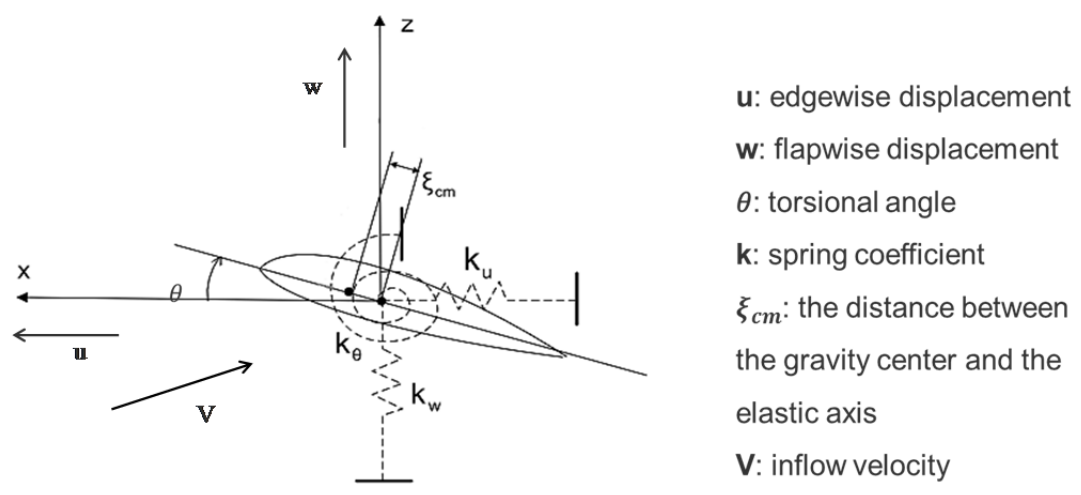
Aeroelastic analysis of a typical blade section with a moving TE flap

The aeroelastic analysis of the blade is performed in the context of the typical 2D elastically mounted section. The aerodynamic characteristics of the deformable blade section are calculated using a 2D free wake viscous-inviscid interaction code [1] while the structural response of the blade is simulated using concentrated spring properties in the flapwise, chordwise and torsional direction of motion respectively [2] as shown in Figure 2.

The whole analysis is performed for the Reference 10 MW Innwind.eu Rotor. As typical blade section, the 75% ($r=65.75$ m) section is considered. At the radial station of 75% distributed aerodynamic loads are expected to obtain their maximum value. The particular section has chord $c=3.398$ m, linear mass $m=221.8$ kg/m. The spring constants of the elastic model are then tuned so as the flapwise and edgewise natural frequencies of the blade $f_{FL} = 0.62$ Hz and $f_{ED} = 0.94$ Hz respectively are reproduced.

Torsion d.o.f. is suppressed (k_{θ} very high). A critical structural damping ratio of 0.5% is used in both bending directions. Simulations are performed for the FFAW3241 airfoil that lies in the outer part of the Reference Innwind Rotor.

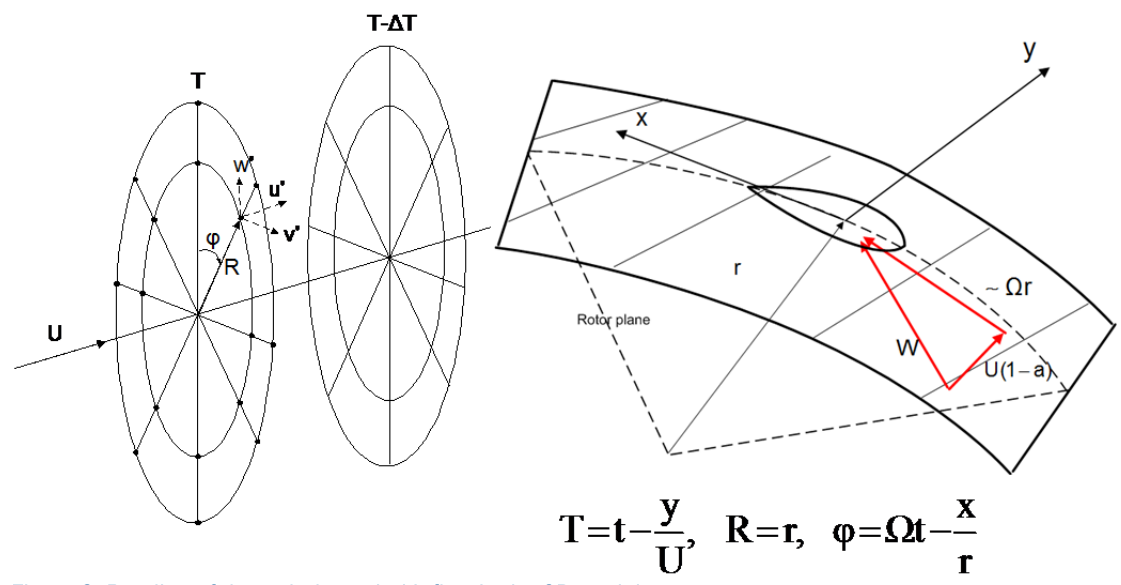
Validation of the control strategies in terms of the load reduction is performed for the wind speed of 10 m/s (below the rated speed but very close to it). At this wind speed the rotor operates at the maximum (rated) rotational speed of 9.6 rpm and the pitch is fixed to 0°.



Structural model with 3 d.o.f.

Figure 2: Typical 2D blade section model for the aeroelastic analysis of the blade.

The reading of the turbulent wind in the 2D aerodynamic model is illustrated in Figure 3. The turbulent wind is computed over a polar grid R, φ at every time instant T . The coordinates R, φ and T are then transformed into x, y co-ordinates of the 2D plane following the expressions presented in Figure 3.



$$T = t - \frac{y}{U}, \quad R = r, \quad \varphi = \Omega t - \frac{x}{r}$$

Figure 3: Reading of the turbulent wind inflow in the 2D model.

Control loop design parameters

The deformable TE flap control loop is illustrated in Figure 4.

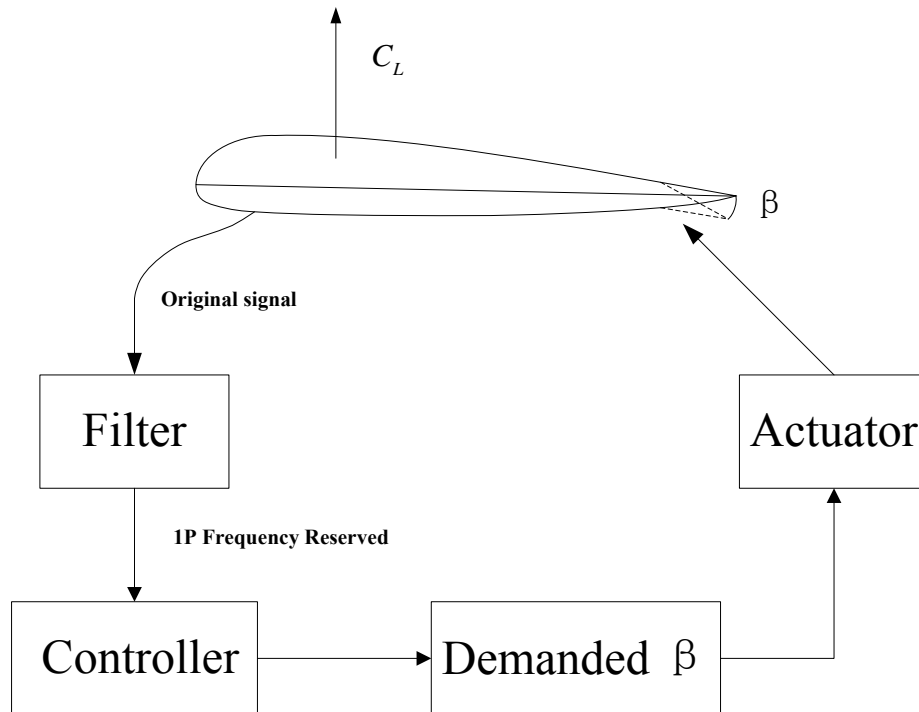


Figure 4: Control loop block diagram.

The input signal (load or acceleration) is first filtered. Several fourth order **elliptic** bandpass or lowpass filters have been tested in the present analysis. The main driver for the selection of the filter parameters (passband ripple, stopband attenuation, band range or edge frequency for lowpass filters etc.) is the response speed of the SMA system. This is found to be relatively low especially during the cooling phase. The aim of the filter is to maintain at least the 1P frequency (0.16 Hz in the present case) which mainly drives blade fatigue loads as shown in Figure 4. In the figure the axial wind component in the hub fixed and the rotating frame are presented. A 1P (6.25 s period) variation is identified in the rotational sampled wind signal that will be also reflected on blade loads and accelerations. Other important requirements of the filter are (a) a small phase shift with respect to the input signal at the frequency of 1P (b) the lowest possible attenuation of the 1P variation.

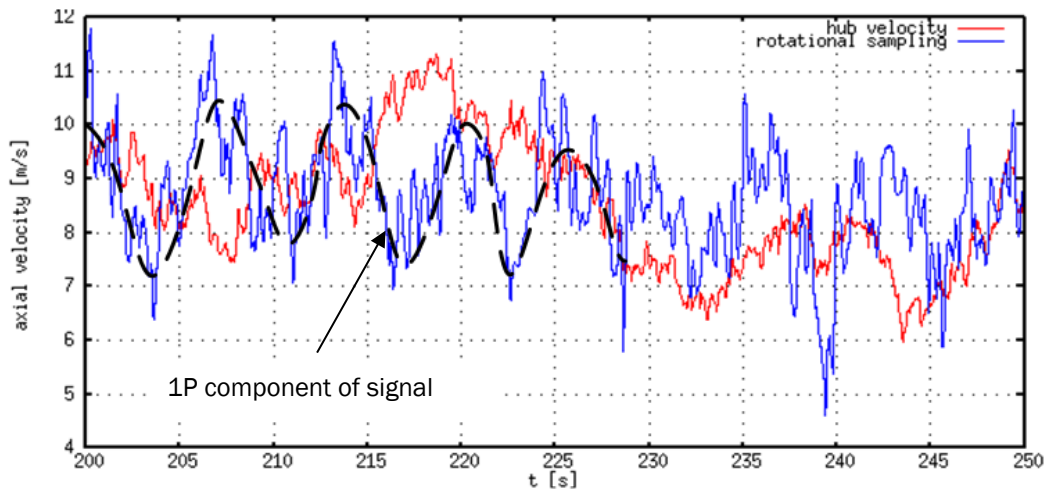


Figure 5: Filtering of the input signal.

The amplitude and phase plots, as well as the state space form of a bandpass filter used in the present analysis are shown in Figure 6 and in the tables below. It corresponds to an elliptic fourth order bandpass filter with a bandpass range of 0.1 Hz [0.11-0.21 Hz], passband ripple $R_p=3$ dB and stopband attenuation $R_s=50$ dB.

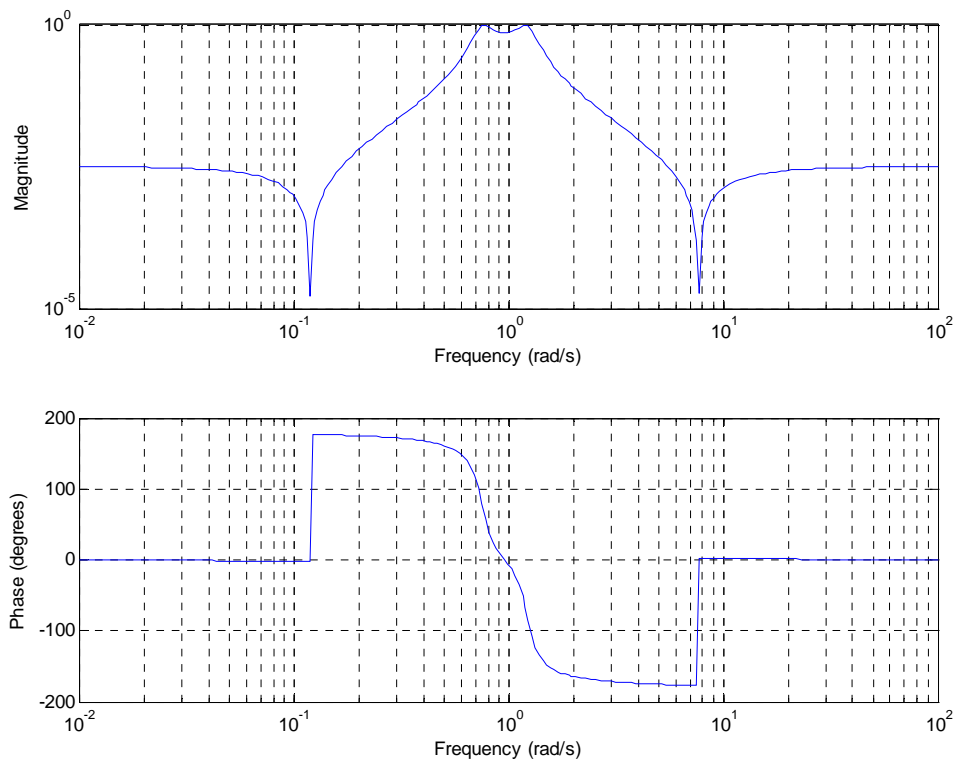


Figure 6: Bode plots of a bandpass filter 0.11-0.21 Hz.

The state-space A,B,C,D matrices of the filter are:

A			
-0.3861	-0.5056	-0.9539	0
0.5056	0	0	0.9539

-0.9539	0	0	0
0	-0.9539	0	0

B
0.6000
0
0
0

C			
-0.0020	0.5939	0	0

D
0.0032

In Figure 7 the output of the filter in a test (flapwise deflection) input is shown.

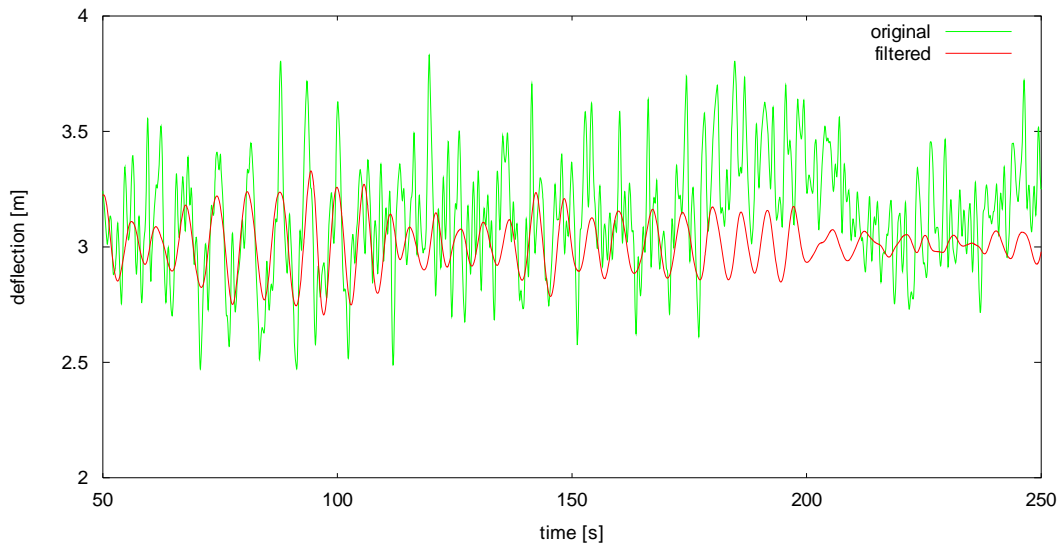


Figure 7: Example of a bandpass filtered signal.

The amplitude and phase plots, as well as the state space form of a lowpass filter used in the present analysis are shown in Figure 8 and in the tables below. It corresponds to an elliptic fourth order lowpass filter with a pass frequency of 0.3 Hz, passband ripple $R_p=1$ dB and stopband attenuation $R_s=10$ dB.

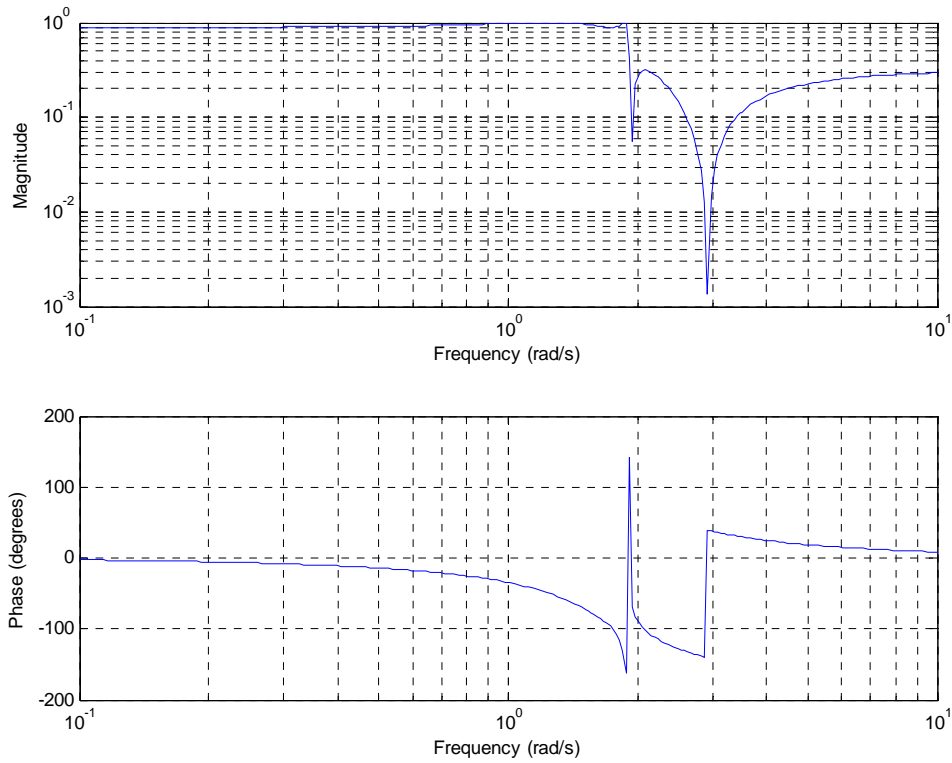


Figure 8: Bode plots of a lowpass filter 0.3 Hz.

The state-space A,B,C,D matrices of the filter are:

A			
-1.4022	-1.7737	0	0
1.7737	0	0	0
-1.4022	3.0057	-0.0653	-1.8981
0	0	1.8981	0

B
1.8900
0
1.8900
0

C			
-0.2346	0.5029	-0.0109	0.0146

D
0.3162

In Figure 9 the output of the filter in a test (flapwise deflection) input is shown.

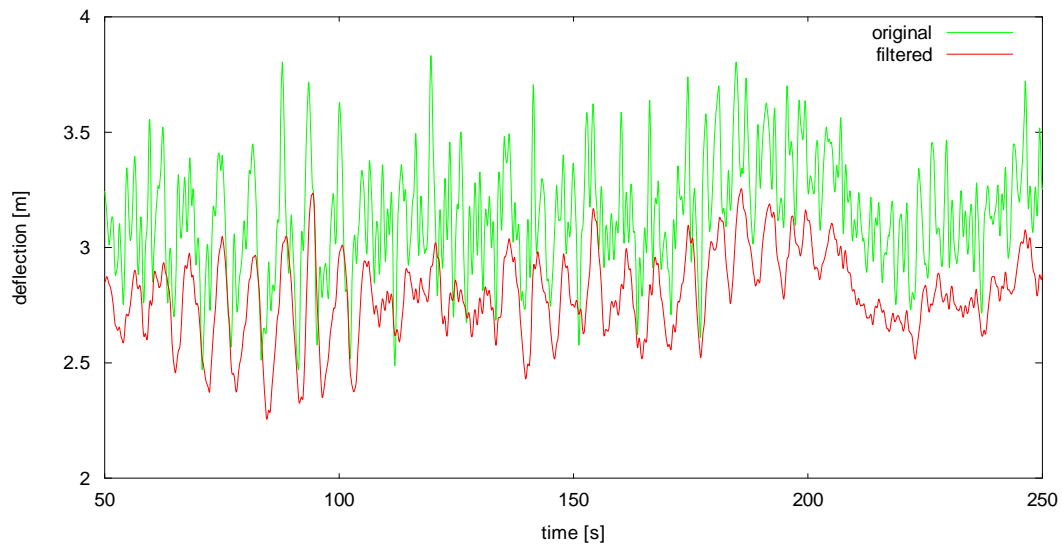
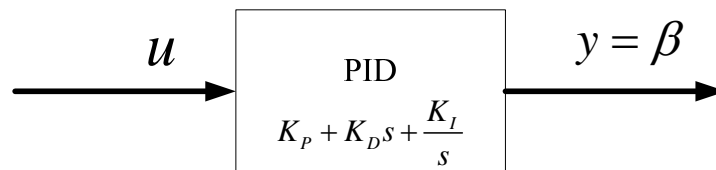


Figure 9: Example of a lowpass filtered signal.

The filtered input signal passes through a linear control element PI or PD depending on the sensor used. The acceleration signal has a zero mean so it can be used in conjunction with a PI controller while the load input can be combined with a PD controller. Thereby, the demand flap angle is determined.



In the next paragraph results from the application of the PI controller that takes as input the acceleration signal measured at the tip of the blade are presented. The latter approach was found to be more efficient in terms of load reduction when the smoothing of the input signal is high.

Control loop application results

Acceleration sensor – PI controller – 30% flap extension

In the present section results of the PI controller (input acceleration signal) are presented for various filters. In all simulations a shear exponent of 0.2 and a yaw error of 5° was considered. Also in all simulations the delay in the response of the actuator is considered negligible.

No filter

In Figure 10 the time series of the flap deflection is presented for an integral gain $k_i=0.05$. The results of the TE flap control simulation are compared against the baseline results of the uncontrolled case.

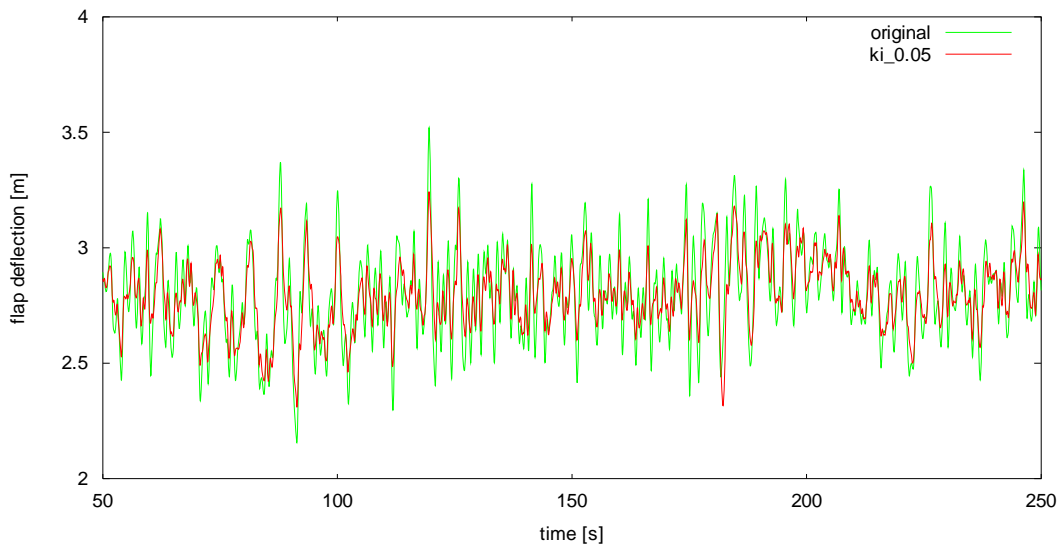


Figure 10: Time series of flap deflection for $k_i=0.05$.

A **27% reduction** on the equivalent fatigue load (1 Hz, $m=12$) is achieved when the input signal is not filtered. In Figure 11 the time series of the flap demand angle is presented. The range of variation of the flap angle is not that high in the case of a 30% flap extension however the speed of the flap motion is higher than 20 deg/s (not shown in the plots).

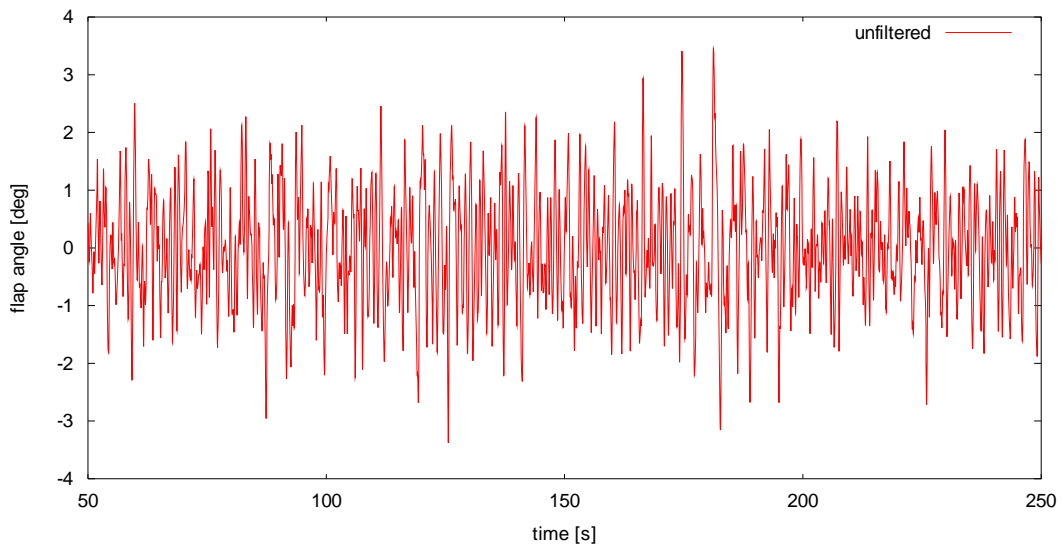


Figure 11: Time series of flap demand angle for $k_i=0.05$.

bandpass filter [0.11 – 0.21 Hz]

In this section results of the PI controller that takes as input a bandpassed filtered signal of the acceleration (bandpass range of 0.1 Hz [0.11-0.21 Hz], passband ripple $R_p=3$ dB and stopband attenuation $R_s=50$ dB) are shown. In Figure 12 the time series of the flap deflection is presented for an integral gain $k_i=0.10$. The results of the TE flap control simulation are compared against the baseline results of the uncontrolled case.

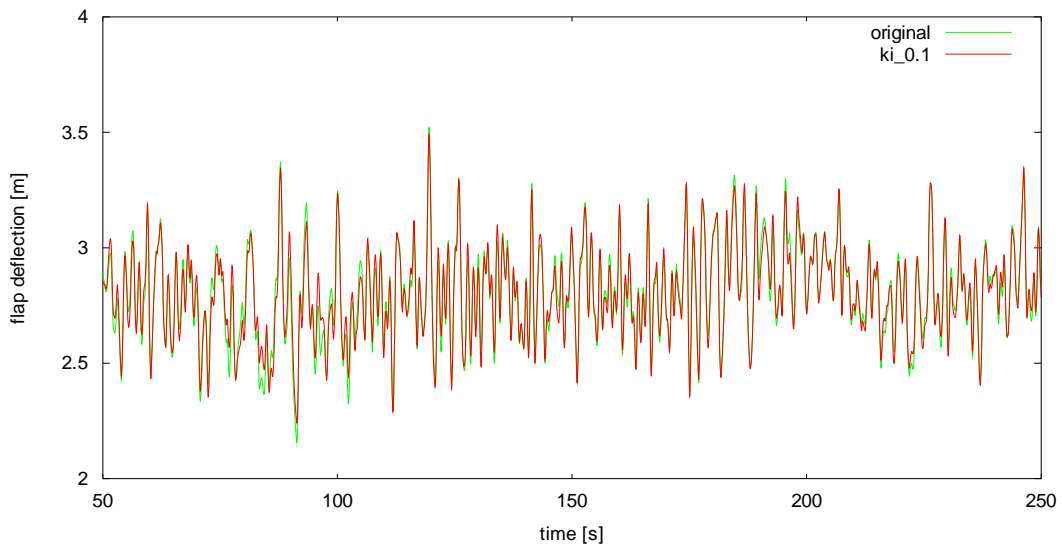


Figure 12: Time series of flap deflection for $k_i=0.10$.

A **6% reduction** in the load is obtained in this case, much lower than in the unfiltered case. In Figure 13 the time series of the flap demand angle is compared against the unfiltered case. It is seen that the range of variation is considerably reduced (about 1deg in absolute value) while the high frequency fluctuations almost vanish. The angular speed of the flap motion is not higher than **1.5 deg/s** in this case.

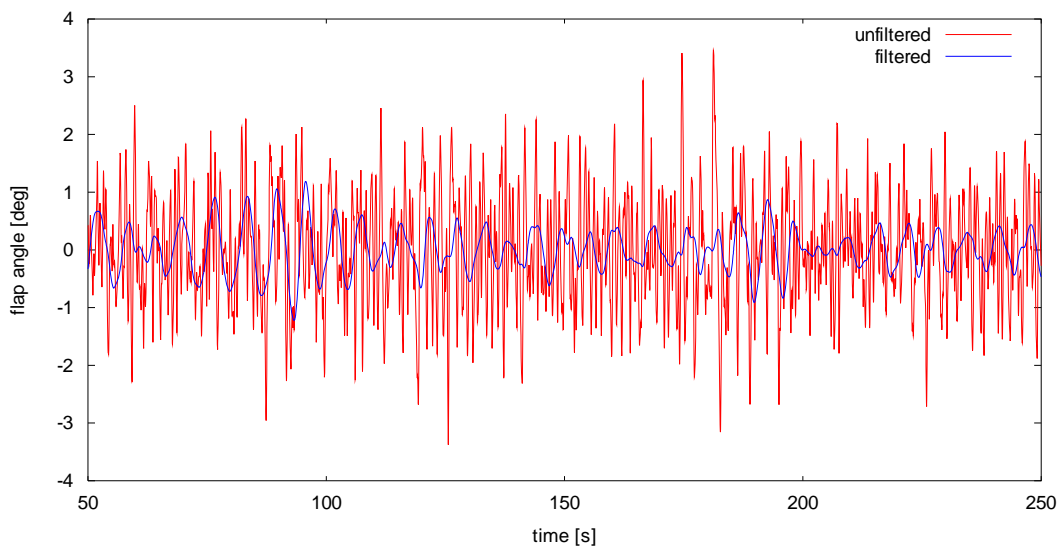


Figure 13: Time series of flap demand angle for $k_i=0.10$.

A fine tuning of the PI gains can give a marginally higher load reduction. In Figure 14 the time series of the flap deflection is presented for the gain values $k_p=0.05 \text{ deg s}^2/\text{m}$, $k_i=0.20 \text{ deg s}/\text{m}$.

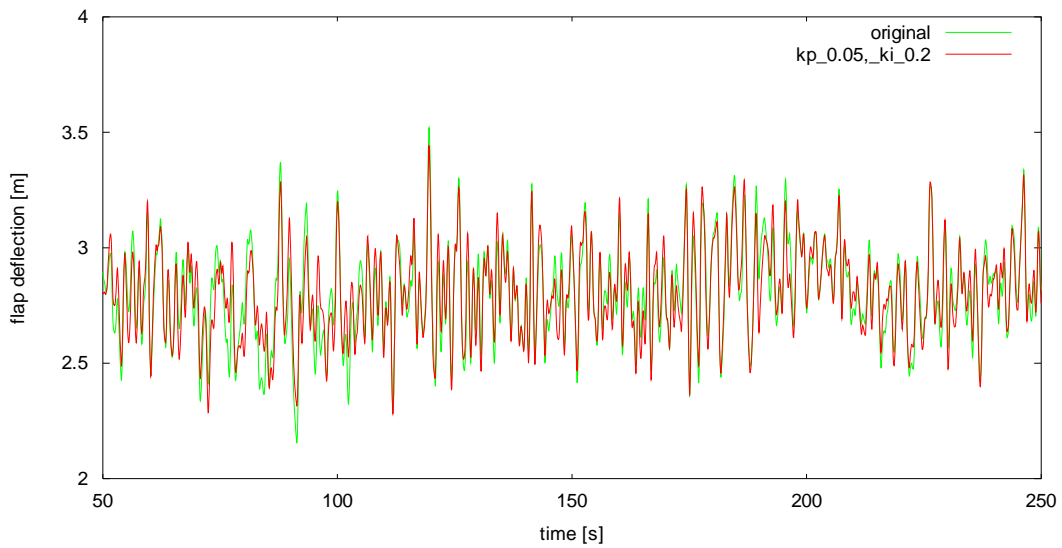


Figure 14: Time series of flap deflection for $k_p=0.05 \text{ deg s}^2/\text{m}$, $k_i=0.20 \text{ deg s/m}$.

The above gains provide maximum equivalent load reduction of **11%**. The flap demand angle is shown in Figure 15. It is compared against the unfiltered case. With the present choice of gains the range of variation of the demand angle is higher (similar to the unfiltered case) however, the high frequency ripple is again removed. The maximum speed of the flap angle variation does not exceed **3 deg/s** in this case.

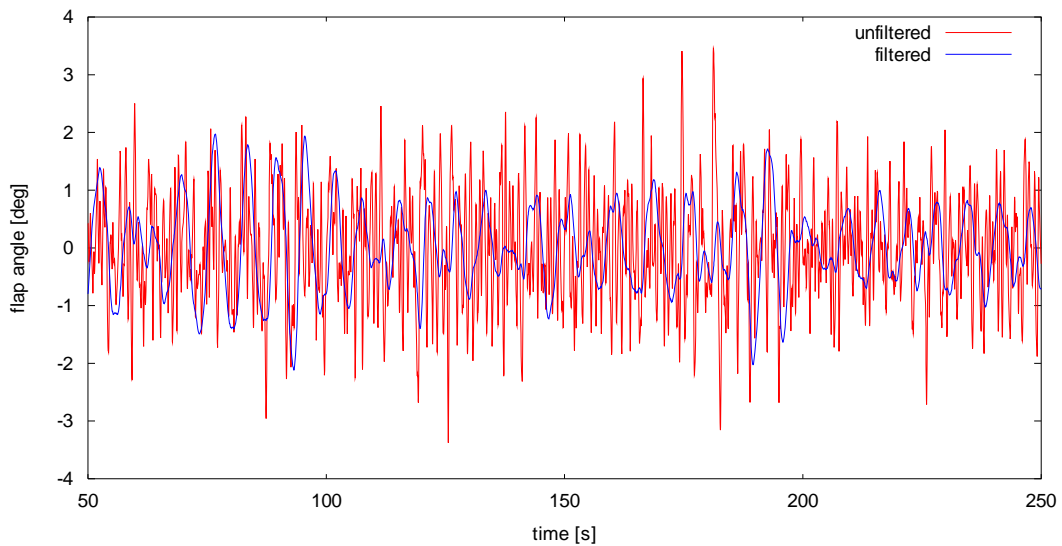


Figure 15: Time series of flap demand angle for $k_p=0.05 \text{ deg s}^2/\text{m}$, $k_i=0.20 \text{ deg s/m}$

In Figure 16 the rainflow counting plots comparing the controlled against the uncontrolled case are shown. It is seen that the controller reduces the range of the low frequency cycles as expected. On the contrary, the range of the high frequency cycles increases. Overall, in terms of the equivalent fatigue load, a reduction is obtained.

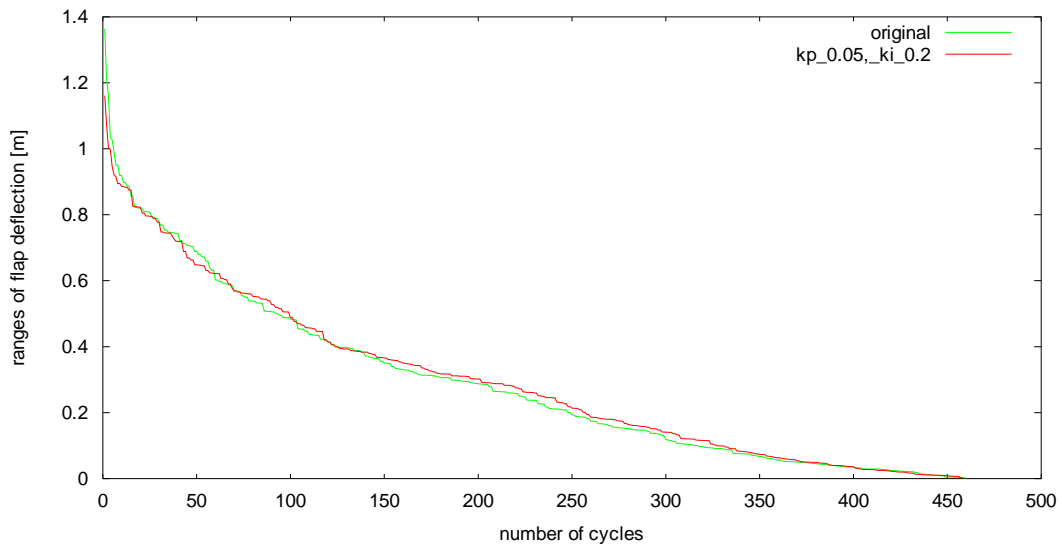


Figure 16: Rainflow counting plot for $k_p=0.05 \text{ deg s}^2/\text{m}$, $k_i=0.20 \text{ deg s}/\text{m}$ (comparison against baseline case).

Lowpass filter 0.3 Hz

In this section results of the PI controller that takes as input a lowpassed filtered signal of the acceleration (edge frequency 0.3 Hz, passband ripple $R_p=3 \text{ dB}$ and stopband attenuation $R_s=50 \text{ dB}$) are shown. This is an intermediate step between the unfiltered and the bandpassed filtered case. In Figure 17 the time series of the flap deflection is presented for an integral gain $k_i=0.10 \text{ deg s}/\text{m}$. Again, the results of the TE flap control simulation are compared against the baseline results of the uncontrolled case.

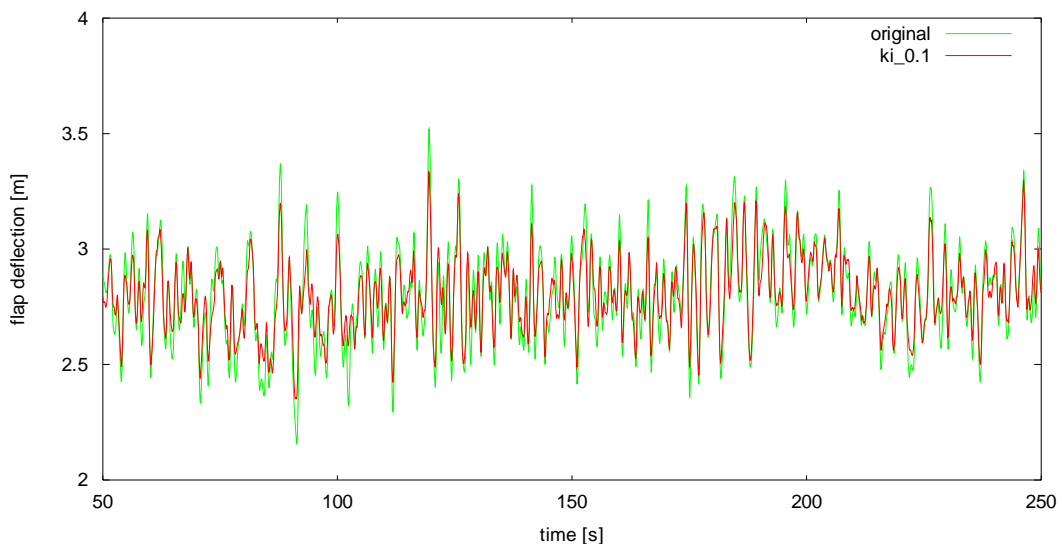


Figure 17: Time series of flap deflection for $k_i=0.10 \text{ deg s}/\text{m}$.

The percentage of the equivalent load reduction is **26%**, similar to the unfiltered case. Although a quite high load reduction is achieved the high frequency fluctuations in the

flap demand signal are much lower than in the unfiltered signal (see Figure 18). The flap speed in this case is going up to **10 deg/s**.

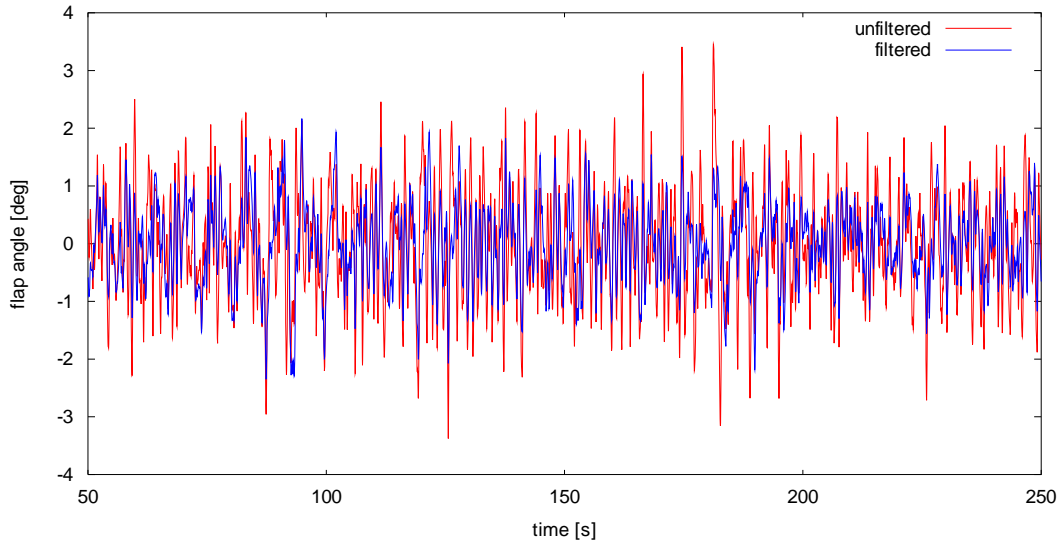


Figure 18: Time series of flap demand angle for $k_i=0.10$ deg s/m

Comparison between different filters

In the present section a comparison of the load reduction capabilities of the various filters examined is presented. The comparison is made on the basis of the rainflow counting plots of the loads time series. The integral gain in all presented cases is $k_i=0.1$ deg s/m (except for the unfiltered case and the case of infinite bandwidth where $k_i=0.05$ deg s/m).

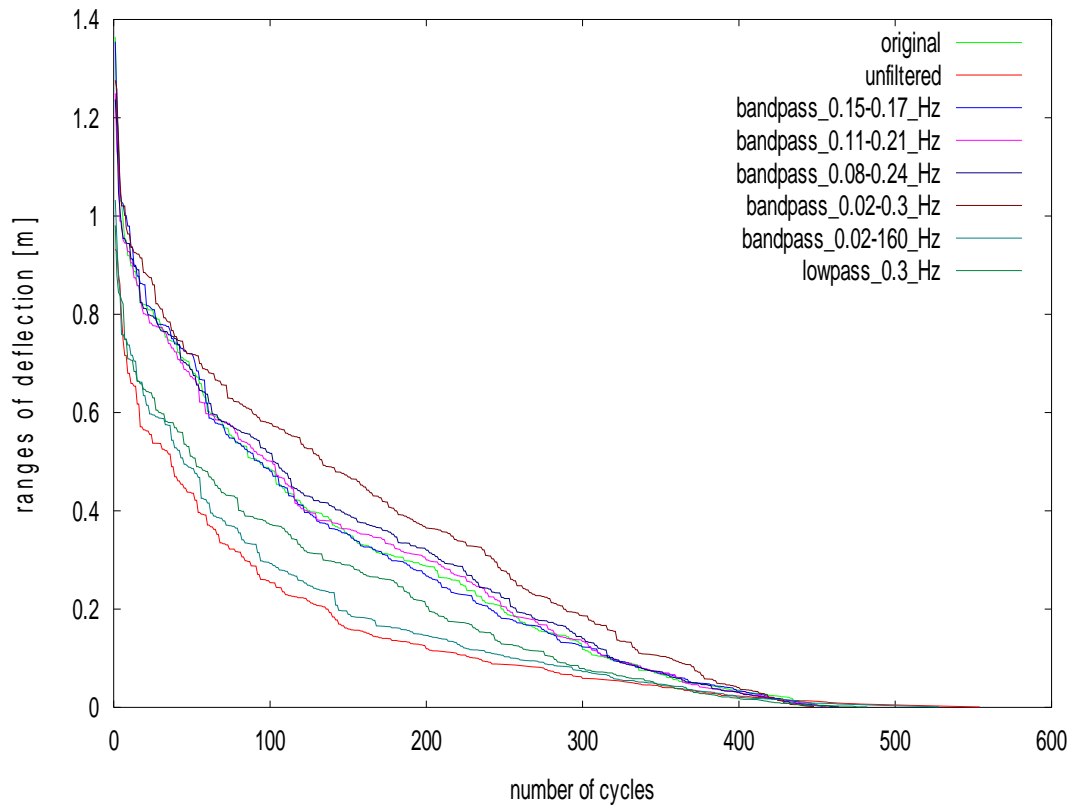


Figure 19: Rainflow counting plots comparison.

In Figure 19 it can be seen that when the range of the bandpass filter is either too low (e.g. [0.15-0.17 Hz]) or too high (e.g. [0.08-0.24 Hz]) the load reduction capabilities are moderated. In some cases a load increase is even obtained [0.02-0.3 Hz]. Better results are obtained for intermediate ranges. For an infinite bandwidth [0.02 160 Hz] the obtained results are quite similar to the unfiltered case.

Shape Memory Alloys

Shape Memory Alloys are “active” or “multifunctional” materials whose structure and composition can be controlled in order to affect their properties and achieve a specific functionality. SMAs have the unique capability to restore their original shape after being deformed excessively to an inelastic strain that could be up to 8%. The key mechanism behind this unique feature lies in the ability of the material to subject to a diffusionless transformation between two different stable phases: the high temperature parent phase (Austenite – A), which is micro structurally symmetric and the lower temperature less symmetric phase (Martensite – M) [3]. The material can revert back to the parent phase either by heating or by simply removing the load that caused the phase transformation if certain thermomechanical conditions apply. These materials exhibit direct coupling (the mechanical or non-mechanical field can serve as an input while the other as the output) are ideal for use in actuation applications because they undergo transformations with high energy density (available work per unit volume).

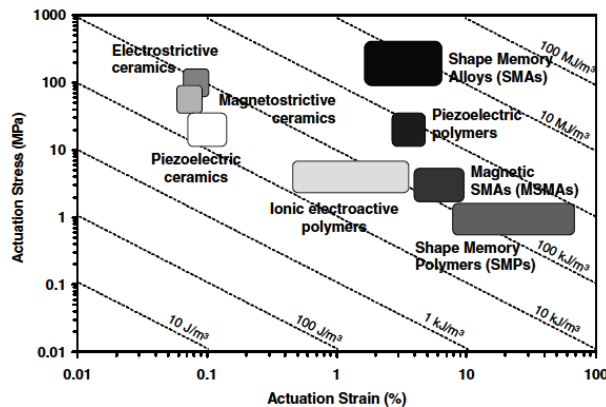


Figure 20: Actuation Energy Density for various Active Materials at typical ranges of Actuation Stress and Actuation Strain

As mentioned before SMAs have two different phases, each one with a specific crystal structure and therefore different properties. The high temperature phase is called Austenite (A), while the low temperature phase is called Martensite (M). Transformation from one phase to the other occurs by shear lattice distortion. Martensite exists in two different forms, twinned (M^t) and detwinned (M^d) martensite. Actuation capabilities of SMAs derive from the Shape Memory Effect (SME). SME is exhibited when a SMA while in phase of austenite is cooled below a critical temperature (M_f) to form twinned martensite, mechanically loaded till martensite is detwinned, unloaded and subsequently heated above a temperature threshold (A_f). Direct transformation of austenite to detwinned martensite though mechanical loading is accompanied by large inelastic macroscopic strain ($>4\%$) that is not recovered upon unloading. This procedure is referred as forward or martensitic transformation. The transformation of martensite (either twinned or detwinned) back to austenite during SME, can only occur through heating above a critical temperature (A_f). If martensite is in twinned form the transformation is called reverse transformation and there is no associated shape change, but if martensite is detwinned the inelastic strain, called transformation strain (ϵ^t), is recovered and the material gains its initial configuration. Figure 21 presents schematically the SME in stress – strain – temperature space where ξ indicated the martensitic volume fraction. Starting from austenitic phase (point A), temperature is lowered. Cooling results in the transformation to twinned martensite (point B) without generation of any macroscopic strain and subsequently shape change. By applying mechanical load to the material it transforms to

detwinned martensite (point C) with a simultaneous strain generation. During unloading of the material the elastic strain is recovered with no transformation process taking place (point D). Heating the material above a certain temperature threshold it transforms back to austenite with associated shape change to parent configuration.

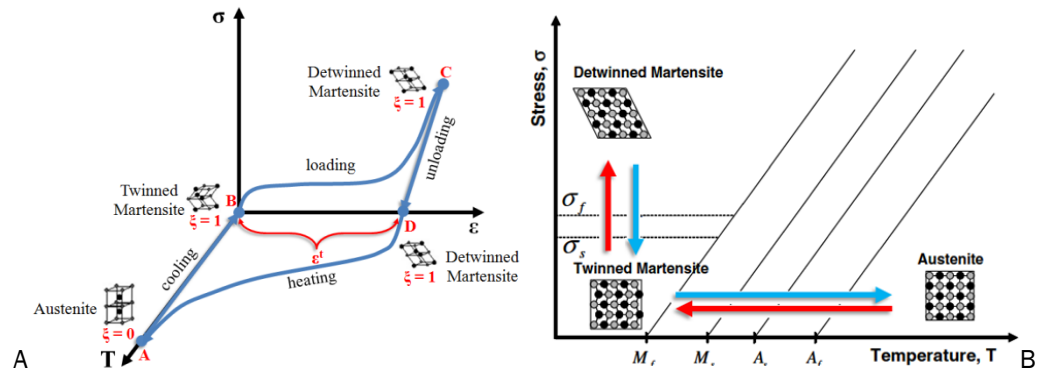


Figure 21: Shape Memory Effect
A. Thermomechanical Loading Cycle B. Phase Diagram

Pseudoelasticity is the second special behavior related to Shape Memory Alloys, which effectively contributes to its functionality as an actuator under high temperature conditions. It is associated with recovery of the transformation strain while temperature is above a specific critical value [4]. Starting from austenitic phase, the material is stressed and transformed to detwinned martensite developing the transformation strain. Upon unloading the transformation strain is recovered and the material transforms back to austenite gaining its initial shape. The forward and reverse transformation during a complete pseudoelastic cycle results in hysteresis, which in the stress – strain space, represents energy dissipated in the transformation cycle. A schematic representation of a pseudoelastic cycle is presented in Figure 22 A in stress – temperature space and in Figure 22 B in stress – strain space where it is clear that pseudoelastic or superelastic behaviour of SMAs could be divided into three regions: linear austenitic region, phase transformation region and linear martensitic region. It should be noted that Figure 22 A is also called phase diagram, because blue and red lines indicate the limits between transformation regions and temperatures M^0s , M^0f , A^0s , A^0f are temperature start and finish transformation thresholds at zero stress level. Respectively, in Figure 22 B stress start and finish transformation thresholds are indicated as σ^{Ms} , σ^{Mf} , σ^{As} , σ^{Af} .

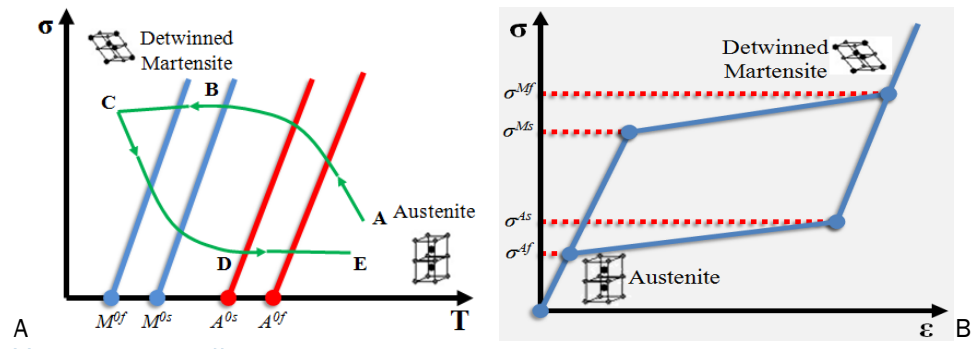


Figure 22: Pseudoelastic Effect
A. Phase Diagram B. Stress Strain Diagram

Shape memory alloys can be used as actuators in wire form to change airfoil shape after being placed in suitable locations on a support structure. Considering a pre-strained SMA wire in detwinned martensite phase clamped in point A and pinned in point B, when

heated above A_s , reverse transformation occurs and stresses are being developed. The resulting force can be used for actuation of the morphing structure in this study.



Figure 23

Specialty Finite Element for SMA Wire Actuators

For the scope of this project a numerical tool enabling prediction of the complex SMA response under various thermal or mechanical loads has been developed. In this section the derivation and implementation of a beam finite element, capable to predict the fully coupled thermomechanical behavior of SMA actuators in 1D form is described. The beam element is able to predict also the time response of the SMA. The development of the new finite element was implemented in the framework of FEA software ABAQUS available subroutines which provide the user with the ability to implement a custom element. Specifically, the aforementioned beam element is implemented in the User Element (UEL) subroutine, an overview of which is given in Figure 24. In the remaining section the governing equations and the appropriate SMA constitutive equations are described.

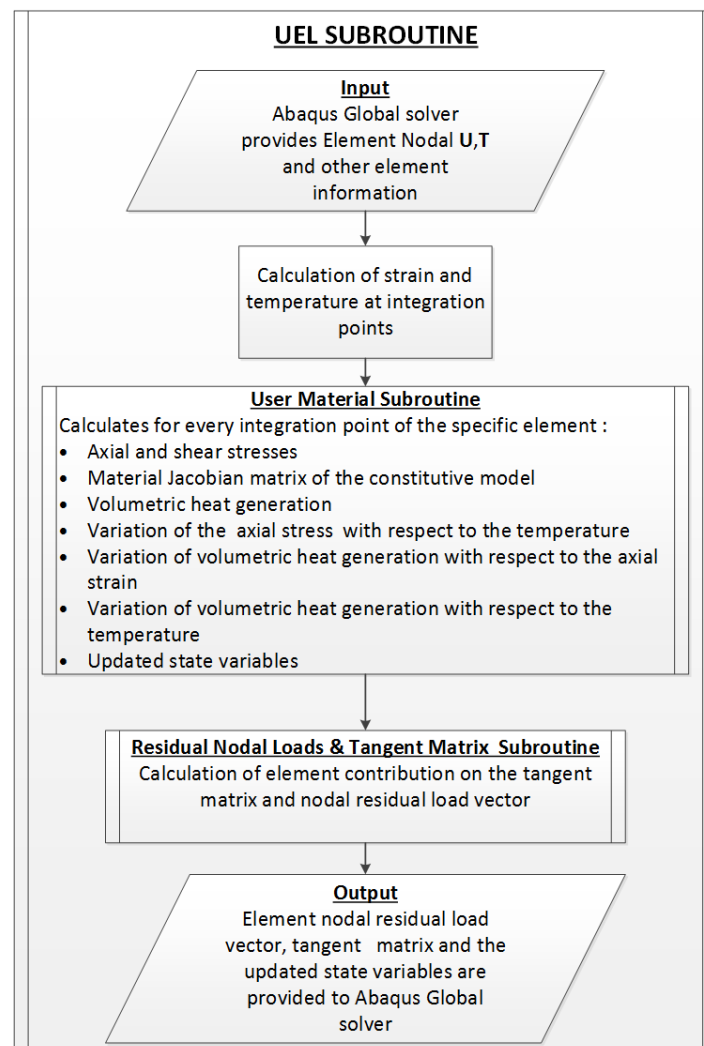


Figure 24: Overview of the developed beam finite element

The mechanical equilibrium equations of 2D SMA beam in the x-z plane are:

$$\frac{d\sigma_x}{dx} + \frac{d\sigma_{xz}}{dz} + f_x = 0 \quad (0)$$

$$\frac{d\sigma_{xz}}{dx} + \frac{d\sigma_z}{dz} + f_z = 0 \quad (0)$$

Where σ_x and σ_{xz} are the axial and shear stresses respectively, while f_x and f_z are the field forces in the x and z directions. The energy conservation equation derived by Lagoudas et al. [5] is

$$\nabla \cdot \mathbf{q} + \rho c \dot{T} - q_s - q_L - q_t = 0 \quad (0)$$

Where $\mathbf{q} = \{q_x, q_z\}$ is the heat flux vector, ρ is the density of the material, c is the specific heat and \dot{T} is the time derivative of the material temperature; q_s represents the distributed heat sources, q_L the latent heat per unit volume due to phase transformations, and q_t the energy release or absorption per unit volume due to the thermoelastic effect. q_L and q_t terms are related to stress σ_x , and as a consequence, the mechanical response of the SMA material is coupled with the thermal response. The constitutive relations for heat flux are defined as:

$$\mathbf{q} = \begin{Bmatrix} q_x \\ q_z \end{Bmatrix} = - \begin{bmatrix} k_x & 0 \\ 0 & k_z \end{bmatrix} \begin{Bmatrix} \frac{dT}{dx} \\ \frac{dT}{dz} \end{Bmatrix} \quad (0)$$

Where k_x and k_z are the conduction coefficients in x and z direction respectively.

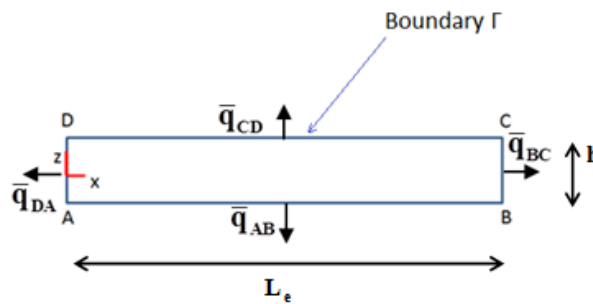


Figure 25: Geometrical Representation of heat flux on Beam Surface

SMA constitutive model

The constitutive model of Lagoudas et al. in a properly reduced 2D form was selected to describe the SMA behavior. This model uses Gibbs free energy as thermodynamic potential in order to describe the thermodynamic state of the material by using temperature, stress and total martensitic volume fraction (MVF). MVF, ξ accounts for the generation and recovery of all martensitic variants and is bounded by $0 \leq \xi \leq 1$.

Hooke's law is defined as:

$$\sigma_x = E_x (\varepsilon_x - \alpha_x (T - T_0) - \varepsilon^t) \quad (0)$$

$$\sigma_{xz} = G \varepsilon_{xz} \quad (0)$$

Where, $\varepsilon_x, \varepsilon_{xz}$ are the total axial and shear strains respectively; E and G are the effective elastic modulus and shear modulus respectively; α_x is the effective thermal expansion coefficient in x direction, T is the material's temperature, T_0 is the strain-free reference temperature; ε^t is the recoverable axial inelastic strain generated during transformation from austenite to martensite and subsequently recovered during full reverse transformation. The effective material properties are calculated by the properties of each net phase and the MVF ξ , using the rule of mixtures.

$$\frac{1}{E_x} = \frac{1}{E_x^A} + \xi \left(\frac{1}{E_x^M} - \frac{1}{E_x^A} \right) \quad (0)$$

$$\alpha_x = \alpha_x^A + \xi (\alpha_x^M - \alpha_x^A) = \alpha_x^A + \xi \Delta \alpha_x \quad (0)$$

$$c = c^A + \xi (c^M - c^A) = c^A + \xi \Delta c \quad (0)$$

$$s_0 = s_0^A + \xi (s_0^M - s_0^A) = s_0^A + \xi \Delta s_0 \quad (0)$$

$$v_0 = v_0^A + \xi (v_0^M - v_0^A) = v_0^A + \xi \Delta v_0 \quad (0)$$

where, s_0, v_0 are the specific entropy and specific internal energy at the reference state, and superscripts A and M denote the austenitic and martensitic phases respectively. The boundaries for the initiation and completion of the transformation processes for all possible thermodynamic paths are derived from the second law of thermodynamics (Clausius-Planck inequality):

$$\left(\sigma_x \Lambda + \frac{1}{2} \sigma_x \left(\frac{1}{E_x^M} - \frac{1}{E_x^A} \right) \sigma_x + \sigma_x \Delta \alpha_x (T - T_0) - \rho \Delta c \left[(T - T_0) - T \ln \left(\frac{T}{T_0} \right) \right] + \rho \Delta s_0 T - \rho \Delta u_0 - f^t \right) \dot{\xi} = \Pi \dot{\xi} \geq 0 \quad (0)$$

The expression inside the parentheses on the left of the inequality is defined as:

$$\begin{aligned} \Pi(\sigma_x, T, \xi) = & \sigma_x \Lambda + \frac{1}{2} \sigma_x \left(\frac{1}{E_x^M} - \frac{1}{E_x^A} \right) \sigma_x + \sigma_x \Delta \alpha_x (T - T_0) - \\ & \rho \Delta c \left[(T - T_0) - T \ln \left(\frac{T}{T_0} \right) \right] + \rho \Delta s_0 T - \rho \Delta u_0 - f^t \end{aligned} \quad (0)$$

and is termed as the thermodynamic force conjugated to the MVF ξ . The term Λ determines the transformation strain direction and magnitude and is assumed to have the following form:

$$\Lambda = \begin{cases} \Lambda_{fwd} = H^{cur} (|\sigma_x|) \text{sgn}(\sigma_x) ; & \dot{\xi} > 0 \\ \Lambda_{rev} = \frac{\varepsilon^{t-r}}{\xi^r} ; & \dot{\xi} < 0 \end{cases} \quad (0)$$

where, ε^{t-r} is the transformation strain at transformation reversal, ξ^r is the MVF at the same point, and subscripts “fwd” and “rev” indicate forward and reverse transformation. The term H^{cur} describes the maximum axial transformation strain generated during full transformation from austenite to martensite at a given applied stress level and is defined as:

$$H^{cur}(|\sigma_x|) = \begin{cases} H_{\min}; & |\sigma_x| > \sigma_{crit} \quad (0) \\ H_{\max} + (H_{\max} - H_{\min})(1 - e^{-k_t(|\sigma_x| - \sigma_{crit})}); & |\sigma_x| > \sigma_{crit} \quad (0) \end{cases}$$

where, H_{\min}, H_{\max} are the minimum and maximum transformation strain; σ_{crit} denotes the equivalent stress threshold value below which the material exhibits $H^{cur}(|\sigma_x|) = H_{\min}$; and the parameter k_t controls the rate at which $H^{cur}(|\sigma_x|)$ evolves exponentially from H_{\min} to H_{\max} .

Finally, the term f^t is defined for the forward and reverse transformation as:

$$f^t = \begin{cases} f_{fwd}^t = \frac{1}{2}a_1(1 + \xi^{n_1} - (1 - \xi)^{n_2}) + a_3; & \dot{\xi} > 0 \quad (0) \\ f_{rev}^t = \frac{1}{2}a_2(1 + \xi^{n_3} - (1 - \xi)^{n_4}) - a_3; & \dot{\xi} < 0 \quad (0) \end{cases}$$

The form of f^t is chosen by the implemented model in order to capture the smooth hardening of SMA in a thermodynamically consistent manner. The parameters $H_{\max}, H_{\min}, \alpha_1, \alpha_2, \alpha_3, n_1, n_2, n_3, n_4$ in Equations (0) to (0) are calibrated experimentally. For every reversible process, the Clausius-Plank inequality (0) must remain equal to zero, while for every irreversible process it must have a positive value. Hence, for the forward transformation ($\dot{\xi} > 0$), Π takes positive values, $\Pi(\sigma_x, T, \xi) = Y^t(\sigma_x) > 0$. Similarly, in the reverse transformation ($\dot{\xi} < 0$) Π should take negative values $\Pi(\sigma_x, T, \xi) = -Y^t(\sigma_x)$. Finally when no phase transformation takes place ($\dot{\xi} = 0$) the inequality holds true independently of the values of Π as $\Pi\dot{\xi} = 0$. In the preceding conditions $Y^t(\sigma_x)$ is a positive threshold value that determines the initiation of the forward/reverse transformation and is defined as:

$$Y^t = Y_0^t + D\sigma\Lambda \quad (0)$$

Where Y_0^t is the threshold value when the material is in a stress free state, and D is a constant which is determined during model calibration process.

The internal heat sources of the material, here after termed as thermomechanical coupling terms, can be attributed to distributed phase transformation process and to the thermoelastic effect and can be calculated by:

$$q_L(\sigma_x, T, \xi) = (\Pi - \frac{\partial \Pi}{\partial T} T)\dot{\xi} \quad (0)$$

$$q_t(\sigma_x, T, \xi) = -\alpha_x : \dot{\sigma}_x T \quad (0)$$

As q_L and q_t are implicit functions of axial stress they essentially couples the thermoelastic force equilibrium equations (0) and (0) with the energy conservation equation (0) of the thermal problem.

Finally the distributed internal Joule heating sources q_s in equation (0) can be expressed in relation to the current as follows:

$$q_s = \frac{I^2 r_r}{A^2} \quad (0)$$

Where I is the electric current passing through the cross section, r_r is the specific electrical resistance of the SMA and A is the cross section of the beam.

Beam Element

In the following paragraphs the formulation of a two-node thermomechanical beam element is described.

Assumed displacement and temperature fields

For the displacement and temperature fields through the thickness (h) of the cross section kinematic assumptions have been made. First-order shear deformation theory (FSDT) was implemented in the beam section for calculating the displacement field. According to this theory the beam element can undergo extension along x-axis, bending in z direction and constant shear in the x-z plane (Figure 26(A)). The temperature field is approximated by a high-order cubic polynomial along the height of the cross section.

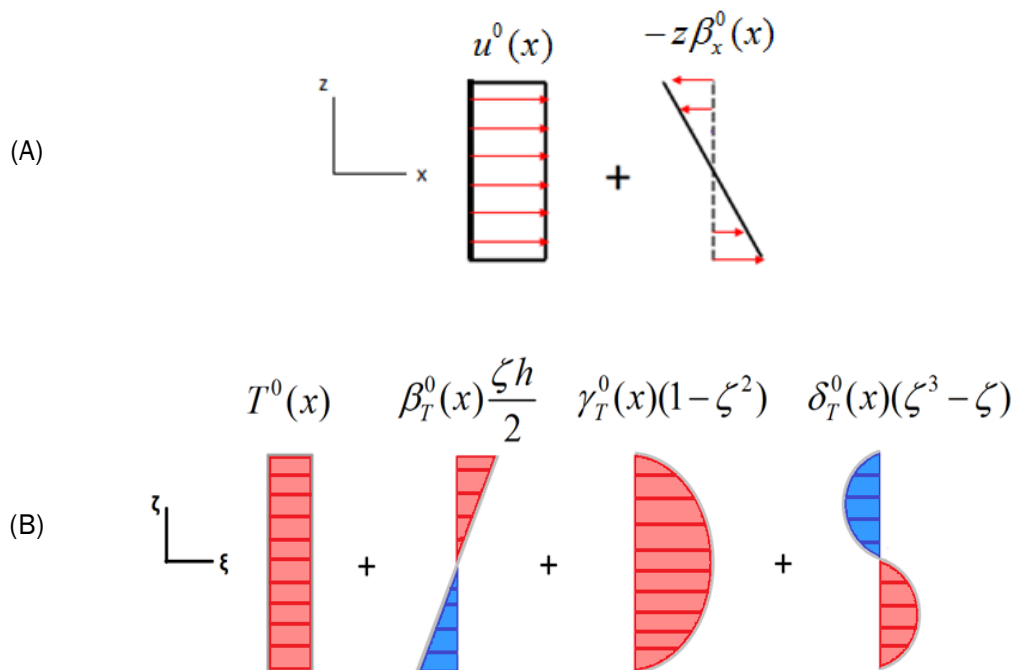


Figure 26: Assumed Fields through Thickness of a Beam Section (A) Displacement Field and (B) Temperature Field

The following equations calculate the displacement and the temperature field on the beam cross-section:

$$u(x, z) = u^0(x) - \beta_x^0(x) \frac{\zeta h}{2} \quad (0)$$

$$w(x, z) = w^0(x) \quad (0)$$

$$T(x, \zeta) = T^0(x) + \beta_T^0(x) \frac{\zeta h}{2} + \gamma_T^0(x)(1 - \zeta^2) + \delta_T^0(x)(\zeta^3 - \zeta) \quad (0)$$

where, $u(x, z)$ is the total axial displacement, $u^0(x)$ is the uniform axial displacement, $\beta_x^0(x)$ is the angle of rotation of the beam cross section and $w^0(x)$ is the transverse displacement of the center line of the beam cross section. The four components shown in Equation (0), describe the uniform, linear, parabolic and cubic distribution of the temperature through the thickness of the beam. By proper specification of the corresponding coefficients $T^0, \beta_T^0, \gamma_T^0, \delta_T^0$, we can approximate the full temperature field on the cross section as shown in Figure 25 **Error! Reference source not found.**(b). In the previous equations, h is the height of the beam's cross section, $\zeta = \frac{2z}{h}$ is the non-dimensional thickness variable which takes values from -1 to 1, and superscript 0 refers to the value of each variable at the mid-plane of the section. Taking into account the displacement Equations (0) and (0), the axial strain ε_x and the shear strain ε_{xz} are given by the following expressions,

$$\varepsilon_x = \frac{\partial u(x, z)}{\partial x} = \frac{du^0(x)}{dx} - \frac{d\beta_x^0(x)}{dx} \frac{\zeta h}{2} = \varepsilon_x^0(x) - \frac{d\beta_x^0(x)}{dx} \frac{\zeta h}{2} \quad (0)$$

$$\varepsilon_{xz} = \frac{dw^0(x)}{dx} - \beta_x^0(x) \quad (0)$$

In the same manner using Equation (0), the temperature gradients in x and z directions are given by the following two expressions respectively.

$$\frac{dT(x, \zeta)}{dx} = \frac{dT^0(x)}{dx} + \frac{d\beta_T^0(x)}{dx} \frac{\zeta h}{2} + \frac{d\gamma_T^0(x)}{dx} (1 - \zeta^2) + \frac{d\delta_T^0(x)}{dx} (\zeta^3 - \zeta) \quad (0)$$

$$\frac{dT(x, \zeta)}{dz} = \frac{dT(x, \zeta)}{d\zeta} \frac{d\zeta}{dz} = \left[\beta_T^0(x) \frac{h}{2} - 2\gamma_T^0(x)\zeta + \delta_T^0(x)(3\zeta^2 - 1) \right] \frac{2}{h} \quad (0)$$

FE formulation

For implementing the equilibrium equations in finite elements the equivalent variational form is derived by multiplying equations (0) and (0) by an arbitrary variation of displacement $\delta \mathbf{u}$ we assume the form of the virtual work equilibrium:

$$\delta \mathbf{U}^T \Psi_U = b \int_A \delta \varepsilon_x \sigma_x dA + b \int_A \delta \varepsilon_{xz} \sigma_{xz} dA - b \int_A \delta \mathbf{u}^T \mathbf{f}_f dA - b \int_\Gamma \delta \mathbf{u}^T \boldsymbol{\tau} d\Gamma = 0 \quad (0)$$

Where Ψ_u is the discretized balance vector between internal and external forces and $\delta \mathbf{U}$ is the arbitrary variation of discretized displacements; the first and second term from the left in the middle part of the equation represent the variation of axial and shear strain energy, the third and last term the work of field forces and traction forces, respectively; b is the width of the beam, $\delta \mathbf{u}$ is the variation of displacements, \mathbf{f}_f is the field forces vector and $\boldsymbol{\tau}$ is the surface traction vector.

The variational form of thermal equilibrium is similarly derived by multiplying Equation (0) by δT and expresses the equilibrium between internal and external thermal loads variation acting on the thermal solid.

$$\begin{aligned} \delta \mathbf{T} \Psi_T = & -b \int_A \mathbf{q} \cdot (\nabla \delta T) dA + b \int_A \delta T (\rho c \dot{T}) dA - \\ & b \int_A \delta T (q_s + q_L + q_t) dA + b \int_\Gamma \delta T \bar{\mathbf{q}}_\Gamma \cdot \mathbf{n} d\Gamma = 0 \end{aligned} \quad (0)$$

In the preceding equation, Ψ_T is the discretized balance between internal and external thermal loads, $\delta \mathbf{T}$ is the arbitrary variation of discretized thermal DOFs and δT is the arbitrary variation of the temperature. The first integral from the left represents the internal energy flux due to heat transfer. The second integral represents the thermal energy of the solid due to its specific heat capacity. The third integral entails three components: the first represents the thermal energy due to distributed internal sources q_s per unit volume; the second component represents the energy release or absorption per unit volume q_L due to exothermic and endothermic reactions during phase transformation provided by Equation(0); and the third component q_t expresses the thermoelastic energy release or absorption per unit volume. Finally, the last integral represents the heat energy variation due to surface thermal loads, which in the case of heat convection take the form:

$$\bar{\mathbf{q}}_\Gamma = h_\Gamma (T - T_{env}) \hat{\mathbf{n}} \quad (0)$$

Where $\hat{\mathbf{n}}$ is the outward pointing normal surface unit vector on the boundary Γ consisting of segments AB,BC,CD,DA , $h_\Gamma = \langle h_{AB}, h_{BC}, h_{CD}, h_{DA} \rangle$ is the heat transfer coefficients on the boundary Γ (Figure 24) and T_{env} is the far-field temperature of the adjacent fluid.

As previously explained, the consideration of terms q_L and q_t effectively couples the equilibrium Equations (0) and (0), therefore, they should be considered and solved simultaneously. Conversely, by neglecting the q_L , q_t terms the Equations (0) and (0)

decouple and thermal effects such as heat losses due to convection or thermal conductivity would be approximately captured.

A new beam element is formulated entailing seven degrees of freedom at each node, which approximate the generalized section variables through shape functions $N^i(x)$,

$$[u^0(x), w^0(x), \beta_x^0(x), T^0(x), \beta_T^0(x), \gamma_T^0(x), \delta_T^0(x)] = \sum_{i=1}^{nodes} N^i(x) [u^{0i}, w^{0i}, \beta_x^{0i}, T^{0i}, \beta_T^{0i}, \gamma_T^{0i}, \delta_T^{0i}] \quad (0)$$

where the nodal variables with superscript $0i$ refer to the value of each node “ i ” calculated at the mid-plane “ 0 ”. The same c^0 shape functions $N^i(x)$ are used for each degree of freedom.

Equations (0) and (0) combined with equation (0) are then expressed in the discretized form of residual load vectors Ψ_u, Ψ_T for calculation of the non linear time behavior of SMA material.

$$\Psi_U = \sum^{nelm} \Psi_U^{elm} = 0 \quad (0)$$

$$\Psi_T = \sum^{nelm} (\Psi_T^{elm}) = 0 \quad (0)$$

The time response of the SMA structure is driven by the thermal equilibrium equation (0). The backward difference time integration method combined with the Newton-Raphson iterative non linear procedure is used to solve the coupled system of the non linear equations (0) and (0). The time domain is discretized to a finite number of time steps with resolution Δt , each beginning at time t and ending at time $t+\Delta t$. The Equations (0) and (0) are solved at time $t+\Delta t$ using the N-R process. The time derivatives of each term are approximated by the backward finite difference formula, to yield the residual load

vector ${}^{t+\Delta t}\Psi_U$ and ${}^{t+\Delta t}\Psi_T$.

$${}^{t+\Delta t}\dot{F} = \frac{{}^{t+\Delta t}F - {}^tF}{\Delta t} \quad (0)$$

where, F is the variable to be differentiated and left superscripts indicate the respective time step. At each time step, the corresponding load increment is applied and an improvement of the solution is calculated according to the N-R iterative process, by solving the following equations:

$$- \begin{bmatrix} \bar{\bar{\mathbf{K}}}_U & \bar{\bar{\mathbf{K}}}_{UT} \\ \bar{\bar{\mathbf{K}}}_{TU} & \bar{\bar{\mathbf{K}}}_T \end{bmatrix}^{t+\Delta t} \begin{Bmatrix} \Delta \mathbf{U} \\ \Delta \mathbf{T} \end{Bmatrix} = \begin{Bmatrix} \Psi_U \\ \Psi_T \end{Bmatrix} \quad (0)$$

where: $\bar{\bar{\mathbf{K}}}$ is the total tangent matrix which is also evaluated at the end of the time step and contains the mechanical, thermal and coupling components, indicated by subscripts U, T and UT respectively; $\Delta \mathbf{U}$ and $\Delta \mathbf{T}$ are increments of the nodal displacement and temperature. A series of iterations are performed in each time step, till the residual mechanical and thermal load vectors ${}^{t+\Delta t} \Psi_U$, ${}^{t+\Delta t} \Psi_T$ are driven to zero, hence equilibrium Equations (0) and (0) are satisfied.

The total tangent matrix $\bar{\bar{\mathbf{K}}}$ and the element tangent matrix $\bar{\bar{\mathbf{K}}}^{elm}$ are defined as:

$$\bar{\bar{\mathbf{K}}} = \begin{bmatrix} \bar{\bar{\mathbf{K}}}_U & \bar{\bar{\mathbf{K}}}_{UT} \\ \bar{\bar{\mathbf{K}}}_{TU} & \bar{\bar{\mathbf{K}}}_T \end{bmatrix} = \begin{bmatrix} \frac{\partial \Psi_U}{\partial \mathbf{U}} & \frac{\partial \Psi_U}{\partial \mathbf{T}} \\ \frac{\partial \Psi_T}{\partial \mathbf{U}} & \frac{\partial \Psi_T}{\partial \mathbf{T}} \end{bmatrix} = \sum^{nelm} \bar{\bar{\mathbf{K}}}^{elm} = \sum^{nelm} \begin{bmatrix} \frac{\partial \Psi_U^{elem}}{\partial \mathbf{U}} & \frac{\partial \Psi_U^{elem}}{\partial \mathbf{T}} \\ \frac{\partial \Psi_T^{elem}}{\partial \mathbf{U}} & \frac{\partial \Psi_T^{elem}}{\partial \mathbf{T}} \end{bmatrix} \quad (0)$$

where time step superscripts are omitted for brevity.

A user element (UEL) subroutine was developed for interpreting the previous described equations in ABAQUS FEA software according to the Reference Manual (ABAQUS 2011) (ABAQUS_6, 2012).

The RHS (Equation(0)) represents the contribution of the element to the residual load vector,

$$RHS = \Psi^{elm} = \begin{Bmatrix} \Psi_U^{elm} \\ \Psi_T^{elm} \end{Bmatrix} \quad (0)$$

while the AMATRX (Equation(0)) represents the negative tangent matrix (in the specific occasion it contains element's tangential mechanical, thermal and coupling matrices).

$$AMATRX = -\bar{\bar{\mathbf{K}}}^{elm} = -\frac{\partial \Psi^{elm}}{\partial (\mathbf{U}, \mathbf{T})} = -\frac{\partial RHS}{\partial (\mathbf{U}, \mathbf{T})} \quad (0)$$

Both arrays are defined in UEL and ABAQUS global solver assembles the total load vector matrix and tangent matrix.

In brief, ABAQUS global solver provides the new guess of the element nodal variables and the solution-dependent state variables available from the previous time step, as inputs to the UEL which is called for every iteration of every time step of N-R processes for each element. The nodal variables are the displacements and the temperatures, while the solution-dependent state variables are the transformation strain and the martensitic volume fraction. After the nodal and solution-dependent state variables are passed in the UEL subroutine the strains and the temperatures are calculated at the integration points of the element and passed into a user material subroutine which implements the SMA constitutive model in discretized form. Details about the implementation of the numerical

form of the constitutive model can be found in the work of [5] [7]. With the aforementioned inputs available, the calculation of stresses, σ_x, σ_{xz} and the Material Jacobian matrix of the constitutive model, $\frac{\partial \sigma}{\partial \epsilon}$ are performed. Also the volumetric heat generation, $Q = q_L + q_t$, the variation of axial stress with respect to temperature $\frac{\partial \sigma_x}{\partial T}$, the variation of volumetric heat generation with respect to axial strain $\frac{\partial Q}{\partial \epsilon_x}$ and the variation of volumetric heat generation with respect to temperature, $\frac{\partial Q}{\partial T}$ are calculated.

Finally the updated values of the solution-dependent state variables are determined. The solution state variables are always calculated in the user material subroutine therefore are always linked to element's integration points.

All the previous quantities, calculated at the integration points, are required to perform the necessary numerical integrations involved in the calculation of the residual load vector and tangential matrix terms. Finally, the UEL outputs to ABAQUS global solver the element nodal residual loads, the element tangent matrix and the updated state variables.

Implementation of Time Domain Control Equations

The time response of the whole adaptive structure is mandated by the dominant SMA time response. The time response of the SMA is included in the thermal equilibrium equation (Equation (0) in discretized form) described in the previous section. More specifically, the SMA time response is dictated primarily by the term that expresses the specific heat capacity in Equation (0) ($\rho c \dot{T}$) and is depended on the rate of temperature change. Secondly the coupling terms (i) q_L (Equation (0)) that expresses energy dissipation or absorption during phase transformations and is depended on the rate of MVF change and (ii) q_t (Equation (0)) that expresses the energy release or absorption due to the thermoelastic effect and is depended on the rate of the developed stress change, affect also the time response of the SMA.

It can be assumed that the amount of energy provided to the SMA in order to change its temperature plays a significant role to the response of the morphing WTB trailing edge, as the temperature of the actuators drives the exerted actuation forces. The provided energy is the quantity that should be controlled in order to achieve the desired time and structural response.

Controller Implementation

The approach decided to be followed for controlling the position of the morphing trailing edge adopted the implementation of a Proportional –Integral –Derivative (PID) controller. The PID controller is a widely used mechanism in industrial control systems which function is based on the effort to minimize the error between the desired set point and the measured (process) variable. The error of these two values is estimated by a feedback loop which compares the process value with the set point value. Towards the minimization of the error, the PID controller algorithm entails three constant value parameters thus called also three term control. These parameters are widely called as the proportional gain (K_P) which depends on the present error, integral gain (K_I) which

depends on the accumulation of past errors and derivative gain (K_D) which expresses a prediction of future errors based on the current rate of change. The weighted sum of these gains is used to adjust the process via a control element.

As the morphing trailing edge has a highly non linear response, the approach of designing a controller by using the transfer function of the system proved to be infeasible as it applies only on linear systems. Though a custom made subroutine was developed in order to render the control of the morphing trailing edge possible. The PID controller equation (0) is implemented in a subroutine which is interacting with the developed User Element subroutine used for the thermomechanical and time response of the SMA, and the ABAQUS global solver.

$$u(t) = K_P e(t) + K_I \int_0^t e(t) dt + K_D \frac{de(t)}{dt} \quad (0)$$

Terms K_P , K_I , K_D represent the proportional, integral and derivative gain respectively while $u(t)$ represents the manipulated value and $e(t)$ is the error between the measured value and the set point value at each time increment.

In the case of the morphing WTB trailing edge a different PID controller is used for the upward and another one for the downward movement. The manipulated value $u(t)$ is referred to the provided electrical power supplied to each SMA actuator to elevate its temperature. When the trajectory defines that the TE must move upwards the PID controls the power supplied to the top actuator and additionally it defines that the heat exchange with the ambient conditions is dictated by the free convection coefficient. At the same time the controller of the lower actuator cuts off the supplied power and specifies the rate of heat exchange is defined by the coefficient of forced convection, enhancing thus the cooling rate of the antagonistic actuator and facilitating the upward movement. The error $e(t)$ represents the discrepancy of the measured tip displacement and the target tip displacement value.

The Morphing Trailing Edge Concept

The selected trailing edge (TE) morphing rib mechanism concept has been derived from Task 2.2 (Lightweight structural design) and it is presented schematically in Figure 27, where SMA wire actuators are presented with red colour. Summarizing the concept characteristics, the undeformed mechanism shape coincides with airfoil's section original shape. Morphing is achieved by antagonistic SMA actuators which control both upwards and downwards movement as well as the retracting phase. Mechanism parts configuration provides known and adjustable centres of rotation for the flap as connection pin joints between moving parts are located at specific position on airfoil's camber line. Rib's rigidity is provided by the antagonistic actuators, allowing multiple options when it comes to skin design and material selection.

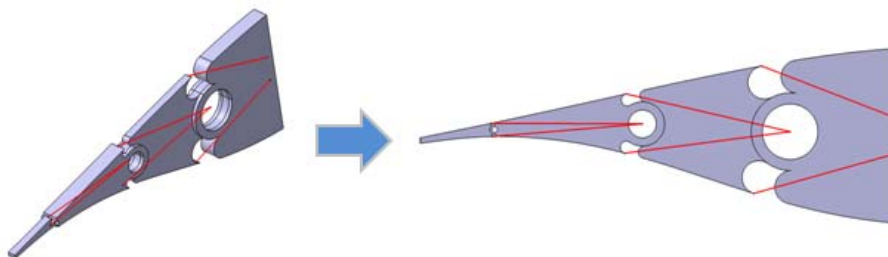


Figure 27: Rib Mechanism with SMA Wire Actuators

The rib structure constitutes of three moving parts connected with hinged pin joints at 10%, 30% and 50% of airfoil chord length, respectively. Although pin positions are expressed in the longitudinal axis in respect of the chordal length the exact position of each pin is located on the original airfoil camber line. Moreover, although each part can be moved independently as a flap, combination of part movement, can lead in an articulated morphed airfoil shape. Flexible elastomeric skin is under consideration in Task 2.2 to bridge the discontinuities caused by the slots and preserve continuity of airfoil aerodynamic surfaces. A three rib mechanism for the full section is shown in Figure 28. Supposing that full section No 75 extends from section No 74 to section No 76 there is one rib on each section plane.

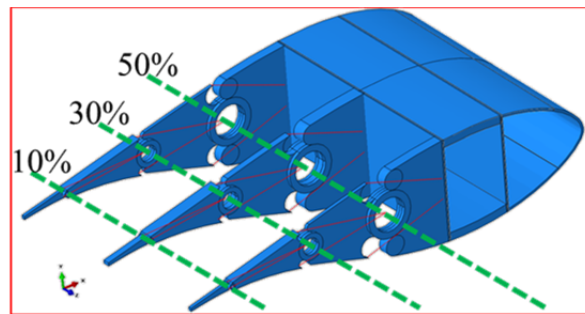


Figure 28: Full Section (Sections 74, 75 & 76) with three (3) Rib Mechanisms

When subjected to heating above A_s SMA wires' martensitic crystal structure transforms to austenite and during the transformation the material tends to return to its parent shape. Because of the boundary conditions applied to each actuator's ends strain develops and the actuator retracts. Each SMA wire ends have specific degrees of freedom restricted. Actuators responsible for moving equivalent flap at 10% of chord length have the ends towards airfoil nose direction pinned on the imaginary axis crossing 30% of chord length as shown in Figure 28. The other end of each actuator is pinned on proper position on equivalent flap at 10% of chord length. During retraction phase of an actuator its length is reduced and because its end towards airfoil nose direction cannot move, as it is pinned on the rotation axis, flap is rotated in the respective direction. In the same manner are connected the actuators moving equivalent flap at 30% of chord length. Finally, the actuators responsible for moving the equivalent flap at 50% of chord length have their ends towards airfoil nose pinned on near shear web. This design for actuators positioning allows each flap to be controlled more easily as it has a specified rotation centre and the actuators influence the movement of only one flap and do not interact with others. In Figure 29 some movement capabilities of the trailing edge rib mechanism are presented.

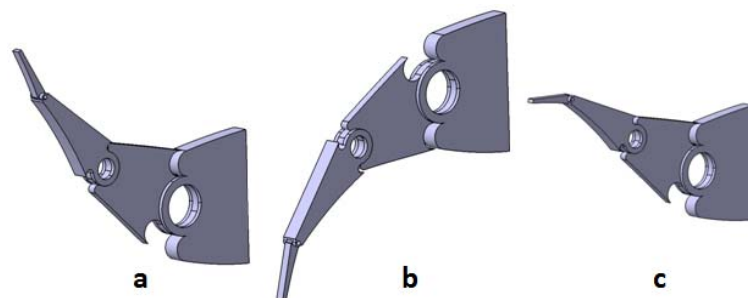


Figure 29: Mechanism Movement Capabilities

a) Movement Upwards b) Movement Downwards c) Combined Movement

Mechanism Functionality Assessment

Airfoil geometry was designed in CATIA software and was modelled in FEA software Abaqus. In Abaqus a specialty subroutine (User Material subroutine-UMAT) implementing an SMA constitutive model [5] was used to simulate the complex thermomechanical response of SMA actuators. The simple adaptive airfoil model with six SMA actuators for each rib mechanism was analyzed in order to assess the effectiveness of the actuators and the feasibility of the concept. Absence of skin was the best case scenario by means that actuators would not have any resistance while moving mechanism parts. The FE analysis was performed for the calculation of the airfoil rib mechanism response under the thermal load (in form of temperature increase from 310.0 K to 350.0 K) applied on the proper SMA wires to deflect mechanism first in downwards and then in upwards direction. Quantitative analyses of the model proved the predicted response of mechanism movement both downwards and upwards as shown in Figure 31, where with black colour initial position and with green colour position after SMA actuators heating are presented.

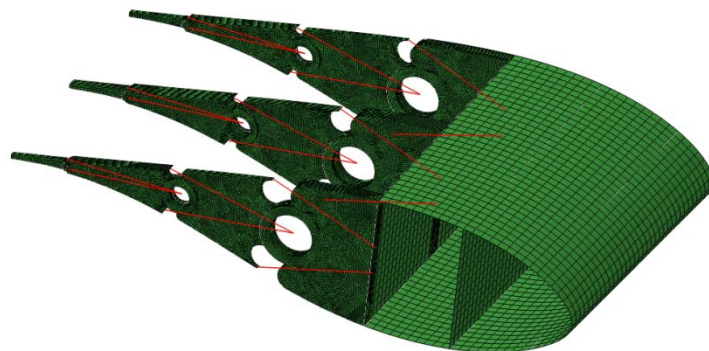


Figure 30: Airfoil and Mechanism Structural Model



Figure 31: Simulation Analysis Results for A. Downwards and B. Upwards Rib Mechanism Movement

Time Response Simulation Input

Although thermomechanical response of SMA actuators proves to be adequate for evaluating mechanism movement capabilities and therefore airfoil morphing, actuators and subsequently mechanism time response is essential for the evaluation of the proposed morphing concept. Time series for specified flap angular movement at 30% of chord length was provided by NTUA (Figure 32). Considering estimations on time intervals between two successive flap angle peaks, time period of this signal was calculated at 6.25 seconds and the absolute maximum angle at 1.98 degrees. The combination of the specified chord length and rotational angle of flap represents a change of 0.15 for lift coefficient.

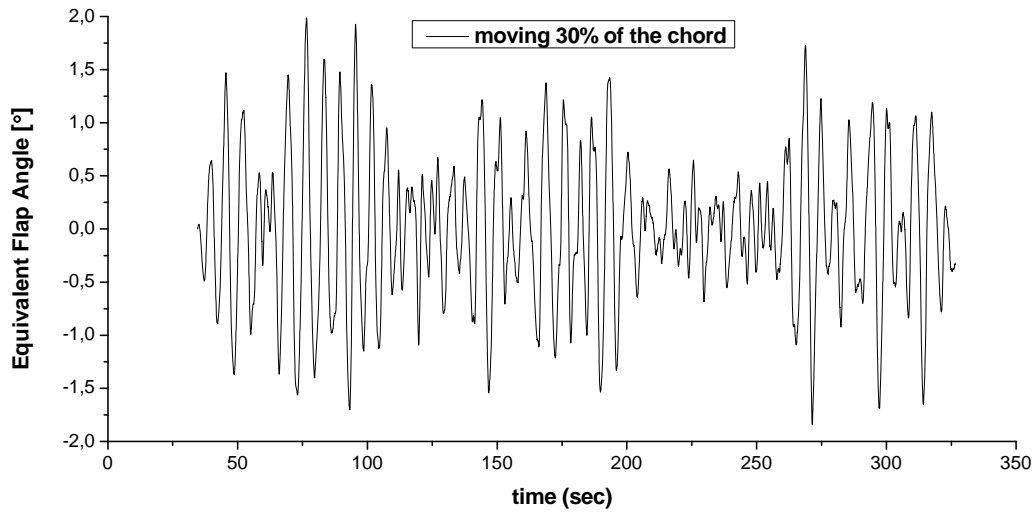


Figure 32: Time Series for Flap corresponding to 30% of Chord Length given by NTUA

Idealized Cosinusoidal Target Trajectory

Considering a flap of length corresponding to 10% of the chord length, modifications were made to simulate airfoil’s response when respective actuators were activated. As a first approach, absolute value of maximum angle was assumed in the time series NTUA provided for 30% of chord length. Using proper charts provided also by NTUA, that relate the percentage of chordal moving length and angular rotation β with the change in lift coefficient (Figure 33), estimation about required angle β when moving 10% of chord length for achieving the same change in lift coefficient was made. Estimated angle was set to 3.6 degrees.

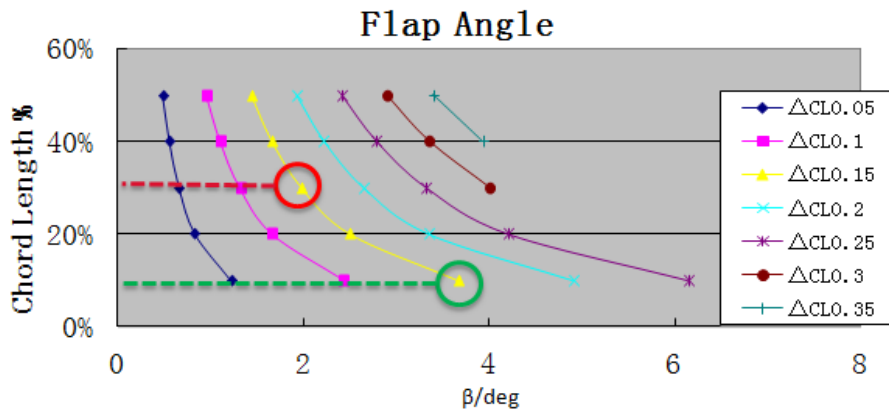


Figure 33: Chart relating Percentage of Moving Chordal Length and Angular Rotation β to Coefficient of Lift Variations

A cosine input signal, shown in Figure 34, for the simulations with amplitude of 3.6, angular frequency $\frac{2 \cdot \pi}{6.25}$ and phase $+\frac{\pi}{2}$ ($3.6 \cdot \left[\cos\left(\frac{2 \cdot \pi}{6.25}\right) + \frac{\pi}{2} \right]$) was created after matching the angular rotation to middle rib’s back end vertical displacement. This modification was made because the PID controller is designed to control the specified displacement. Total time of cosine input signal was set to five periods ($5 \cdot 6.25$ seconds).

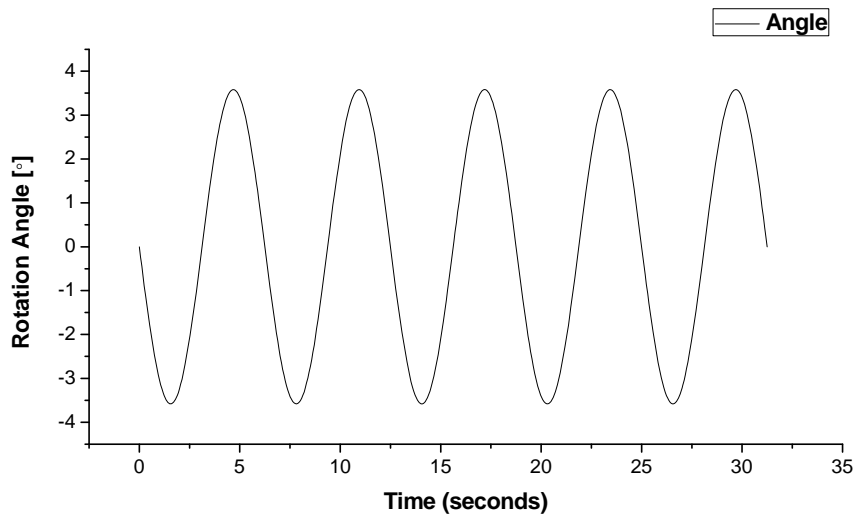


Figure 34: The Five (5) Period Cosine Input Signal

Time Response for Idealized Cosinusoidal Target Trajectory

The ambient temperature was defined to be constant at 295 K and natural convection conditions were assumed. With predefined boundary conditions, simulation was conducted to investigate if the mechanism, driven by the SMA actuators, could follow the input signal. During the simulation, energy offered to the actuators was controlled by the PID controller. Figure 35 presents analysis results concerning vertical movement of flaps.

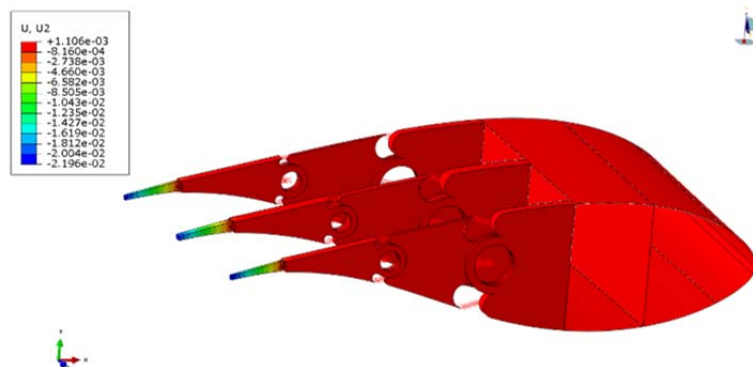


Figure 35: Simulation Results regarding Vertical Displacement (U2)

Following figures (Figure 37 to Figure 40), depict the response of airfoil and actuators during analysis time. Measurements for the data of each figure refer to the SMA actuators of the middle rib which corresponds to the response of the most representative airfoil geometry. Actuator names used in the diagrams are explained in Figure 36.

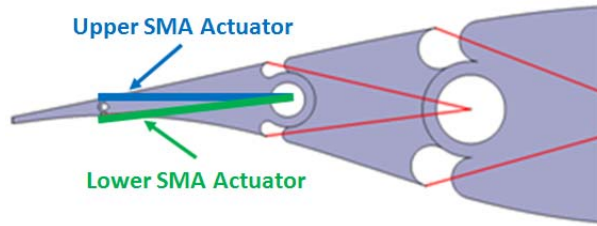


Figure 36: Explanation of SMA actuators Name Definitions

As it is shown in Figure 37, cosinusoidal input trajectory can be followed by the SMA actuators in terms of achieving the right amplitude in the proper time. Although amplitude is not a problem, the ability of the actuator to follow target trajectory as a path is not that adequate. It is clear that as time passes SMA actuators response is delayed about 2÷2.5 seconds, although peak values are achieved in the exact time. This delay in the response may rely on the control variables which were set by trial and error method or the ipso facto response of the actuator.

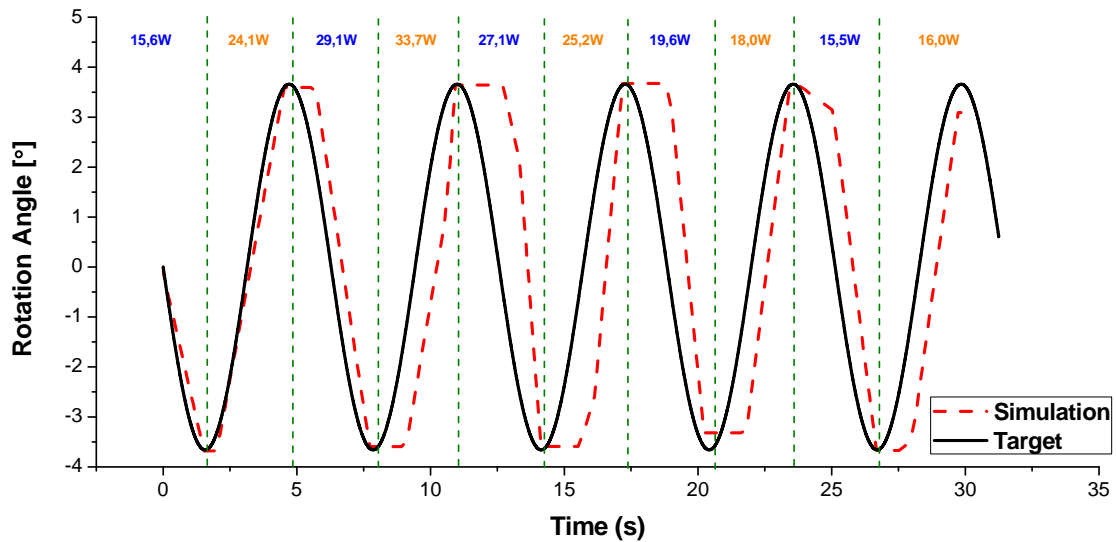


Figure 37: Flap Angular Rotation vs. Time

The major challenge observed in this simulation results was the development of high stresses on actuator section (Figure 38). Stresses seem to saturate on a value of 750÷800 MPa. This range is restricted for SMAs actuators as their yield strength is about 650 MPa and the stress mean value limit for an acceptable fatigue life less than 100 MPa.

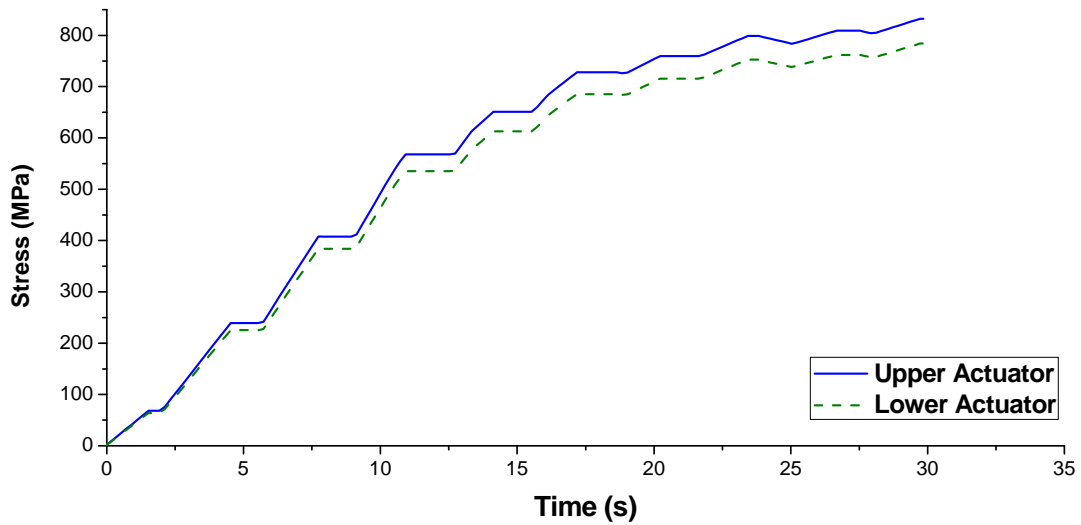


Figure 38: Actuators Stress vs. Time

Another challenge is the constantly increasing temperature required to heat the SMA actuators in order to begin phase transformations. Temperature seems to saturate in values over 440 K. This happens because the SMA actuators are constantly under mechanical loading (developed stress from above diagram indicate it). As mechanical loading increases transformation temperature thresholds also increase. Subsequently, in order to begin a transformation more energy in form of heat is required and this means higher temperature of the actuator.

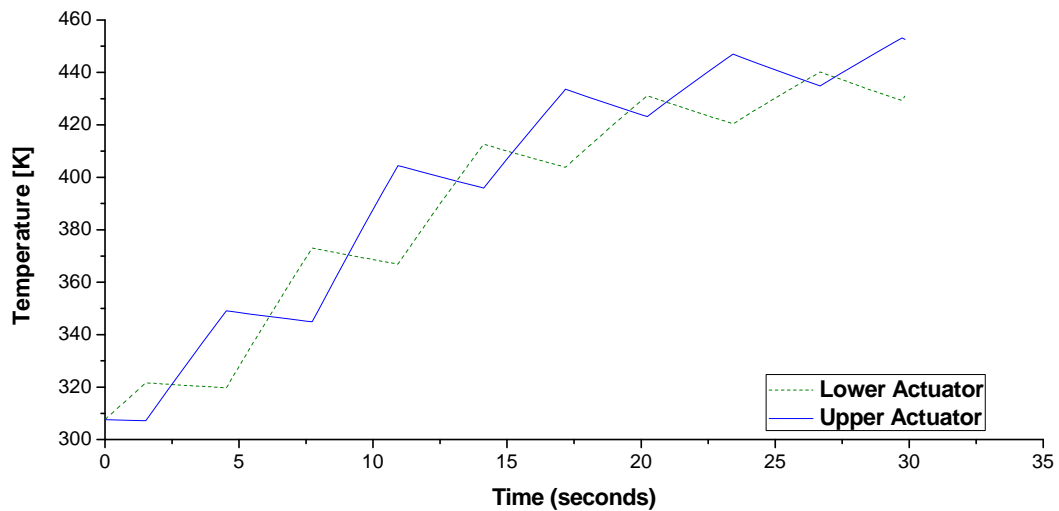


Figure 39: Actuators Temperature vs. Time

From Figure 40 it is clear that for the given conditions SMA actuators tend to have their martensitic volume fraction between 0.3 and 0.5 and they cannot return back to fully martensitic phase ($\xi = 1$). This can be an indication of changing the operating region of the SMA actuators regarding the martensitic volume fraction at initial configuration (no SMA actuator active).

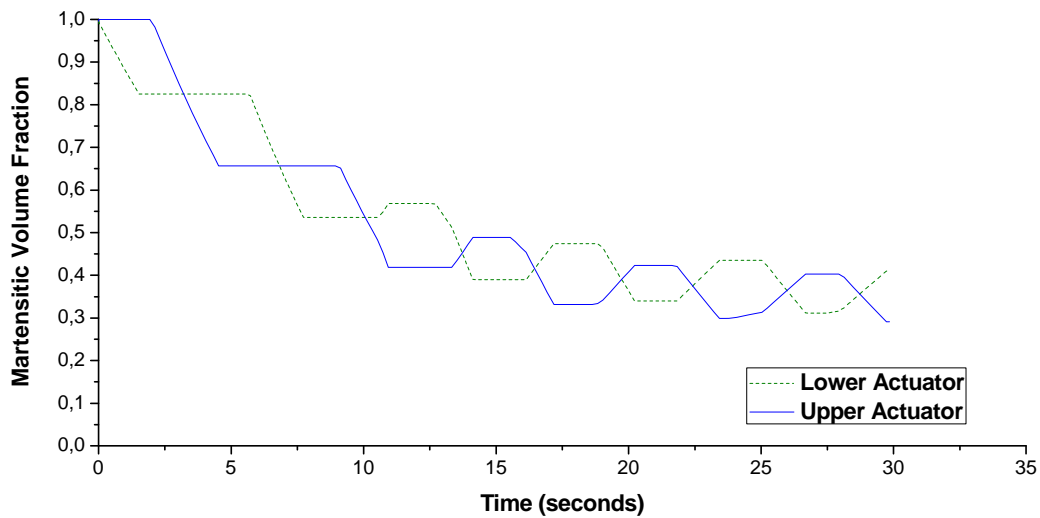


Figure 40: Actuators Martensitic Volume Fraction vs. Time

Actuator Performance Optimization

Challenges were raised from the above analysis, which hinder the feasibility of the SMA actuator. The main challenges were:

- continuously increasing stress of the SMA actuator wires at high levels
- slow cooling rate driven by natural convection that led to high actuation temperature levels
- adverse effect of the above to the actuator time response and power consumption.

To overcome those challenges, possibility of active cooling and change of the operation region of the SMA wire actuators (where shape memory alloy material is partially at martensitic and partially at austenitic phase) were examined. Working SMA regions can be clearly understood when looking at diagrams of Figure 41.

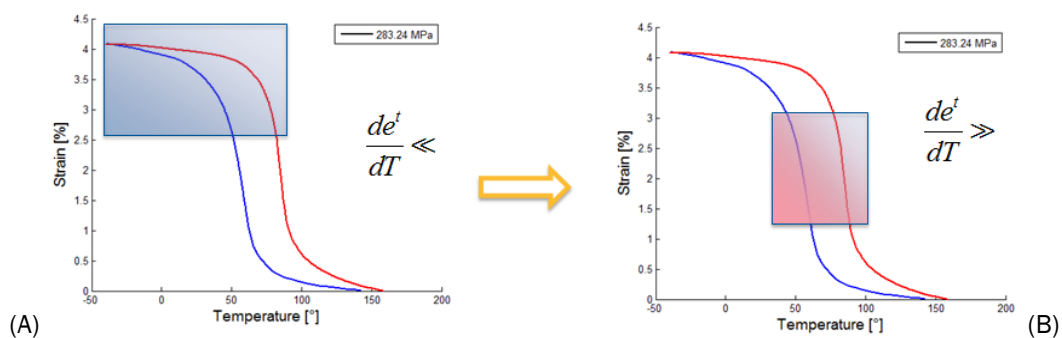


Figure 41: Explanation of SMA actuators Different Working Regions

Figure 41 diagrams present the response of an SMA wire of 1mm diameter during a thermal cycle under constant mechanical load (isobaric experiment). Red coloured curve represents heating phase while blue coloured curve represents the cooling phase. Blue box in Figure 41 (A) indicates the region where the actuators are designed to work so far. Martensitic volume fraction equals 1 (material is at fully martensitic phase) when simulation begins at initial configuration. When the actuator is heated, energy is absorbed to begin the transformation and produce transformation strain. Retraction of

the SMA actuator rotates the flap and morphing is achieved. To return flap in its original position, presuming that antagonistic actuator is not activated, cooling of the previously heated actuator is required. As it may be observed when martensitic volume fraction at initial configuration equals 1 there is a critical temperature difference of about 100°C to achieve the required transformation strain. If the martensitic volume fraction of the actuators at initial configuration was set to another value, for example 0.5, then the required difference in temperature would be reduced to 50°C. It should be noted that although temperature difference is considered the measuring variable, the real variable is the heat provided or rejected by the actuator. This practice of changing martensitic volume fracture of the actuators at initial configuration has multiple advantages. First of all, it provides a faster rate in change of transformation strain in terms of temperature difference. As a result SMA actuators actuation frequency is also increased. It also reduces the required energy by the actuators to develop a predefined strain level. Furthermore, considering that we have antagonistic actuators, the reduced temperature difference during cooling phase, provides substantial time for the actuators to accommodate during their activation and deactivation. Making the last statement more clear, it should be considered a full cycle of flap movement. When the flap is rotated downwards lower SMA actuator is activated while upper SMA actuator is inactive but under tension. During retracting phase, upper SMA actuator is active and lower SMA actuator inactive. At this point cooling rate and fast transformation of lower SMA actuator contributes to minimization of concentrated stresses on lower actuator. Also, the pre tensioning of the upper actuator while was inactive enhances its faster transformation.

Design of Less Time–Consuming FE Model

Full section 3D model simulation including all rib mechanisms, SMA actuators and airfoil parts is highly time consuming (6.25 seconds are simulated in about 45000 seconds or more). A new simulation model focused on a single simplified rib mechanism was designed and assessed in order to reduce simulation time. Respective rib of section 75 (middle) was chosen for standalone modeling as the most representative of the selected airfoil section geometry. Also, efficiency in altering model parameters and further time reduction led to the design of a simplified model based on the geometry of the middle rib corresponding to section 75. Figure 42 shows the rib mechanism with its SMA wire actuators (red colored lines).

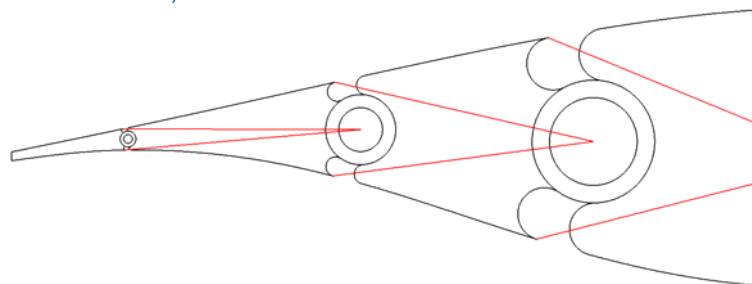


Figure 42: Rib Mechanism and SMA Wire Actuators

In the simplified model only parts that will be considered for simulation are SMA actuators and mechanism parts of one rib. Airfoil parts like shear webs or skin are not necessary for the simulations as they do not move and do not interact with the rib. Figure 43 presents the rib mechanism parts (black sketch), SMA actuators (red lines) and the simplified support structure of the mechanism (green sketch). Support structure is modelled in form of rigid beams with modulus of elasticity 200 GPa and Poisson ration of 0.33. Rigidity of these parts is essential because the main objective is the simulation of time response of SMA actuators and not the study of mechanism parts structure. Additionally, dimensions of the support structure derive from the points where the

actuators are pinned and from the location of rotation axis of the moving mechanism parts.

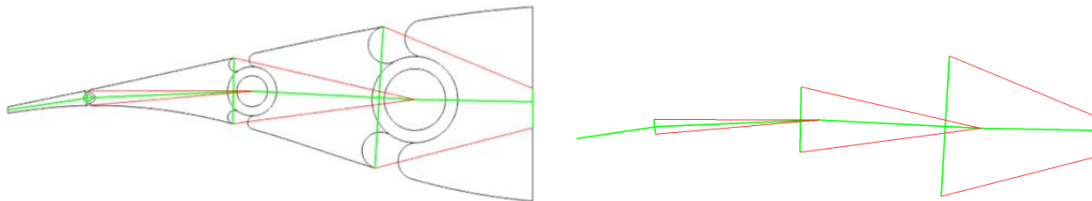


Figure 43: Simplified Structure Design

Mechanism moving parts are modelled as presented in Figure 44 with four rigid parts constituted by rigid beams. Each part is connected with neighbouring parts with MPC pin connections. Red part representing the part that is attached to shear web of the airfoil is fully constrained (clamped). Additionally, all parts, including SMA actuators are constrained to move on the airfoil section plane (2D movement).

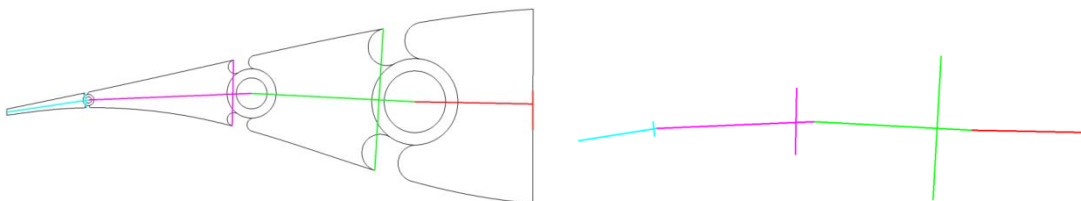


Figure 44: Simplified Support Structure Design

Simulation runs using the 3D rib mechanism took around 25000 seconds, while simulation runs using the simplified model required time up to 7800 seconds for the same input signal. Subsequently, simulation analysis time was reduced around 69%. This is more than expected because simplified model uses less than 200 finite elements, while 3D model uses around finite 38500 elements.

Time Response for Idealized Cosinusoidal Target Trajectory using Optimized Actuators embedded in the Simplified Model

In this section time response of the optimized actuators embedded in the simplified model for an idealized cosinusoidal target trajectory will be presented.

During a thermomechanical cycle, loading of inactive (by means of control) antagonistic actuator is not enough to be subjected to transformation; therefore, it is elastically deformed. Elastic deformation results in high resistance to the movement implied by active actuator. When the SMA actuator is fully at the martensitic phase (100% martensite) there is an energy threshold that must be provided to begin transformation. Energy is absorbed either by heating or by elastic loading of the actuator. Demanding mechanical energy for transformation leads to high developed stresses which, during reverse transformation, are relieved with smaller time rate. This problem can be faced by adjusting the initial martensitic volume fraction of the SMA actuators. With this modification the resistance from antagonistic SMA wire is reduced, as transformation will occur to absorb elastic energy and therefore the required actuation force by the active SMA will decrease. Another benefit is that lower temperature changes will lead to the same effect on the transformation.

Following figures summarize the analysis results when forced air cooling was considered.

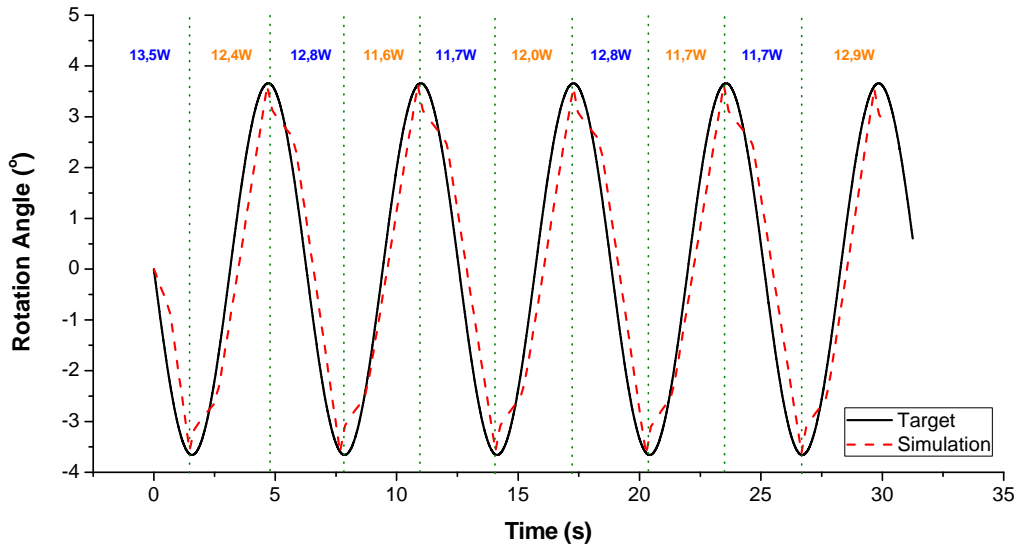


Figure 45: Flap Angle vs. Time

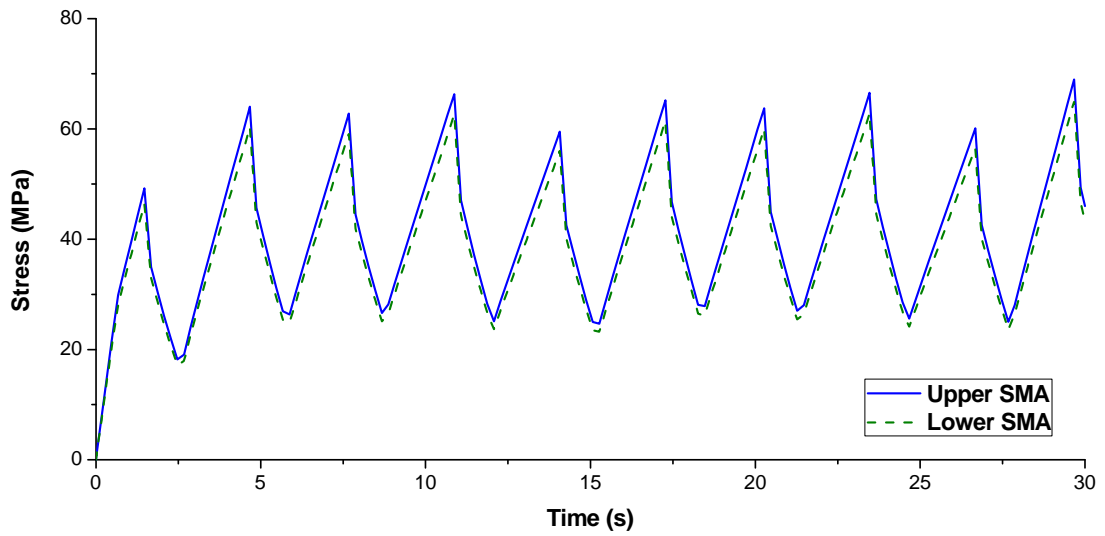


Figure 46: Actuators Stress vs. Time

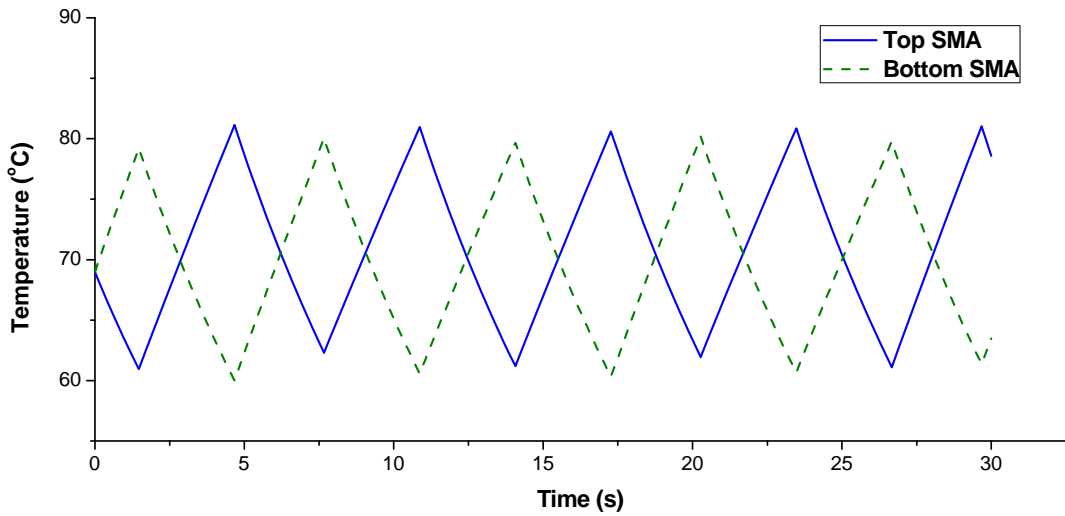


Figure 47: Actuators Temperature vs. Time

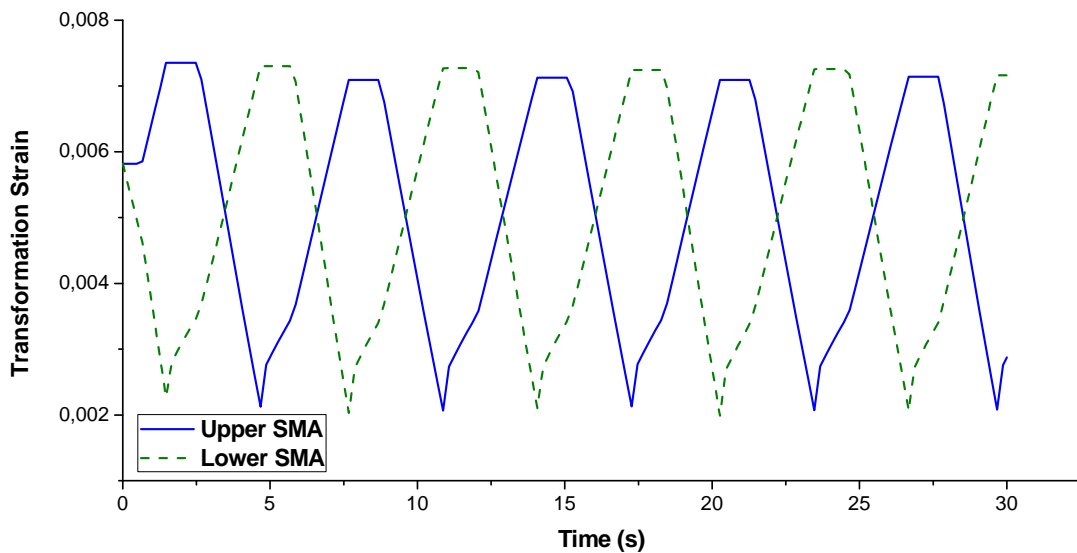


Figure 48: Actuators Martensitic Volume Fraction vs. Time

From the previous results it can be assumed that by changing the working region of the SMA wire actuators and by considering forced cooling conditions at the antagonistic actuators, the stress and temperature levels are saturated at reasonable values proving the feasibility of the concept. Also the power requirements for moving flap seem to reduce by applying pronounced practises.

Validation of Simplified Model and 3D Time Response for Realistic Target Trajectory provided by NTUA

Considering the initial state of the SMA actuators to be 20% at the martensitic phase and 80% at the austenitic active cooling embedded in PID control there was an attempt to follow realistic time series provided by NTUA using optimized actuators. Simulations were performed for both the simplified model and the 3D rib mechanism model to compare their time response and validate the results. Gains of PID controller were defined by trial and error method. Total simulation time was set at 36 seconds and ambient temperature

at 342.0 K. Simulation results are presented in the following figures for both the simplified model and the 3D rib mechanism model.

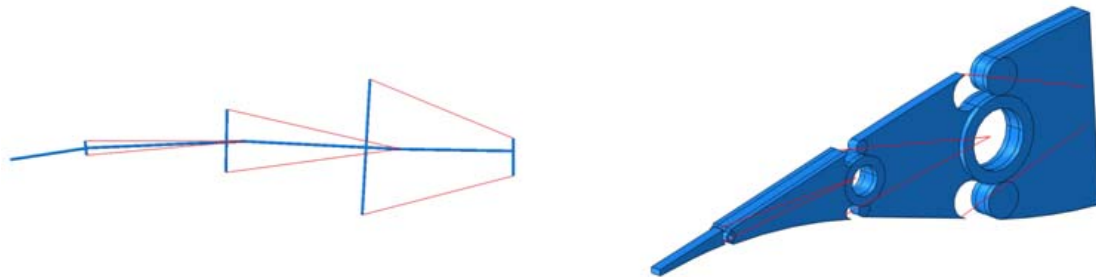


Figure 49: Simplified Model with Actuators and 3D Rib Mechanism Model with Actuators in Abaqus CAE

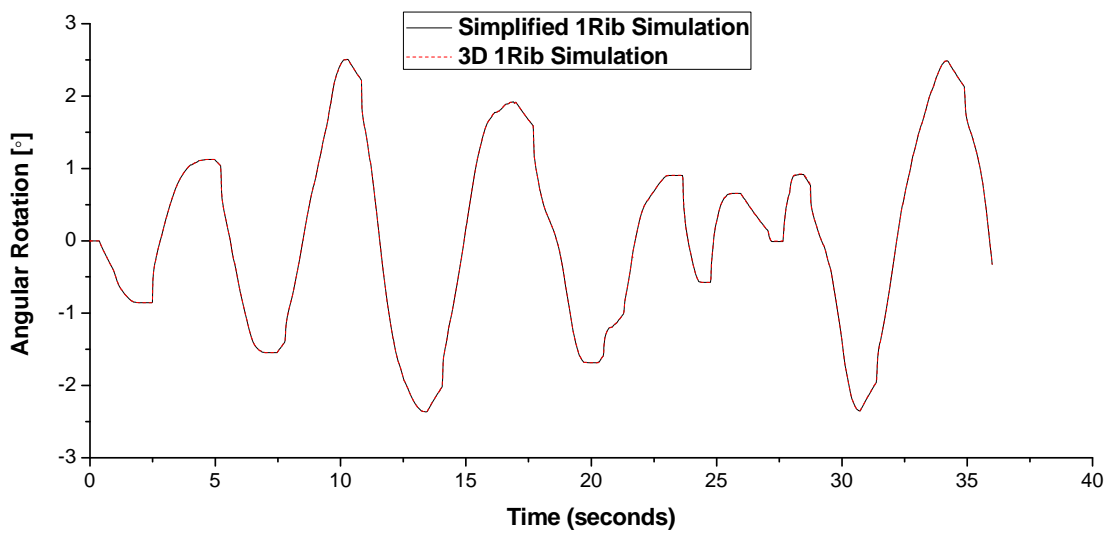


Figure 50: Simplified Mechanism Model and 3D Rib Mechanism Model Angular Rotation Results

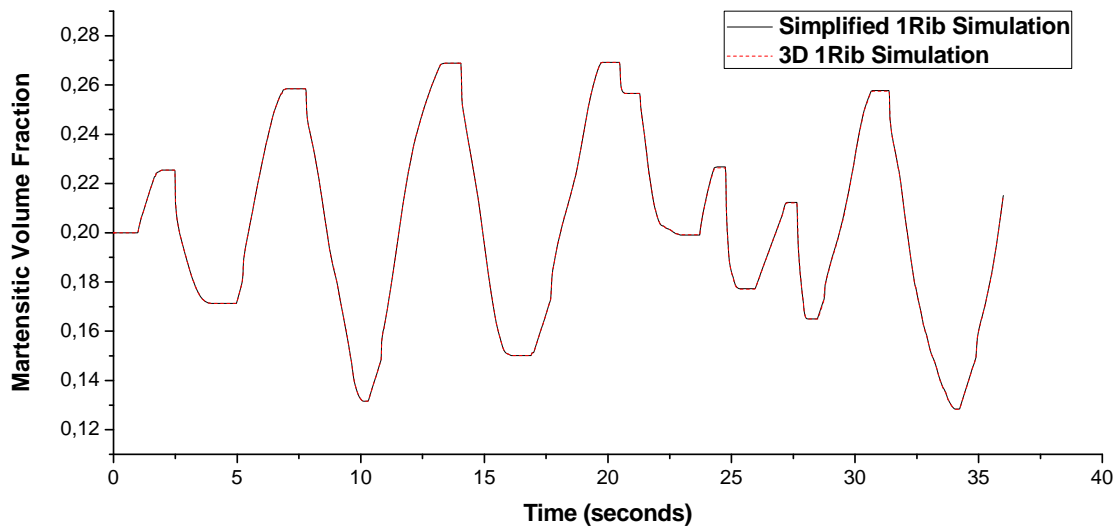


Figure 51: Simplified Mechanism Model and 3D Rib Mechanism Model Upper Actuator Martensitic Volume Fraction Results

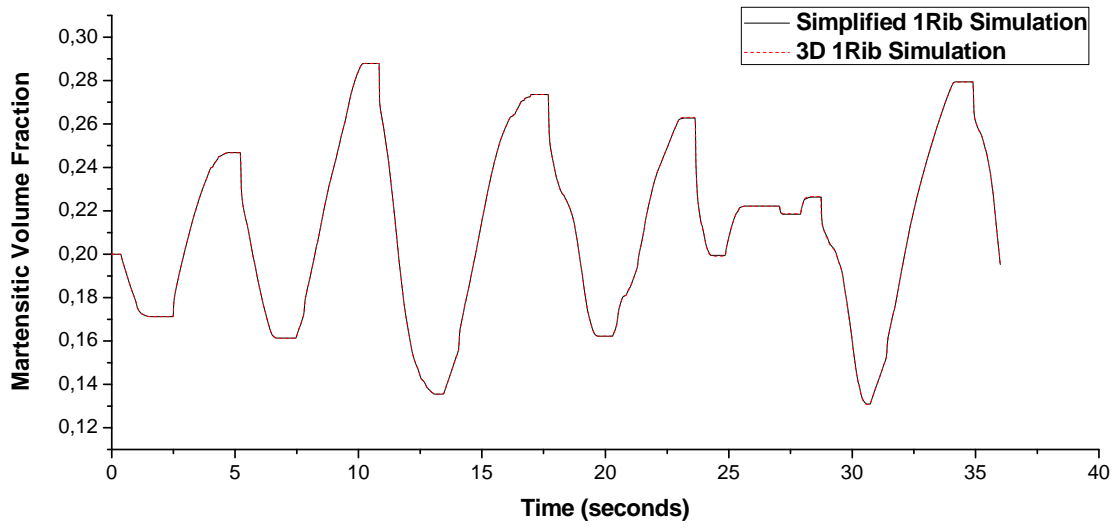


Figure 52: Simplified Mechanism Model and 3D Rib Mechanism Model Lower Actuator Martensitic Volume Fraction Results

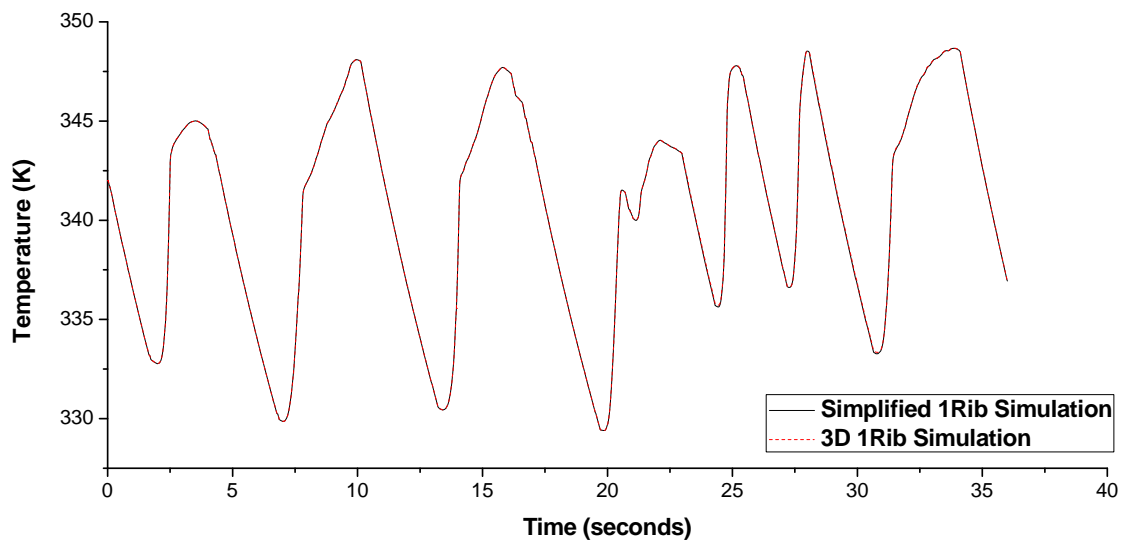


Figure 53: Simplified Mechanism Model and 3D Rib Mechanism Model Upper Actuator Temperature Results

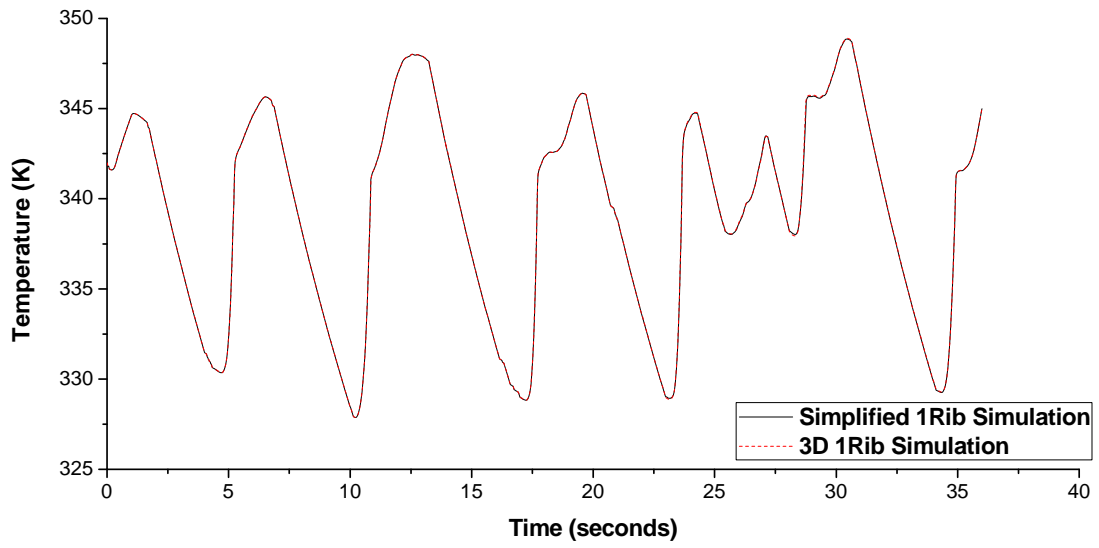


Figure 54: Simplified Mechanism Model and 3D Rib Mechanism Model Lower Actuator Temperature Results

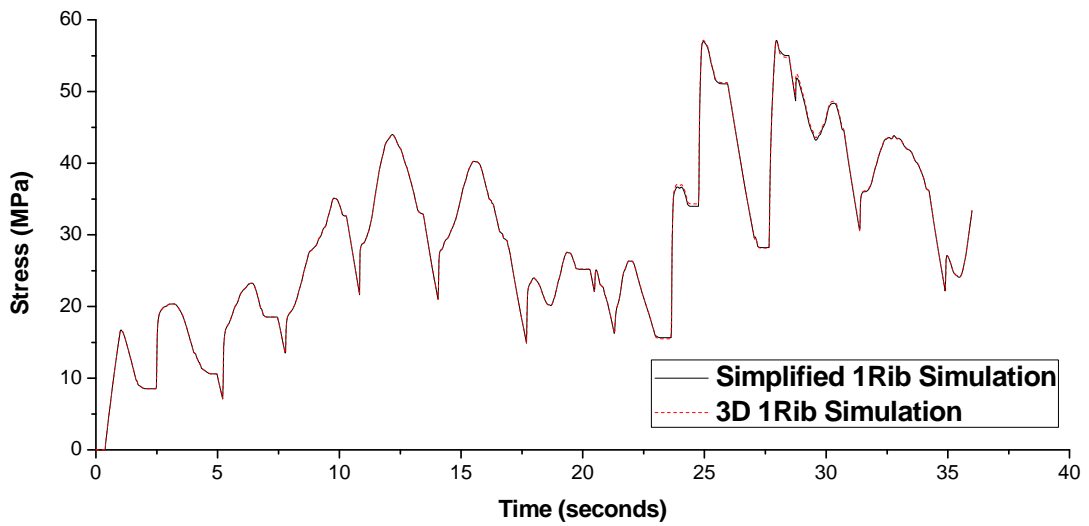


Figure 55: Simplified Mechanism Model and 3D Rib Mechanism Model Upper Actuator Stress Results

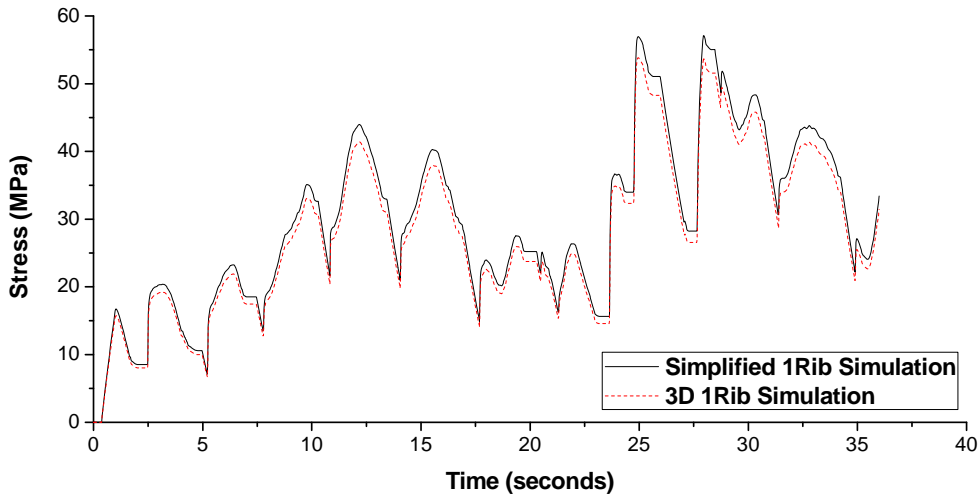


Figure 56: Simplified Mechanism Model and 3D Rib Mechanism Model Upper Actuator Stress Results

As observed the two models have no differences in the produced results except from the developed stresses on the Lower SMA wire actuator where there is a slight difference, but it can be neglected because observed deviation is under 0.07. Therefore, simplified model can be used for testing parameters simulation of the entire rib mechanism.

2.3 Results

Simulation Results for Indicative Time Data (36 seconds)

The following figures describe the simulation results using the simplified model for total simulation time of 36 seconds. In Figure 57 flap response is compared with the input signal and Figure 58 to Figure 60 contain the results of specified variables for both upper and lower actuator for the moving part corresponding to 10% of chord length.

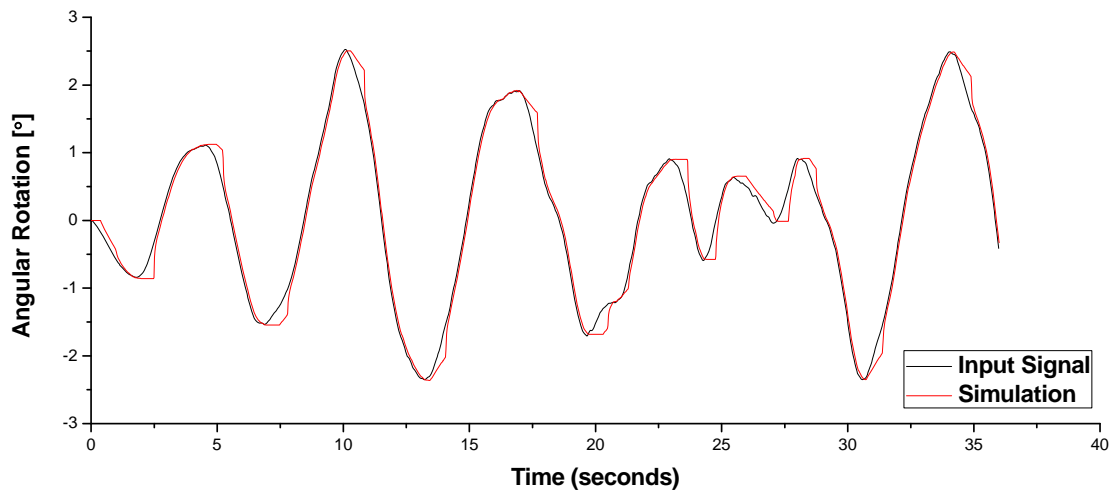


Figure 57: Simplified Model Angular Rotation of Rib Back End vs. Time

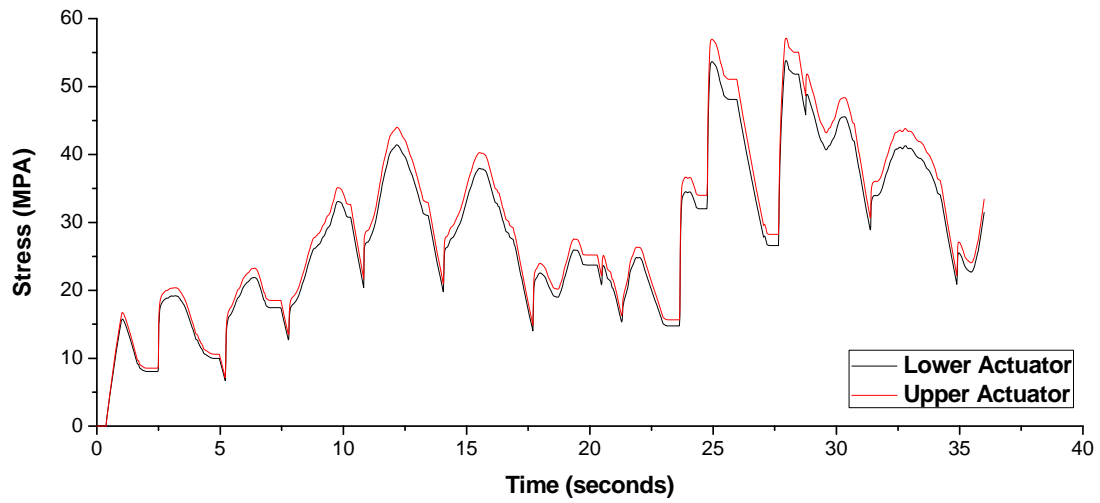


Figure 58: Simplified Model Stress vs. Time

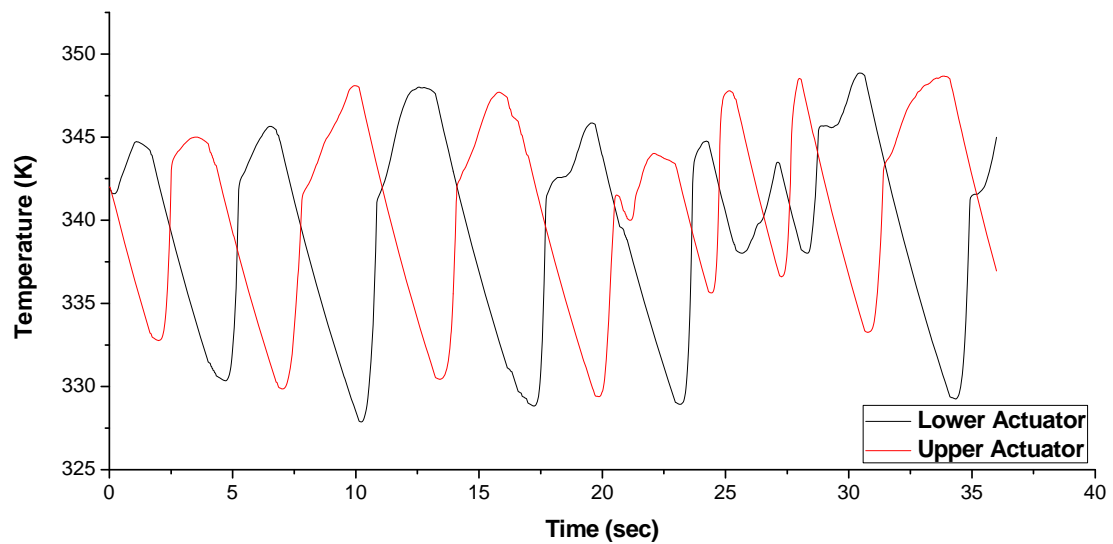


Figure 59: Simplified Model Actuators' Temperature vs. Time

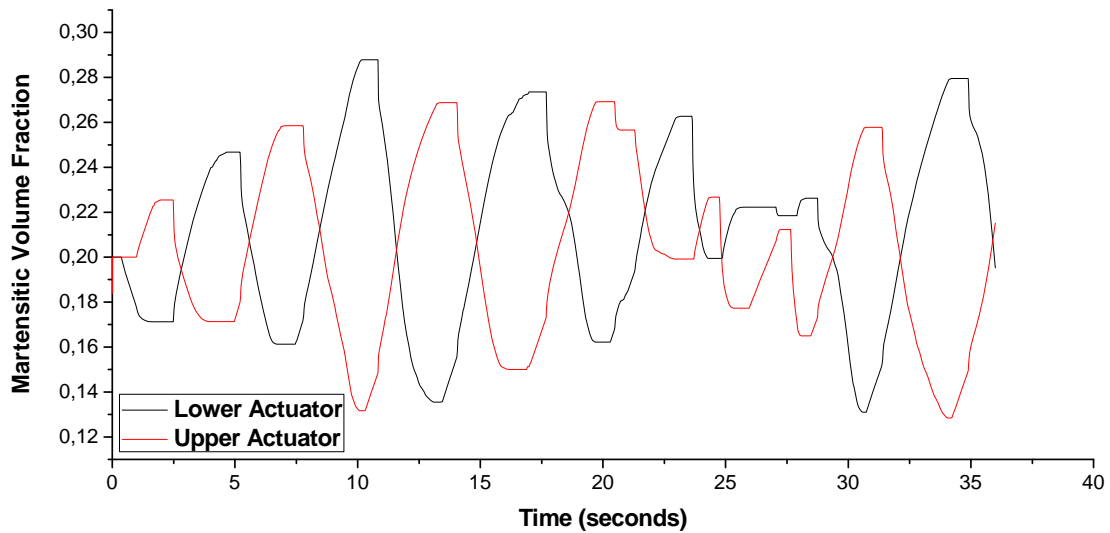


Figure 60: Simplified Model Actuators' Martensitic Volume Fraction (ξ) vs. Time

Simulation of the 3D rib mechanism model with skin on mechanism moving parts (Figure 61) produced exactly the same results as with the 3D rib mechanism model without skin. The result is anticipated because the skin parts added to the structure do not affect mechanism's stiffness and functionality.

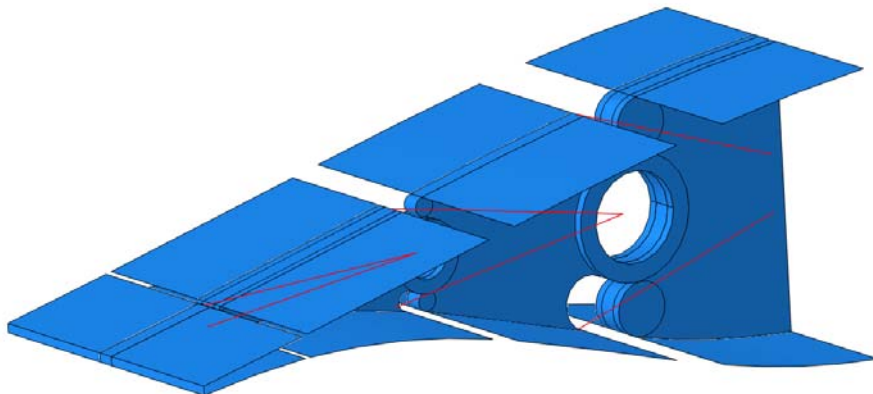


Figure 61: 3D Rib Mechanism with SMA Actuators and Skin Model

Simulation Results for Total Available Time Data (340 seconds)

Finally, simulations using the simplified mechanism model, as it is less time consuming, have been performed for the full input time series data (total time of 340 seconds). As it is proved from Figure 62 the model can follow adequately the predefined signal input trajectory. In high frequencies the flap rotational movement seems to deviate from the optimal. This deviation can be minimized by proper tuning of PID controller gains (k_p , k_d , k_i) either by trial and error or by an optimization function. In present study the only gain that was altered was the gain of proportional controller (k_p) to achieve an effective control. Further study departs from the objective of this one.

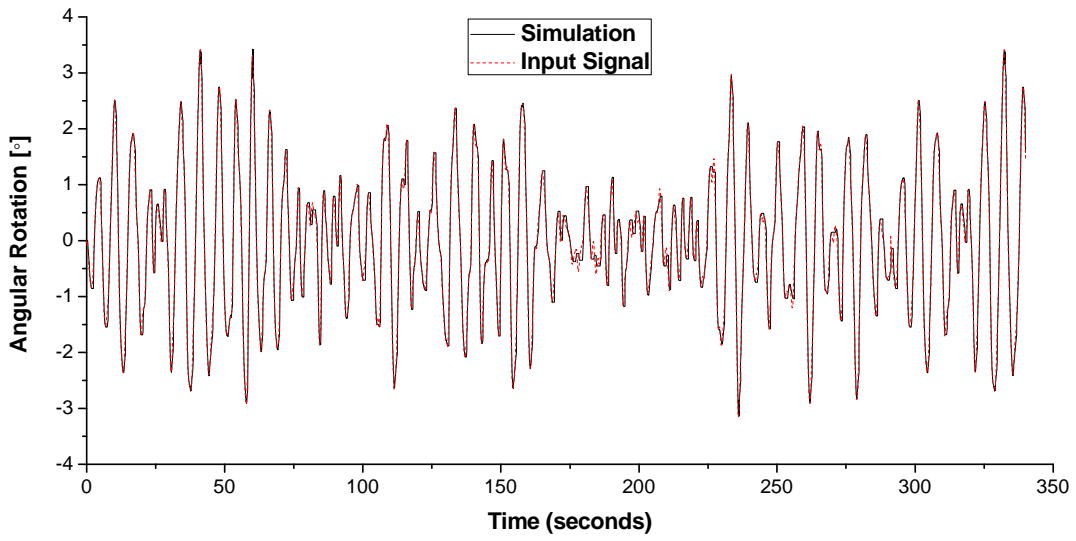


Figure 62: 3D Rib Mechanism with Skin Model Angular Rotation of Rib Back End vs. Time

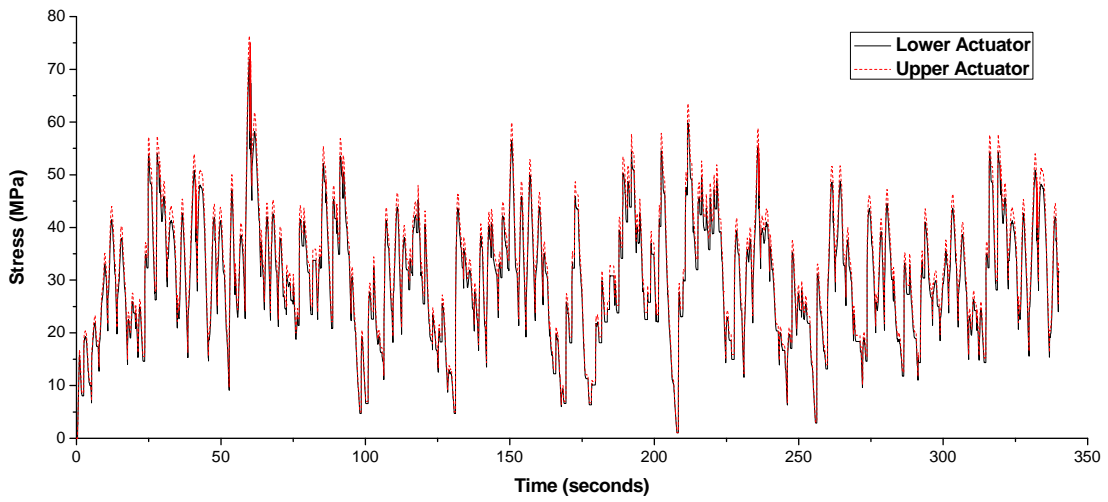


Figure 63: Rib Mechanism with Skin Model Actuators' Stress vs. Time

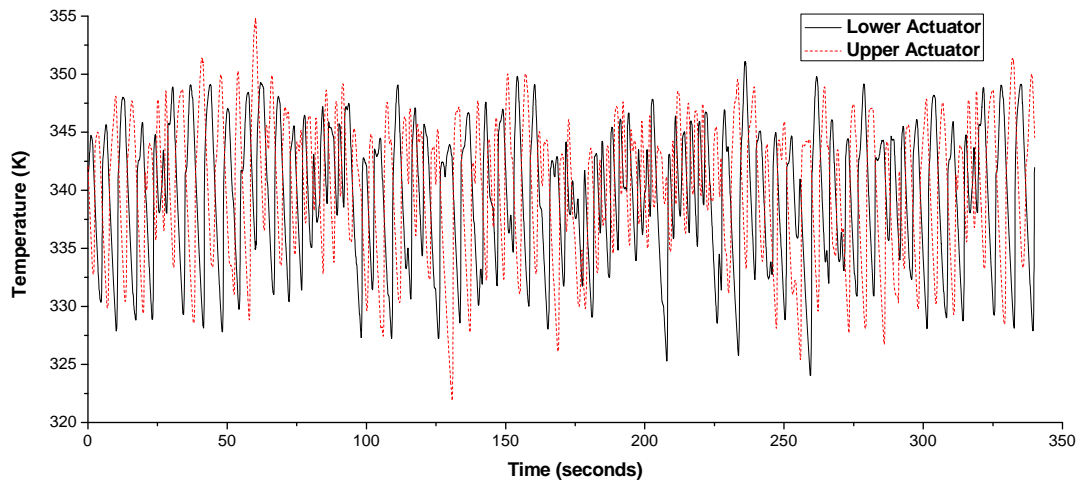


Figure 64: Rib Mechanism with Skin Model Actuators' Temperature vs. Time

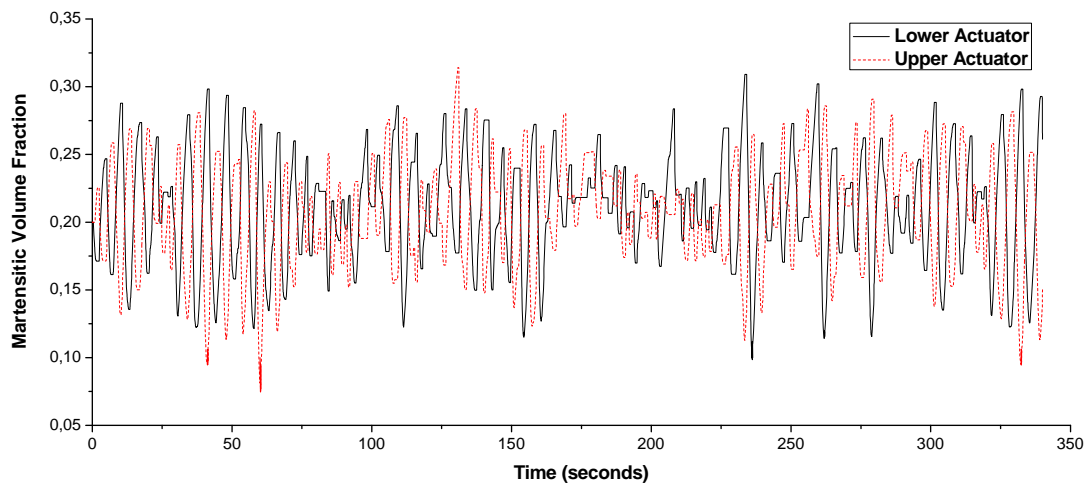


Figure 65: Rib Mechanism with Skin Model Actuators' Martensitic Volume Fraction (ξ) vs. Time

Simulation Results for NTUA Input for Equivalent Flap at 10% of Chord Length

In this section are presented the results from simulation runs setting as input the time series provided from NTUA for an equivalent flap corresponding to 10% of the chord length. This time series does not differ much in terms of periodicity from the one assumed based from the data for equivalent flap at 30% of chord length but it has increased amplitude. In Figure 66 the time series provided by NTUA is presented. With this time series being the target trajectory and PID parameters set simulation runs for the 3D rib mechanism and the simplified model were performed. Total time for the simulation was set to 326 seconds matching the available data.

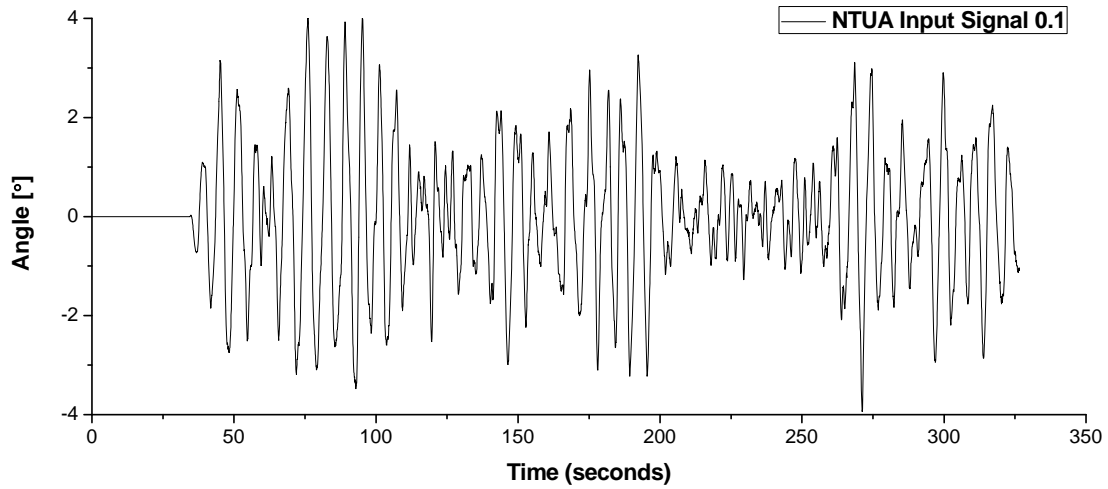


Figure 66: Input Signal provided by NTUA for Equivalent Flap at 10% of Chord Length

Figure 67 is a competitive diagram of the input signal (continuous black curve) with the simulation response (dashed red line). It is clear that the actuators can follow the target trajectory adequately. Main deviations are spotted during the first movement and during angular rotations of about $\pm 2^\circ$ in a high frequency (over 0.5 Hz). With current PID controller set of gains and SMA actuators parameters the mechanism can respond accurately to target trajectories with frequencies up to 0.25 Hz. Further investigation may prove to increase this frequency limit.

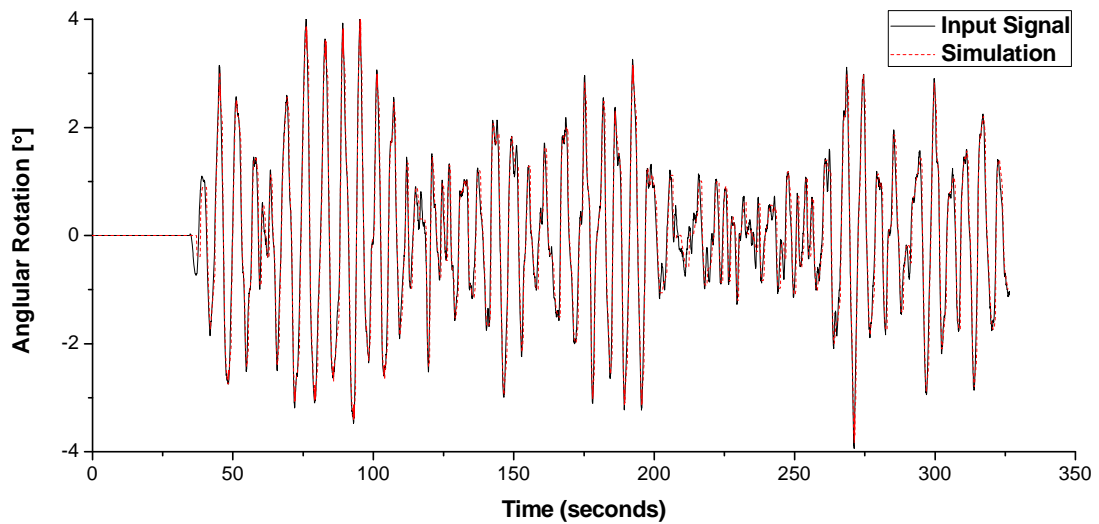


Figure 67: Simplified Model Angular Rotation of Rib Back End vs. Time

As shown in Figure 68 stresses on both upper and lower SMA wire actuators saturate to about 50÷60 MPa, values which are acceptable for the operation of the actuators. Stresses about 110 MPa are developing at the beginning of the analysis and during the first required flap rotation. This is expected to happen because SMA actuators are activated and forced into different thermomechanical conditions.

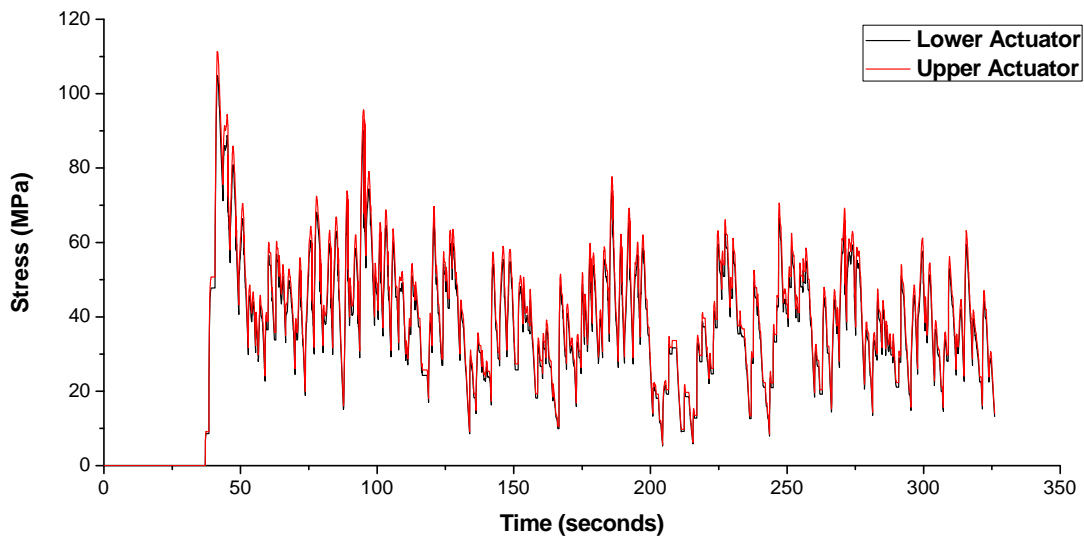


Figure 68: Simplified Model Stress vs. Time

The temperature of the actuators saturates between the values of 325 to 355 K. The temperature range of 30 K is acceptable for the performance of the actuators. It should be noted that the smaller the range of the temperature required and the closest the absolute value of the temperature to the one of the environment the less energy is required for the actuators activation.

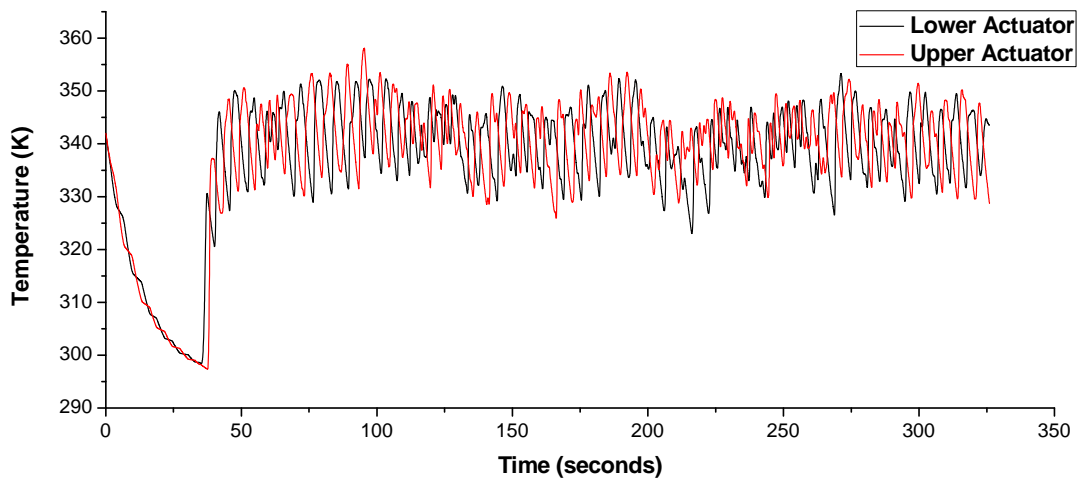


Figure 69: Simplified Model Actuators' Temperature vs. Time

Regarding martensitic volume fraction of the SMA actuators, from Figure 70 it is clear that during the operation of the flap mean value, after transition at the beginning, is the one specified as the initial and operation region ($\xi = 0.2$).

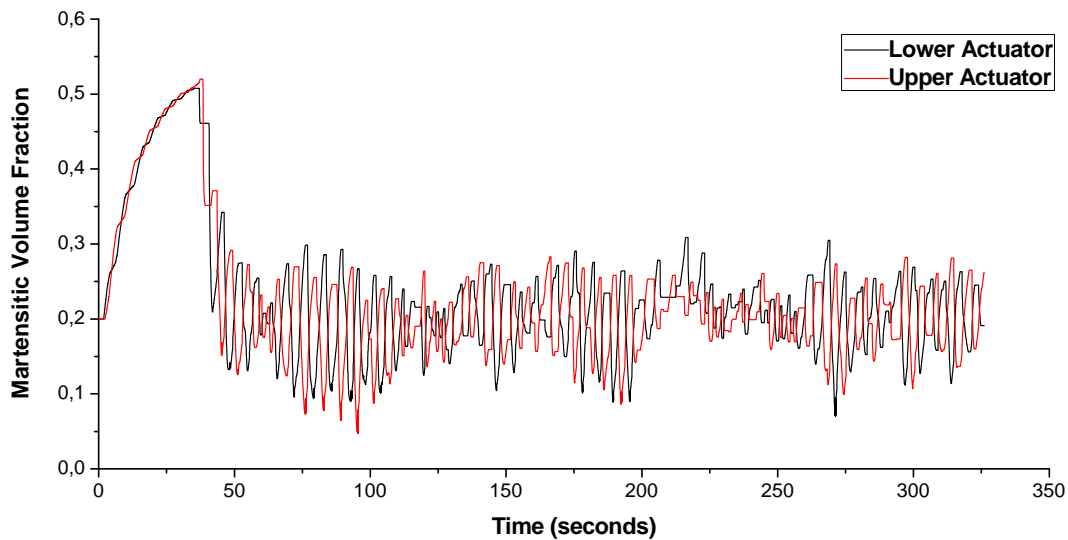


Figure 70: Simplified Model Actuators' Martensitic Volume Fraction (ξ) vs. Time

Finally, Figure 71 presents the power consumption in form of heat to operate with SMA actuators. Maximum power required is around 25 Watts, a value that can be minimized with further tuning of the PID controller and the actuators operating conditions.

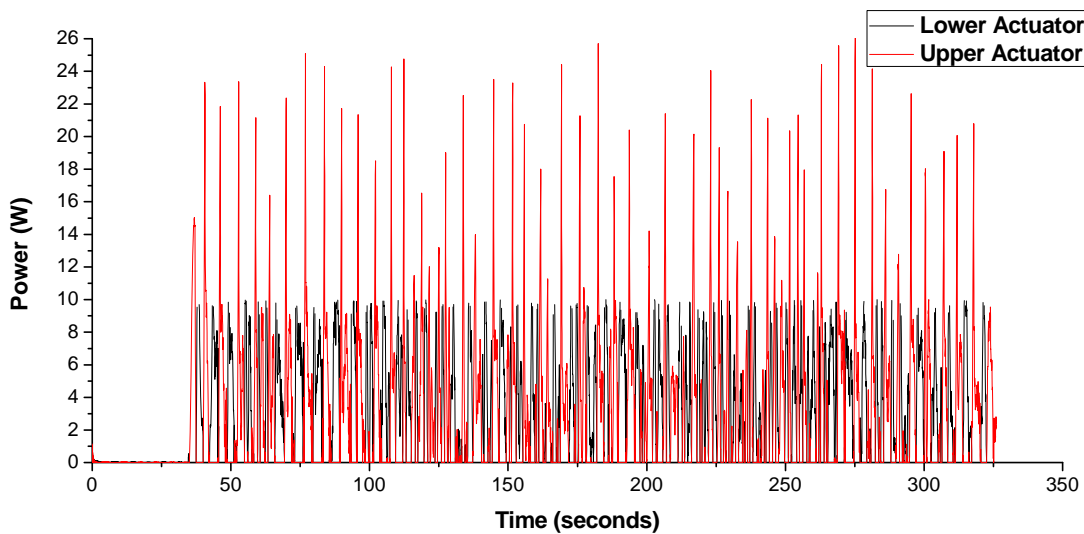


Figure 71: Power Provided to Heat Actuators during Simulation

2.4 Conclusions/Outlook

In the framework of this project a robust design platform for the numerical simulation of a morphing wind turbine blade section trailing edge was developed. The morphing rib mechanism design was derived from WP 2.2.2., and modelled in FEA software Abaqus. A specialty beam finite element capable to simulate the thermomechanical and time response of Shape Memory Alloy actuators was developed and utilized. Thermomechanical response of the SMA wire actuators proved the movement capabilities/limits of the mechanism when actuators were implemented. Target trajectory time series regarding angular rotation of the flap at 30% of chord length were provided by NTUA. From input time series period between two successive peaks and maximum amplitude were extracted. Period and maximum amplitude were used to create

a cosine signal of a total 5 period duration to assess actuators time response. Obtained results proved challenges because developed stresses on SMA actuator wires were continuously increasing, reaching high levels (over 700 MPa), slow cooling rate driven by natural convection led to high actuation temperature levels and subsequently actuators' time response was reduced. It should be mentioned that following this idealized signal required large amounts of power to heat SMA actuators. The aforementioned numerical tool for simulating SMA time response enabled us to overcome serious challenges raised from the initial design such as increased developed stresses and high temperature levels by proper design of SMA actuators. Additionally, a simplified model was designed to simulate the response of the trailing edge rib mechanism with less finite elements. This new model was validated and assessed by comparing results from analyses performed to both simplified model and 3D modelled of the rib. Results proved that simplified model was less time consuming (69% less time required) and more computational effective. Numerous simulations led us to choose the proper working region of the actuators (considering initial martensitic volume fraction of the material) and consider conditions of active cooling to increase the speed of the morphing flap while restricting stress and temperature in reasonable levels. Also minimization of power requirements was possible by using this numerical tool. After NTUA input for flaps corresponding to 30% of chord length were processed properly to correspond to angular rotation of the flap at 10% of chord length new set of simulations was ran. Time for simulation was set to 36 seconds to obtain results to study and export indications regarding actuators performance and variable values. In order to follow required angle trajectory provided by NTUA a subroutine implementing PID control equations was developed. The PID subroutine communicated interacted with the specialty FE and according to the input trajectory provided the adequate power and active or free cooling conditions to the SMA actuators aiming to achieve the target rotation. Furthermore, simulation runs were performed for total time of the available target trajectory (340 seconds). The performed numerical simulations demonstrated the feasibility of the concept using SMA antagonistic actuators to follow the provided trajectory by NTUA. Stresses of the SMA actuators were narrowed in reasonable limits and actuators transformation temperatures, affected by material working region and active cooling, offered the actuator time to adopt and respond in a controlled manner. Finally, NTUA provided time series target trajectory for the equivalent flap at 10% of chord length. This new time series has increased amplitude and this proved challenging. With this input simulation analyses proved that SMA actuators were capable of adequately follow peaks in the required flap movement, but seem require more tuning of PID control variables to increase the sensitivity of the response. Nevertheless, the feasibility of the morphing rib mechanism concept actuated by shape memory alloy wires proved to be feasible and promising.

2.5 References

- [1]. V. A. Riziotis and S. G. Voutsinas, "Dynamic stall modeling on airfoils based on strong viscous-inviscid interaction coupling," *Numerical Methods in Fluids*, vol. 56, pp. 185-208, 2008.
- [2]. P. K. Chaviaropoulos, "Flap/lead-lag Aeroelastic Stability of Wind Turbine Blades," *Wind Energy*, vol. 4, pp. 183-200, 2001.
- [3]. D. C. Lagoudas, Ed., *Shape Memory Alloys Modeling and Engineering Applications*, USA: Springer, 2008.
- [4]. K. Otsuka and C. M. Wayman, *Shape Memory Materials*, Cambridge University Press, 1998.
- [5]. D. Lagoudas, D. Hartl, Y. Chemisky, L. MacHado and P. Popov, "Constitutive Model for the Numerical Analysis of Phase Transformation in Polycrystalline Shape Memory Alloys," *International Journal of Plasticity*, Vols. 32-33, pp. 155-183, 2012.
- [6]. ABAQUS_6, *User Subroutines Reference Manual*, Simulia, 2012.

- [7]. A. M. Qidwai and D. C. Lagoudas, "Numerical Implementation of a Shape Memory Alloy Thermomechanical Constitutive Model using Return Mapping Algorithms," *International Journal for Numerical Methods in Engineering*, vol. 47, no. 6, pp. 1123-1168, 2000.

3 CONCEPT 2: PASSIVE FLAP SYSTEM CONCEPT

3.1 Introduction

In the last years, the increase in wind turbine dimensions has focused the attention on load alleviation techniques. These techniques aim at the reduction of the loads acting on the wind turbine, allowing more efficient structural design. An alleviation of the loads could be achieved by active or by passive techniques. The active techniques rely on an active controller. This system can drive actuators that affect the entire blade, i.e. the pitch actuator, or it can employ distributed devices, such as active flap or plasma actuator placed along blade span, or it can deal with a combination of these systems. In this case a reduction of reliability of the wind turbine is expected due to an increase of the duty cycle of the actuators and to the existence of extra components of the distributed systems.

On the other hand, passive load alleviation techniques affect the system reliability partially, so they seem to be more suitable to wind energy applications. The traditional techniques, such as bend-twist coupling (BTC), have proved their effectiveness but they are unable to react to local noise due to turbulent fluctuation of the wind field. The passive flap concept merges the advantages of the distributed control with the reliability of a passive device. The calibration of the aerodynamic and structural properties of the passive element aims at a reduction of the load without interfering with active control system and other standard wind turbine components.

The first example of a gust-alleviating passive flap can be found in aeronautical field [13]. The experimental setup shows the effects of a long-period dynamically overbalanced flap on an aircraft wind tunnel model. A reduction of the acceleration due to an atmospheric gust is displayed but also a decrease of airplane stability is reported.

Considering rotorcraft applications, an analytic investigation of aeroelastic devices appended to rotor blades is cited in [14]. Among different devices, a passive trailing edge tab concept is shown. The importance of the tuning is highlighted, since the tab motion must be correctly phased to delete the blade harmonic airloading that induces vibrations to the mast. A preliminary simplified analysis is provided, showing promising results. However the device appears to be counter-productive if examined in a more complex framework. The authors do not identify the causes of this mismatch and they suppose that the tab is not tuned properly.

Another passive rotorcraft appended device, similar to the passive flap, is the free tip rotor [15]. The free tip rotor is a conventional rotor except that the blades are modified in the outer part to embed a free pitching tip. This device improves the aerodynamic efficiency, smoothing the airload distribution in the blade tip region when the blade azimuth position is varied. Also in this case the tuning is crucial, as the position of aerodynamic and mass center of the tip relative to the blade pitch axis. Passive control strategies are applied to modulate the torsional moment applied to the free-tip. Different solutions are shown in [16], reporting the sketches of the design concepts.

These studies have shown that the advantage, ensured by a passive device, is overcome by the increase of weight. Therefore, the installation is not convenient in aeronautical and rotorcraft applications, where active systems are preferred despite the loss of reliability. Different requirements characterize wind energy field, where the maximum reliability request is stressed, making the passive flap idea still attractive.

A first application in wind energy of passive distributed system for load alleviation is analyzed in [9]. A passive camber control concept is investigated, considering 2D aeroelastic typical section. The variation of airfoil camber is imposed by local aerodynamic load, while the original shape is restored by concentrate spring and damper. Three simplified load cases are evaluated, showing a significant decrease of load fluctuations.

Passive load alleviation can also be achieved by structural morphing concept as reported in [17]. A bi-stable specimen is designed, tailoring orthotropic material. When the applied load exceed a threshold value, the structure switches from the reference state to the other statically stable state that generates less lift. This process does not require moving parts, but the main drawback is that an active component should be installed on the blade to restore the original shape [18]. For this reason the solution cannot be considered as a purely passive solution.

Despite few studies are reported in literature, passive distributed control requires further investigation for wind energy application. Considering the wind turbine, the project driver is the Cost of Energy (CoE) instead of the weight of rotor blades. So different design approaches can be exploited, making passive distributed load alleviation interesting. Furthermore numerous design solutions can be explored. For example in the reported wind turbine applications, the passive device is moved by aerodynamic loads on the blade section. However, also the structural properties could be exploited to tune the system properly. For this reason all the aero-elastic characteristics are investigated, trying to minimize the negative effects of the appended device on the wind turbine dynamic.

In the first stages of the project, a simplified model is considered to ease the understanding of the phenomenon. A hybrid system is considered, merging the classical typical section theory with the input data provided by a comprehensive wind turbine simulation environment. In the next sections, the model details are given at first, then a description of the model equations is provided. After that, the results are analyzed, assessing system stability, load reduction capabilities and interaction with standard wind turbine behavior. Finally the conclusions are reported and the further developments are suggested.

3.2 Description of the concept

In this task, a passive flap system for load and vibration mitigation is investigated. The advantage of this technique is that a passive flap does not require sensors and actuators and moves only passively in response to blade vibrations. The utility of this technique can be inserted in a more general context of wind turbine design: exploring the feasibility of this system aims at an alleviation of loads and hence, at a reduction of the CoE.

In this preliminary analysis a typical section of the INNWIND blade is studied. A typical section, for a rotating blade, is generally considered at 75% of the blade span (see ref. [1], [9]). A sketch of the blade section with the flap can be viewed in Figure 1.

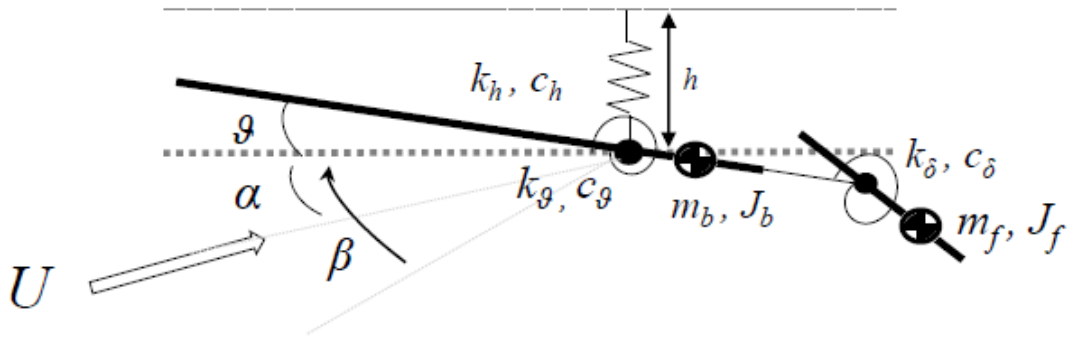


Figure 1: Blade typical section and degree of freedom

The typical section is a simplified 2-D aero-structural model of the blade. The structural properties are obtained by the modal condensation of the blade model, while the aerodynamic loads are evaluated by unsteady strip theory.

Three degrees of freedom are considered:

1. h^*b : plunge, i.e. the vertical deflection of the elastic axis (**EA**) (being b the semi-chord of the airfoil);
2. ϑ : torsional rotation about the elastic axis;
3. δ : deflection of the flap;

In figure 1, α is the angle of attack of the airfoil, β the pitch angle and U the relative wind speed. The springs K_h , K_ϑ and K_δ represent respectively the plunge, the torsional and the flap stiffness. Similarly, C_h and C_ϑ represent the plunge and torsional damping, while C_δ is a damper in the flap hinge. Finally, m_b and m_f are respectively the blade and flap masses and J_b and J_f the moments of inertia.

The aerodynamic model is based on the unsteady 2-D Theodorsen's approach, which includes apparent mass forces as well as the effects of wake vorticity. Considering small disturbance assumption, inviscid and incompressible flow, a closed form solution in the frequency domain can be determined. An equivalent time domain approach is based on Duhamel's integral of Wagner's indicial step responses. The indicial response leads to a linear time invariant (LTI) state space model that can handle arbitrary motion and it allows the application of the LTI system theory (see Ref. [3]).

Problem formulation

In this preliminary analysis, two types of approach have been considered to address the described problem. The first one, based on Theodorsen's theory, is in the frequency domain. The aerodynamic model is combined with structural one as described by the following system:

$$(M_s s^2 + C_s s + K_s) \begin{Bmatrix} h(s)/b \\ \alpha(s) \\ \delta(s) \end{Bmatrix} = qA(s') \begin{Bmatrix} h(s)/b \\ \alpha(s) \\ \delta(s) \end{Bmatrix}, \quad (1)$$

where M_s , C_s and K_s in the left hand side (i.e. the structural part) represent respectively the mass, the damping and the stiffness matrices. In the right hand side (i.e. the aerodynamic part) q is the dynamic pressure and A the aerodynamic matrix, defined as:

$$A(s') = 2b^2(M_{nc}s'^2 + (C_{nc} + \mathbf{C}(s')R_1S_2)s' + K_{nc} + \mathbf{C}(s')R_1S_1), \quad (2)$$

where M_{nc} , C_{nc} , K_{nc} are respectively the non-circulatory apparent mass, damping and stiffness matrices, the products R_1S_2 and R_1S_1 define the circulatory terms, while $\mathbf{C}(s')$ is the complex Theodorsen function, depending on the reduced frequencys':

$$s' = s \frac{b}{U}. \quad (3)$$

With this approach, a stability analysis of the system can be easily conducted including wind speed variation. This approach allows a comparison with the time domain 2D section and a validation of the model.

The second approach is in time domain and goes under the name of Wagner Indicial Response Model. In this approach a state-space model representation of the system is derived. The model is described by:

$$M_s \begin{Bmatrix} \ddot{h}/b \\ \ddot{\alpha} \\ \ddot{\delta} \end{Bmatrix} + C_s \begin{Bmatrix} \dot{h}/b \\ \dot{\alpha} \\ \dot{\delta} \end{Bmatrix} + K_s \begin{Bmatrix} h/b \\ \alpha \\ \delta \end{Bmatrix} = 2qb^2 \begin{Bmatrix} -(Cl^{NC} + Cl^{Circ}) \\ Cm^{NC} + Cm^{Circ} \\ Ch^{NC} + Ch^{Circ} \end{Bmatrix}, \quad (4)$$

where the terms in the right hand side are:

- Cl^{NC} , Cm^{NC} , Ch^{NC} the aerodynamic non-circulatory (NC) terms,
- Cl^{Circ} , Cm^{Circ} , Ch^{Circ} the aerodynamic circulatory (Circ) terms.

The NC terms can be written in matrix form and correspond to the matrixes M_{nc} , C_{nc} , K_{nc} in $A(s')$ of the Theodorsen's formulation. The circulatory terms are defined as:

$$Cl^{Circ} = Cl_{/\alpha} \left[\alpha_{QS}(0)\varphi(\tau) + \int_0^\tau \frac{d\alpha_{QS}(\sigma)}{d\sigma} \varphi(\tau - \sigma) \right] + Cl_{/\delta} \left[\delta_{QS}(0)\varphi(\tau) + \int_0^\tau \frac{d\delta_{QS}(\sigma)}{d\sigma} \varphi(\tau - \sigma) \right] \quad (5)$$

$$Cm^{Circ} = (a + \frac{1}{2})Cl^{Circ} \quad (6)$$

$$Ch^{Circ} = Ch_{/\alpha} \left[\alpha_{QS}(0)\varphi(\tau) + \int_0^\tau \frac{d\alpha_{QS}(\sigma)}{d\sigma} \varphi(\tau - \sigma) \right] + Ch_{/\delta} \left[\delta_{QS}(0)\varphi(\tau) + \int_0^\tau \frac{d\delta_{QS}(\sigma)}{d\sigma} \varphi(\tau - \sigma) \right] \quad (7)$$

where $Cl_{/\alpha}$ and $Ch_{/\alpha}$ represent the slopes of the lift and of the hinge moment curves, $Cl_{/\delta}$ and $Ch_{/\delta}$ the slopes wrt the flap deflection and a the distance (in semi-chords) between elastic axis and the half chord of the section (the value is positive going from the leading edge to the trailing edge). The other terms are:

- $\tau = t \frac{\text{Wind Speed}}{b}$ is the reduced time;
- $\alpha_{QS} = U\alpha + \dot{h} + b \left(\frac{1}{2} - e \right) \dot{\alpha}$ is the equivalent quasi-steady angle of attack;
- $\delta_{QS} = \frac{1}{\pi} (T_{10} - LT_{21})U\beta + \frac{1}{2\pi} b (T_{11} - 2LT_{10}\dot{\beta})$ is the equivalent quasi-steady flap angle;

- $\varphi(t) = 1 - 0.165e^{-0.0455\tau} - 0.335e^{-0.3\tau}$ is the R. T. Jones approximation of the Wagner function (see Ref. [3]);

This model reproduces the unsteady aerodynamic effects due to an arbitrary motion of the 2D section. In a similar way, aerodynamics generated by an indicial vertical speed variation can be described with the Küssner's function, with the addition of a contribute related to the forcing term. This modifies the previous problem as:

$$(8) \quad M_s \begin{Bmatrix} \ddot{h}/b \\ \ddot{\alpha} \\ \ddot{\delta} \end{Bmatrix} + C_s \begin{Bmatrix} \dot{h}/b \\ \dot{\alpha} \\ \dot{\delta} \end{Bmatrix} + K_s \begin{Bmatrix} h/b \\ \alpha \\ \delta \end{Bmatrix} = 2qb^2 \begin{Bmatrix} -(Cl^{NC} + Cl^{Circ} + Cl^{Gust}) \\ Cm^{NC} + Cm^{Circ} + Cm^{Gust} \\ Ch^{NC} + Ch^{Circ} + Ch^{Gust} \end{Bmatrix}$$

where Cl^{Gust} , Cm^{Gust} and Ch^{Gust} are defined as following:

$$Cl^{Gust} = Cl_{/\alpha} \left[\alpha_G(0)\psi(\tau) + \int_0^\tau \frac{d\alpha_G(\sigma)}{d\sigma} \psi(\tau - \sigma) \right], \quad (9)$$

$$Cm^{Gust} = \left(a + \frac{1}{2} \right) Cl^{Gust}, \quad (10)$$

$$Ch^{Gust} = Ch_{/\alpha} \left[\alpha_G(0)\varphi(\tau) + \int_0^\tau \frac{d\alpha_G(\sigma)}{d\sigma} \varphi(\tau - \sigma) \right], \quad (11)$$

and the term $\psi(\tau) = 1 - 0.5e^{-0.130\tau} - 0.5e^{-1.0\tau}$ represents an approximation of the Küssner's function (Ref. [3], [8]).

Finally, after mathematical manipulation of the previous equations, the system model can be reduced in a linear dynamic MIMO system:

$$\dot{x} = Ax + bu \quad (12)$$

being x the state vector, containing the structural and the aerodynamic states. The structural degrees of freedom include the plunge displacement, the torsional rotation, the flap rotation and their first derivatives in time. The aerodynamic states are related to the Indicial Response, including the R.T. Jones's approximation of the Wagner's function (Ref. [3], [8]), and the Küssner's function for unsteady loads. The input vector u contains the angle of attack and the collective pitch actuation.

Starting from the state-space formulation of the system, numerical simulations at different wind speeds can be set up in order to evaluate the effects of the passive flap.

Flap Optimization

Tuning process of the passive flap is performed by an optimization procedure that considers aeroelastic properties of the wind turbine blade. Two considerations drive this procedure:

Flap eigenvalues spread minimization. The aeroelastic model properties of the flap are strictly dependent on wind speed. This fact is found to be a concern: the spread due to aerodynamics might let the flap mode become unstable for high wind speeds. This fact imposes a lower bound on the tuned stiffness, and this may results in a reduced

effectiveness of the system at low velocities. This phenomenon is mitigated by the reduction of the spread due to aerodynamics, decreasing the dependency of the flap mode to the wind speed. These considerations bring to size the hover-hang flap length, in order to cancel out the non-circulatory and circulatory terms related to the flap deflection. Considering the expression (2), these terms are, respectively, K_{nc}^{33} and $R_1^3 S_1^3$. The last term equal to zero, satisfies also the balancing condition, as reported in [6].

Damage Equivalent Load minimization. An estimation of the effects of the passive flap on the fatigue life is assessed by the evaluation of the damage equivalent loads (DEL). The DEL induced by the plunge motion is taken into account. The procedure starts with the evaluation of the DEL by the model of eq. (12). Several wind speeds are considered, exploring all the power production range. The time histories are processed by the *rainflow* counting technique, obtaining the matrix \mathcal{M} , where the element m_{ij} ($V_p < V_0 < V_{p+1}$) denotes the number of cycles in the mean stress interval $h_{m,i} < h_m < h_{m,i+1}$ and range interval $h_{a,j} < h_a < h_{a,j+1}$ for the wind speed interval $V_p < V_0 < V_{p+1}$. Then, assuming the annual wind distribution in terms of Weibull's probability function, the DEL for the plunge load is estimated using the procedure explained in [10].

Interaction with control system

This analysis aims to understand how the passive flap affects the AEP, providing a preliminary measurement of the interaction between the passive system and the active control system of the wind turbine. This estimation must consider the trim condition and the behaviour of the control system that prescribes the regulation strategy. The 2D linear typical section system is not able to provide these measurements because it estimates only the variations from a reference condition inferred from Cp-Lambda multibody simulations. For this reason, the effects induced by the passive flap on the AEP are examined by a model that includes the trim controller and rotor dynamic. A collective-pitch non-linear wind turbine reduced model is applied. The model includes tower fore-aft motion, actuators dynamic and drive train shaft dynamic and it is represented by the following equations:

$$M_T \ddot{d} + C_T \dot{d} + K_T d - F_a(\Omega, \beta_e, V_w - \dot{d}, V) = 0 \quad (13)$$

$$(I_{LSS} + I_{HSS}) \dot{\Omega} + T_l(\Omega) - T_a(\Omega, \beta_e, V_w - \dot{d}, V) = 0 \quad (14)$$

$$\dot{\beta}_e + 2\xi\omega\beta_e + \omega^2(\beta_e - \beta_c) = 0 \quad (15)$$

$$\dot{T}_{el_e} + \frac{1}{\tau}(T_{el_e} - T_{el_c}) = 0 \quad (16)$$

The first equation represents the tower dynamic where d is the fore-aft motion of the tower top and F_a is the aerodynamic longitudinal force. The M_T , C_T and K_T are modal mass, damping and stiffness of the tower obtained by a modal reduction of a finite element model of the tower structure. The second equation expresses the drive train dynamic: Ω is the rotor angular velocity, T_l is the torque due to mechanical loss and T_a is the aerodynamic torque. I_{LSS} and I_{HSS} represent the overall rotor inertia relative respectively to the low speed and to the high speed shaft. T_{el_e} and β_e are the electrical torque and the collective-pitch obtained by the last two equations that express the dynamic behaviour of the actuators, filtering the required input torque T_{el_c} and collective-pitch β_c . A picture of the model is reported in **Error! Reference source not found.**, while further details are available in [19].

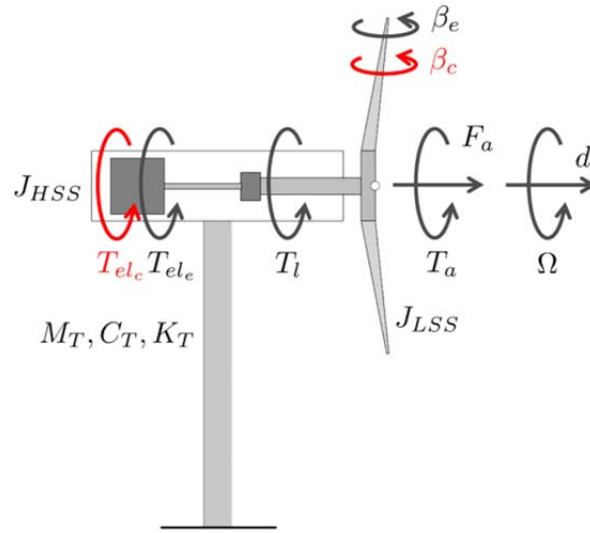


Figure 2, Reduced model to estimate power production effects due to passive flap

The aerodynamic torque T_a and the aerodynamic force F_a are computed as:

$$T_a = \frac{1}{2} \rho A R \frac{C_P(\lambda, \beta_e, V)}{\lambda} (V_w - \dot{d})^2 + T_{a,flap} \quad (17)$$

$$F_a = \frac{1}{2} \rho A C_F(\lambda, \beta_e, V) (V_w - \dot{d})^2 + F_{a,flap} \quad (18)$$

where ρ is the air density, A is the rotor area, R is the rotor radius, V_w is the wind speed and λ is the tip speed ratio. The aerodynamic coefficients C_P and C_F are known by look up tables and they are obtained by static Cp-Lambda analysis. Finally $T_{a,flap}$ and $F_{a,flap}$ are the contributes to aerodynamic forces and moments due to the passive flap. These contributes are computed by the 2D unsteady sectional model described in the previous chapter, using the data obtained by Cp-Lambda dynamic analysis. Obviously the motion of the passive flaps is influenced by β_c and T_{elc} imposed by the trim controller. However, it is made the assumption that the aerodynamic forces, obtained by the 2D typical sectional analyses, are representative of the flap behaviour over the entire power production range even if the β_c and T_{elc} imposed by the trim controller are varied. This hypothesis allows to compute the flap response for each blade, considering the original measurements obtained by Cp-Lambda simulations. The pre-calculated effects of the flaps are then applied to the reduced model, during the simulations that include the trim controller.

$T_{a,flap}$ and $F_{a,flap}$ are obtained by the aerodynamic distributed loads computed by the 2D analyses. The distributed loads are assumed constant along the span wise extension of the flap, so $T_{a,flap}$ and $F_{a,flap}$ are obtained by the superposition of the forces generated by each passive flap, projected into normal and tangent direction to the rotor plane.

Knowing $T_{a,flap}$ and $F_{a,flap}$, it is possible simulating the complete power production range, linking the nonlinear wind turbine model with an LQR controller synthetized as reported in [19]. These simulations are compared with the measurements obtained by the reduced system when the terms $T_{a,flap}$ and $F_{a,flap}$ are switched off, providing a rough estimation of the passive flap effects on the reference conditions and on the AEP. Further developments will include the dynamic of the passive flaps into the nonlinear

reduced model, linking the noises $T_{a,flap}$ and $F_{a,flap}$ to the rotor dynamic and to the trim controller.

3.3 Results

Procedure Validation

In order to validate the procedure, a stability analysis has been performed on a typical section using both the models described above. Starting from the system defined in the frequency domain, the p - k iterative method in the calculation of the eigenvalues is used. On the other side, using the state space representation of the system, a direct calculation of the A matrix eigenvalues can be easily performed. These computations have been derived for different wind speed values. The section parameters used in this preliminary validation analysis are not yet optimized (see next section).

Figure 3, shows the root loci of the eigenvalues for different section speed values from 0 to 80m/s, the latter being the 120% of the rotor rated speed.

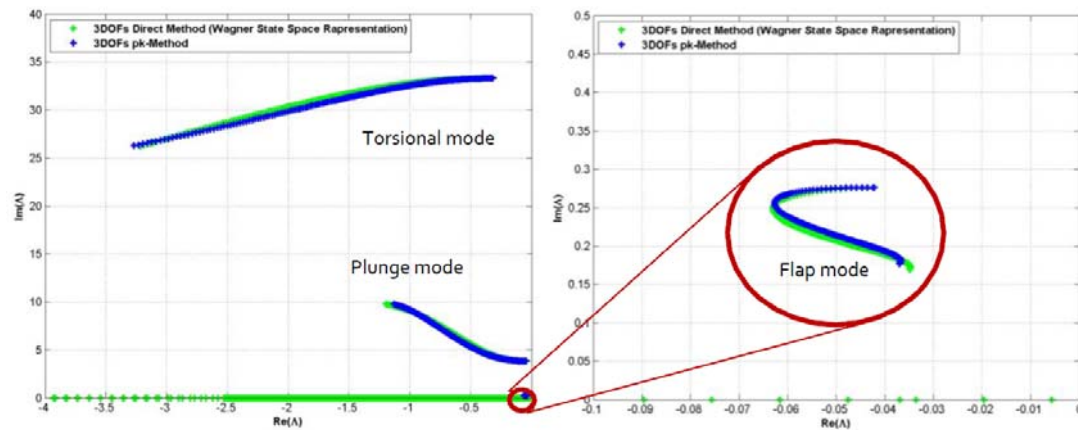


Figure 3: Eigenvalues analysis for procedure validation. Comparison between p - k method for frequency domain approach (blue markers) and direct method for time domain approach (green markers). Plunge and torsional modes are in the left figures, flap mode is zoomed in the right one. A variation of the section speed from 0 to 80 m/s (corresponding to a 120% of the rotor rated speed) is considered

In figure 3, the green markers represent the eigenvalues calculated with the direct methods with the time domain approach and the blue ones are the eigenvalues computed with the p - k method with the frequency domain approach. As one can see, there is a good agreement between the aeroelastic states (torsional, plunge and flap) identified by the two approaches. The real eigenvalues of the direct approach represent the unsteady aerodynamic states, that can be found only in the state space aerodynamic representation.

Flap optimization and final configuration

The output of the optimization procedure described in the previous section on the DEL is shown in the next figure.

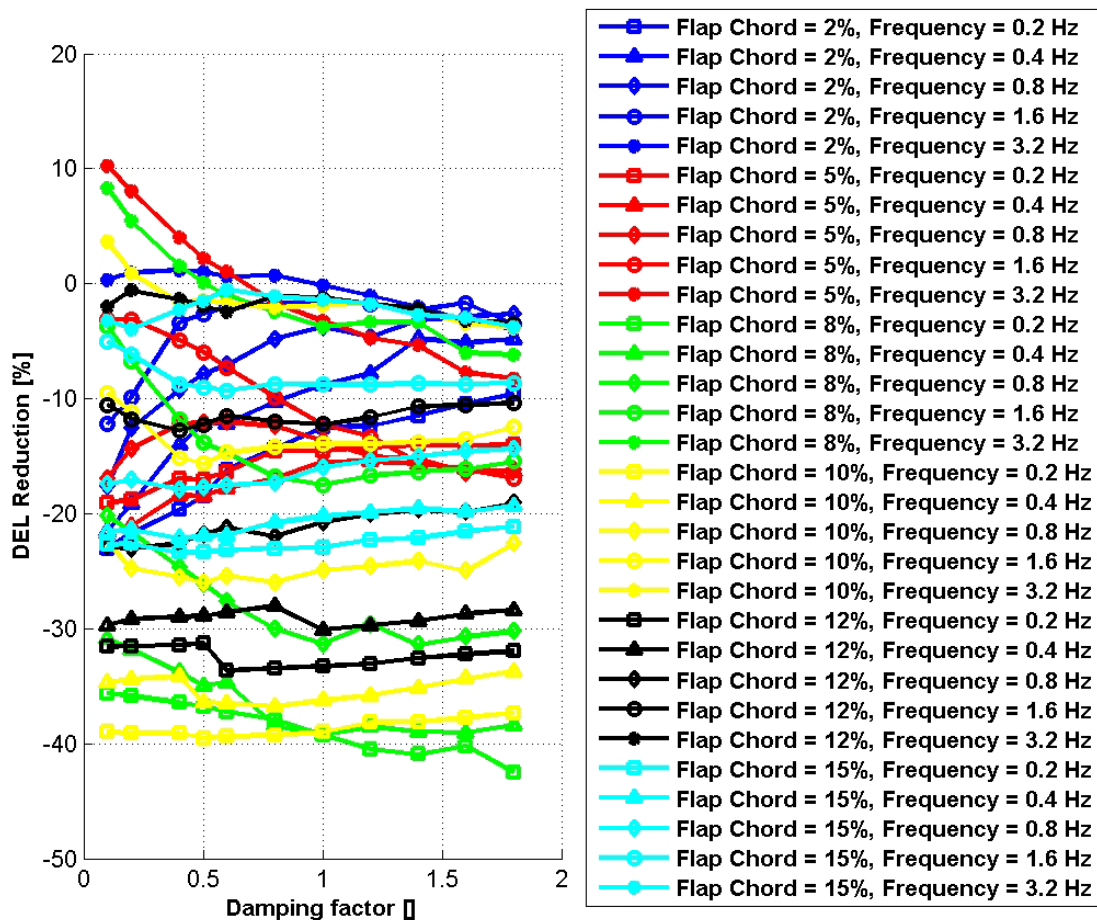


Figure 4: DEL reduction analysis, in percentage of system without flap. Several flap chords and flap frequencies have been considered

Figure 4 shows the DEL reduction for several damping coefficients, frequencies and flap chord values expressed in percentage of sectional chord. Going toward smaller values of flap chord, system is not effective for two reasons:

- 1) small flap chord means pour flap authority into the system model, that results in a low DEL Reduction (e. g. see curves 2%, 5% of flap chord, at 0.2,0.4,0.8 and 1.6 Hz of flap frequency);
- 2) Too limited flap deflection range at smaller flap chords for physical reasons (see Figure 6), that introduces truncation effects which result in an increase of DEL at higher frequencies and lower damping coefficients (e.g. see curves 2%, 5% of flap chord, at 3.2 of flap frequency and from 0.1 to 0.7 of damping factor).

Going toward higher values of flap chord, the passive system is more effective, especially at lower frequencies. Best values of DEL reduction are found to be with 10% of flap chord and a frequency of 0.2 Hz, with a flat behavior with respect to damping factor. A good trend of DEL reduction seems to be with 8% of flap chord and a frequency of 0.2 Hz, going toward higher damping coefficients (especially higher the 1), but this may results in a higher energy dissipation with problems related to heat dissipation.

At the end of this procedure the parameters obtained are reported in Table 1.

Parameter	Value
Blade chord [m] (75%)	3.25
Plunge frequency [Hz]	0.62
Torsional frequency [Hz]	4.95
Plunge damping factor []	0.01
Torsional damping factor []	0.01
Blade mass [Kg/m] (75%)	186
Blade moment of inertia [Kg*m] (75%)	94.1
EA position a [% Blade semichord]	29
Static moment x_α [% Blade semicord]	12.5
Flap chord c_f [m]	0.32
Flap frequency [Hz]	0.20
Flap damping factor []	0.50
Flap mass [Kg/m] (75%)	16
Flap static moment x_δ [% Blade semicord]	16
Flap moment of inertia [Kg*m] (75%)	2.02
Flap over-hang OH [% Flap chord]	32
Hinge position e [% of Blade semichord]	90

Table 1: Section model, final configuration

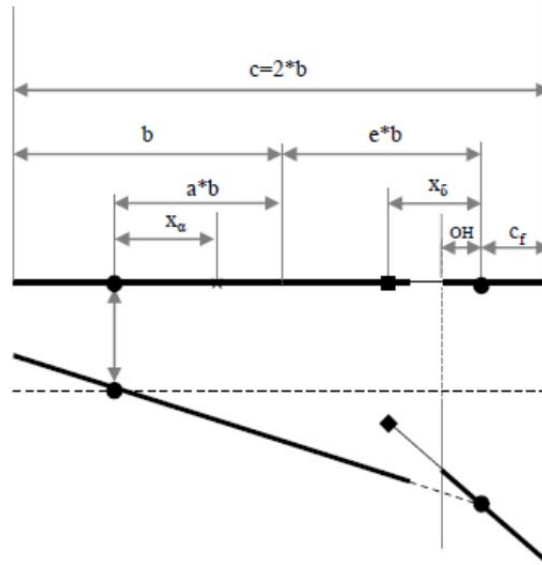


Figure 5: Section model, geometrical parameters definition

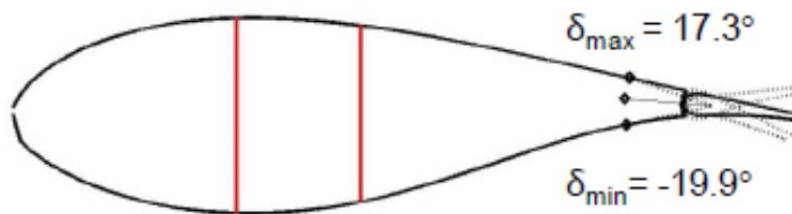


Figure 6. Section model, flap deflection range with physical constraint.

System Stability

In figure 7 the stability analysis for final optimized configuration has been performed, using only the state space model (i.e. the same used for the section response described in the following sections). In this analysis, the regulation trajectory of the wind turbine has been considered, so that for each wind speed the corresponding reference conditions have been taken into account, including the blade centrifugal stiffening due to rotor speed.

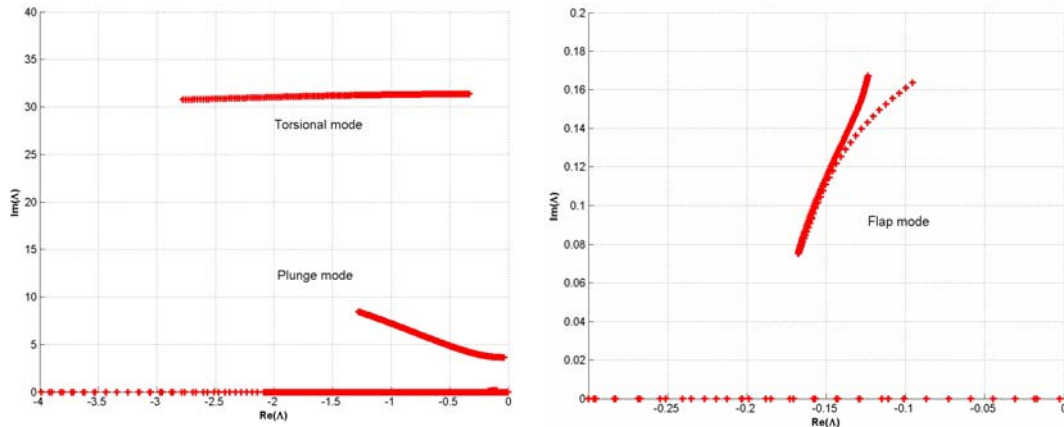


Figure 7: Eigenvalues for stability analysis, final configuration. Plunge and torsional modes are in the left figure, flap mode is zoomed in the right figure. Plunge stiffness variation with centrifugal force is included. A variation of the section speed from 0 to 80 m/s (corresponding to a 120% of the rotor rated speed) is considered

Figure 7 highlights that the system is always stable within the velocity range considered.

Transfer functions

The transfer functions of the state variables with respect to the model input (angle of attack and pitch angles) are computed by the Fourier's transformation of the state space system. Figures 8-13 show these transfer functions of the system for different wind speed from 5m/s to the cut-out wind speed (25m/s).

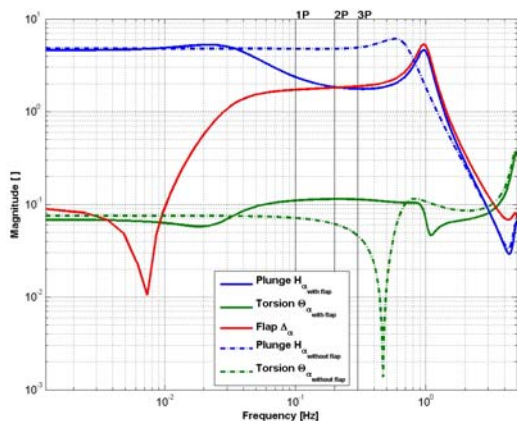


Figure 8: Transfer functions vs. angle of attack, at 5 m/s of wind speed

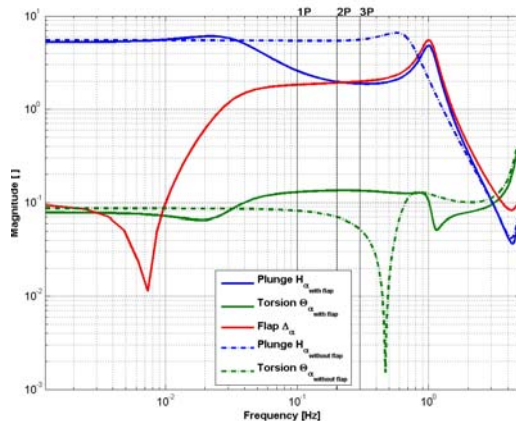


Figure 9: Transfer functions vs. angle of attack, at 7 m/s of wind speed

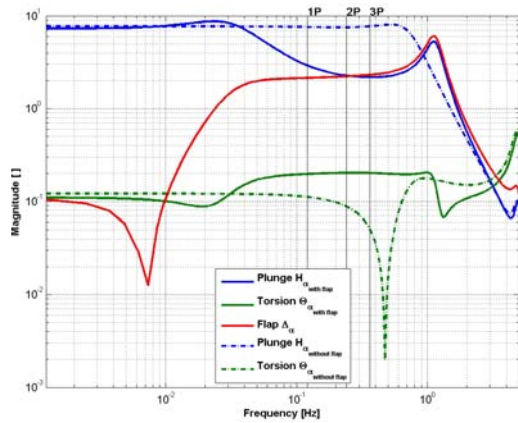


Figure 10: Transfer functions vs. angle of attack, at 9 m/s of wind speed

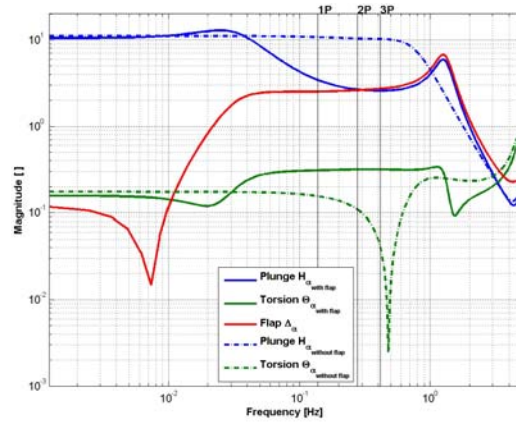


Figure 11: Transfer functions vs. angle of attack, at 11 m/s of wind speed

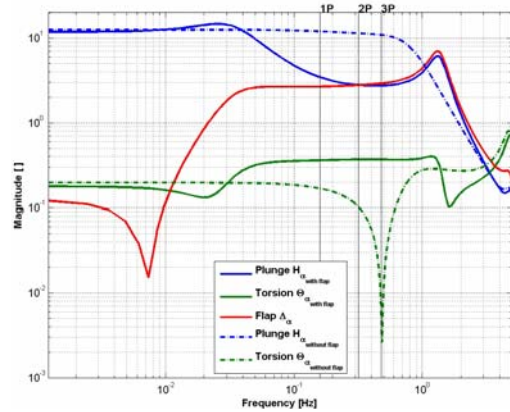


Figure 12: Transfer functions vs. angle of attack, at 19 m/s of wind speed

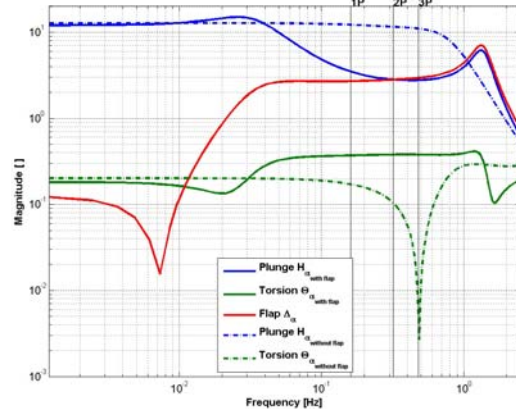


Figure 13: Transfer functions vs. angle of attack, at 25 m/s of wind speed

These figures show the transfer functions of the system with (solid line) and without (dot-dashed line) the passive flap. For the plunge motion (blue lines), a reduction of magnitude around the 1P-3P bandwidth is evident for all the velocities considered: the flap mode interact with the plunge mode in a way of splitting the first flap natural frequency of the blade (that is visible at 5 m/s case, figure 3) in two peaks, one before the 1P and one after the 3P. In this way, a notch filter around the 1P-3P bandwidth, where the main loads occur, is reproduced.

Another important point showed in the above figures regards the extracted power and the pitch control effectiveness. The use of a passive flap could reduce the aerodynamic power due to a reduction of the pitch control action. In this situation the flap could counteract to the active pitch control system. To avoid this situation, a flap balancing technique described in Ref. [6] is adopted. This balancing is highlight in figures 7-12, where, at lower frequencies the solid lines (i.e. the system with flap) and the dot-dashed ones (i.e. without flap) are very close and the flap deflection is poor. This means that the average loads as well as the power output are preserved.

Section response analysis

The simulations have been performed feeding the state space system with the angle of attack and the collective pitch angle time histories computed with Cp-Lambda, an aero-

servo-elastic multibody code (Ref. [11]). Design Load Cases (DLCs) DLC11 according to GL2010 (Ref. 12) from the cut-in wind speed (4m/s) to the cut-out (25m/s), normally used for the estimation of the fatigue loads, have been conducted and the output of these dynamic responses used as input of the state space system. These analyses are conducted for the section with and without the passive flap in order to evaluate the flap effect on the simplified model.

The following figures 14a-19a show the Fast Fourier Transform (FFT) of the plunge displacement with (red lines) and without (blue lines) flap for different mean wind speed. On the left, figures 14b-19b show the corresponding FFT input (i.e. the FFT of the angle of attack and of the collective pitch angle) and the FFT of the flap deflections. As one can see, the peaks in the 1P-3P region of the plunge displacement are reduced almost of one order of magnitude for all the mean wind speeds. The flap deflections depicted in the left (black lines) show that in all the conditions the angles are widely limited in the physical range showed in Figure 6 (+17 and -20 degrees).

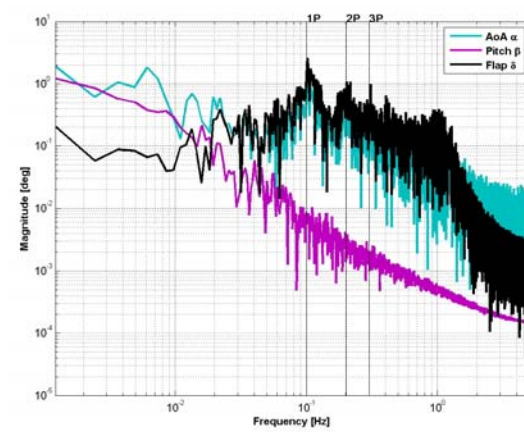
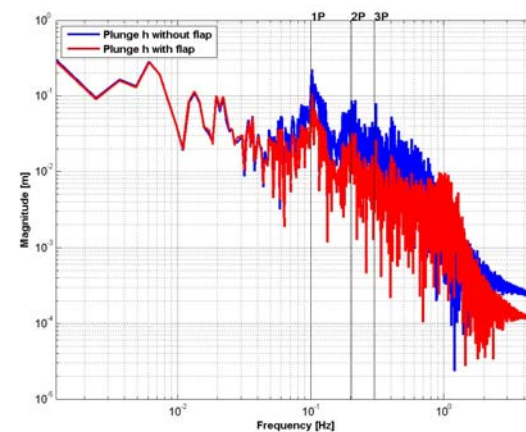
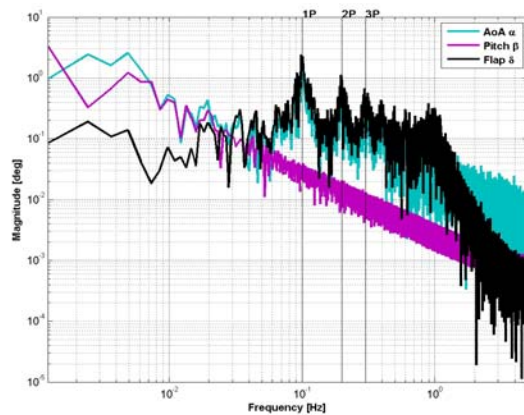
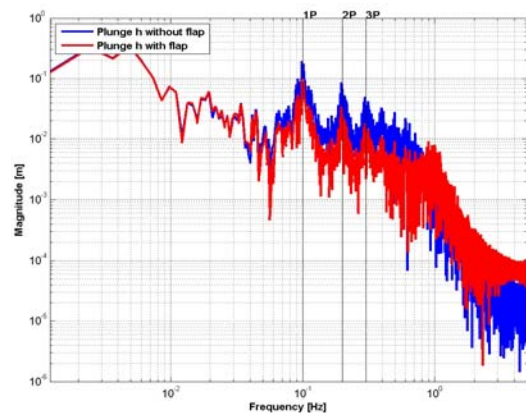


Figure 15a: plunge time response (FFT) with (red line) and without flap (blue line) at 7 m/s of wind speed

Figure 15b: Input time histories and flap time response (FFT) with and without flap, at 7 m/s of wind speed

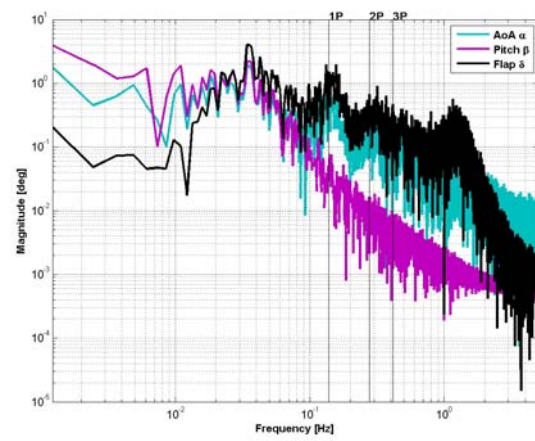
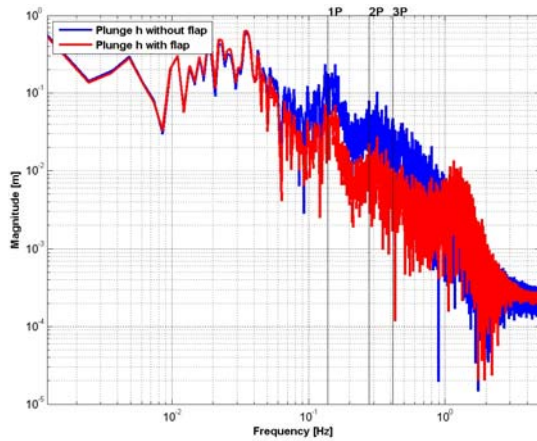
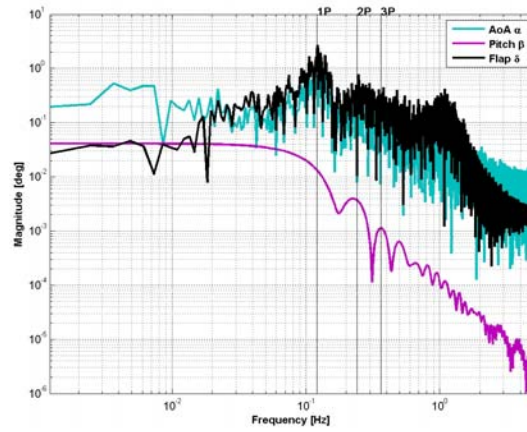
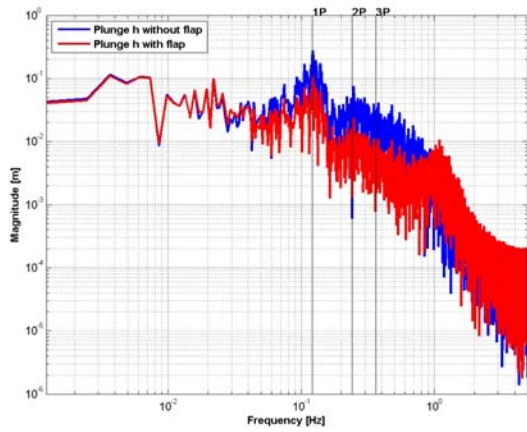


Figure 17a: plunge time response (FFT) with (red line) and without flap (blue line) at 11 m/s of wind speed

Figure 17b: Input time histories and flap time response (FFT) with and without flap, at 11 m/s of wind speed

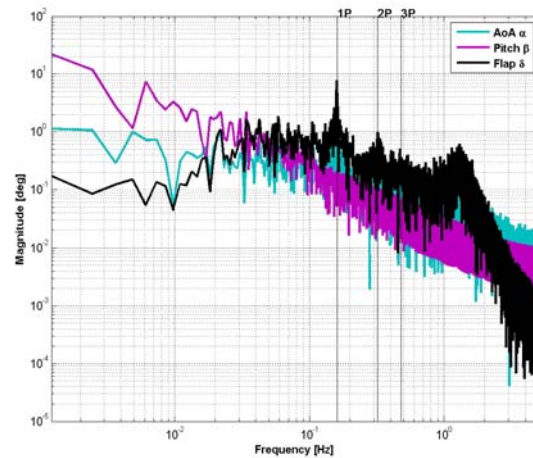
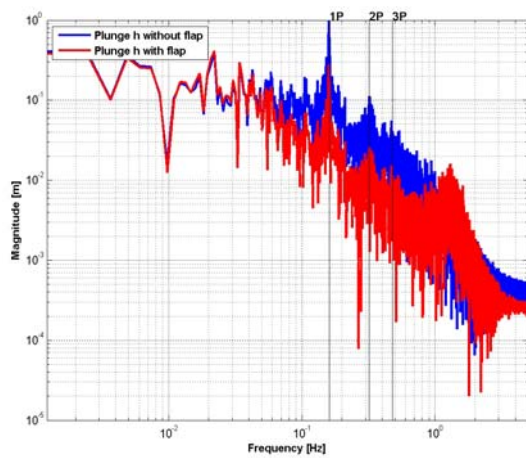


Figure 18a: plunge time response (FFT) with (red line) and without flap (blue line) at 19 m/s of wind speed

Figure 18b: Input time histories and flap time response (FFT) with and without flap, at 19 m/s of wind speed

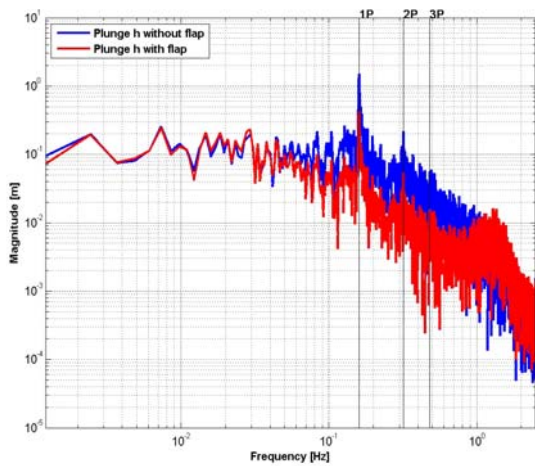


Figure 19a: plunge time response (FFT) with (red line) and without flap (blue line) at 25 m/s of wind speed

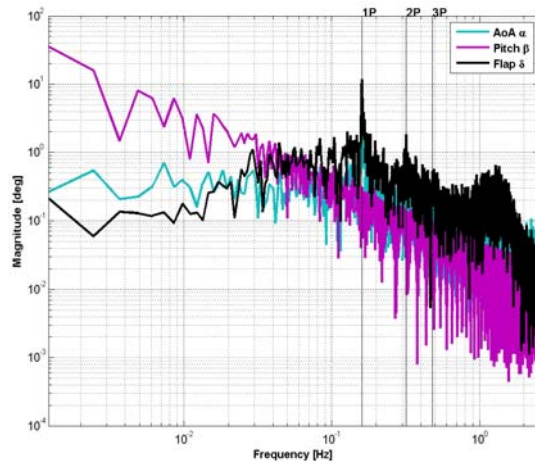


Figure 19b: input time histories and flap time response (FFT) with and without flap, at 25 m/s of wind speed

Time histories: AoA, Pitch and Flap deflections

Figures 20-25 report Angle of attack, Pitch and flap deflections, showing flap activity during wind turbulent conditions, with respect to physical boundaries.

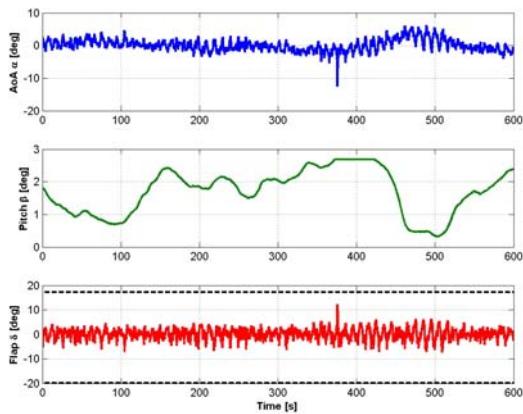


Figure 20: AoA, Pitch and flap deflection, at 5 m/s of wind speed

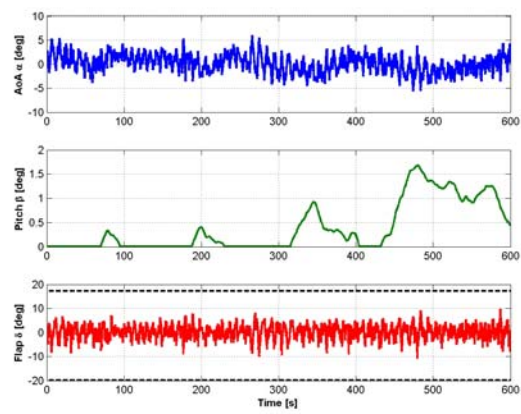


Figure 21: AoA, Pitch and flap deflection, at 7 m/s of wind speed

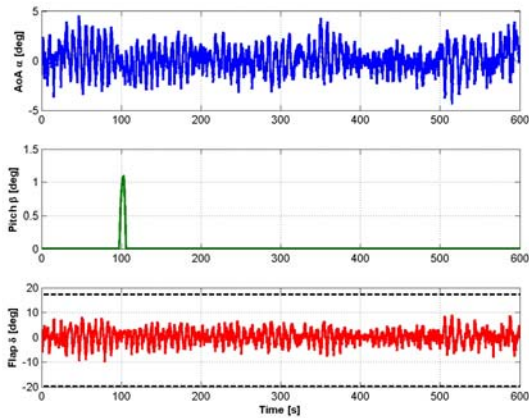


Figure 22: AoA, Pitch and flap deflection, at 9 m/s of wind speed

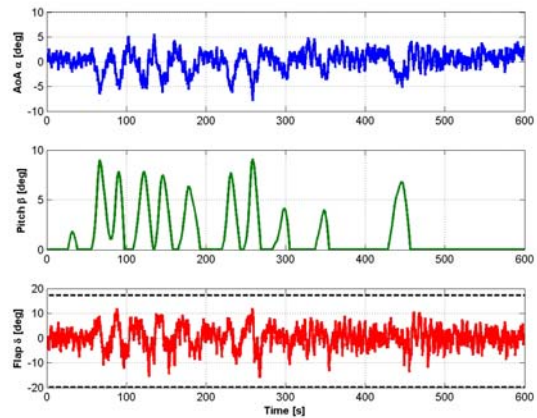


Figure 23: AoA, Pitch and flap deflection, at 11 m/s of wind speed

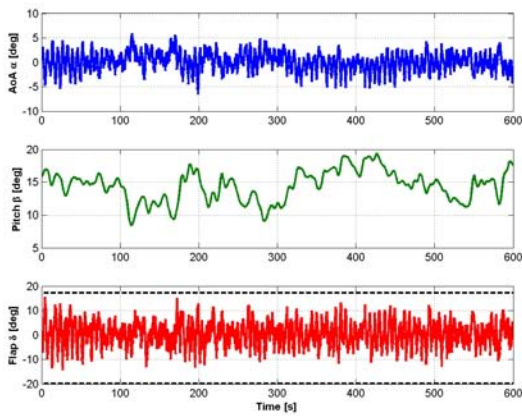


Figure 24: AoA, Pitch and flap deflection, at 19 m/s of wind speed

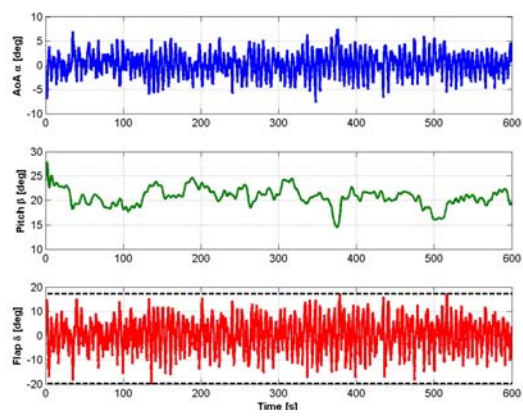


Figure 25: AoA, Pitch and flap deflection, at 25 m/s of wind speed

Damage equivalent load

Finally, from the previous analyses, the Damage Equivalent Loads (DELs) are computed for the system with the passive flap as well as without the flap, in order to estimate the effectiveness of the passive flap in the reduction of the fatigue damage. The equivalent load is defined as the cyclic load which, when applied n_{eq} times gives the same fatigue damage on the wind turbine as the real turbulent flow at the considered wind speed (Ref. [10]).

The results of DELs calculation are illustrated in the next figures. In particular, figure 26 shows for each mean wind speed the DELs computed without flap (blue bars) and with the passive flap (red bars). In the range between 5m/s and 9m/s the equivalent loads are mitigated considerably: at 9m/s DEL is reduced of about 50%. Figure 27 shows the same DELs weighted with the Weibull probability density function with $k=2$ (i.e. Rayleigh) and $V_{AVE}=10m/s$.

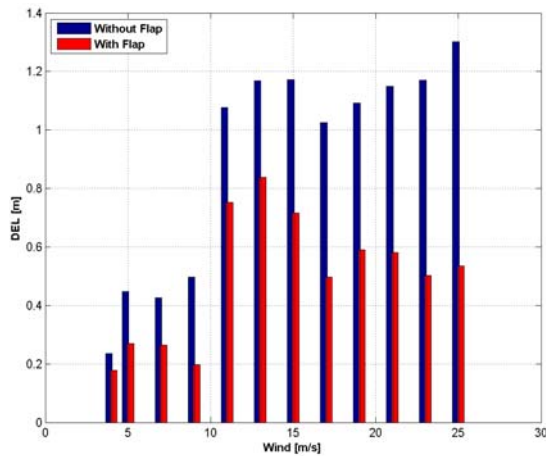


Figure 26: Damage equivalent load for plunge displacement at each wind speed. Comparison between system with (red bars) and without flap (blue bars).

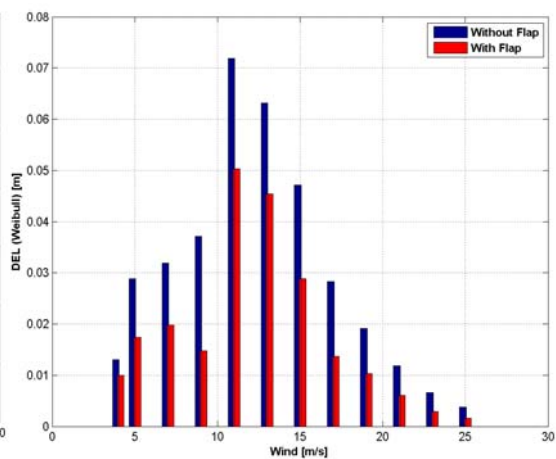


Figure 27: Damage equivalent load for plunge displacement at each wind speed, weighted with Weibull distribution with $V_{AVE}=10\text{m/s}$. Comparison between system with (red bars) and without flap (blue bars).

Effects on power production

The effects on power production are estimated by the non-linear wind turbine reduced model. Normal Turbulence Model (NTM) wind fields with different values of mean hub wind speed are considered. For each wind speed the dynamic analyses of the system are performed by time domain integration. When the installation of passive flap is taken into account, the pre-computed noises $T_{a,flap}$ and $F_{a,flap}$ are considered accordingly. The dynamic simulations explore all the power production range, allowing to assess the variation of AEP due to the noise induced by the passive flap.

In **Error! Reference source not found.**8 the mean value of the electrical power is reported towards mean hub wind speed. This estimation predicts a slight reduction of the power when the passive flaps are considered. The reduction of the power is reflected also into AEP evaluation as shown by **Error! Reference source not found.**, in which the AEP values, in turbulent condition with and without passive flaps, are reported. This analysis shows a limited per cent variation of AEP, but a further validation with a more complete model is worthiness.

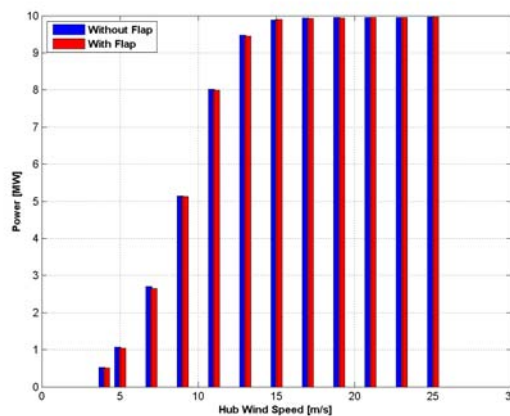


Figure 28: Power production vs hub wind speed: standard configuration vs passive flap configuration in turbulent wind conditions.

Table 2: Passive flap effects on AEP

Reference model	Model with passive flap	Variation
47.54 GWh/year	47.38 GWh/year	-0.33%

3.4 Conclusions

In this task, a passive flap system for load mitigation has been investigated. The advantage of this technique is that a passive flap does not require sensors and actuators and moves only passively in response to blade vibrations.

In this preliminary analysis a typical section of the INN WIND blade has been considered and two different models have been developed, one in the frequency domain using the classical Theodorsen's theory and the second in the time domain using the Wagner Indicial Response Model.

The latter has been used to run dynamic simulations in order to estimate the fatigue damage in turbulent condition with and without this balanced passive flap. This comparison has highlighted the effectiveness of this passive system in the reduction of the DELs.

Finally, the effect of passive flap on AEP has been estimated by the non-linear wind turbine reduced model. Normal Turbulence Model (NTM) wind fields with different values of mean hub wind speed are considered. Values reported in Table 2, show a loss of Annual energy production of less the 0.4%. Further investigation of the impact on the CoE should be made in order to point out whether or not the passive flap would be a successful technology.

Next step will be the integration of this technology in a more sophisticated environment such as aeroelastic simulations in order to include this passive flap in the more general context of wind turbine design.

3.5 References

- [1] Bisplinghoff, R. L., Ashley, H., 1962. *Principles of Aeroelasticity*. John Wiley & Sons, Inc., Hoboken, New Jersey.
- [2] Karpel, M., 1981. *Design for Active and Passive Flutter Suppression and Gust Alleviation*. Cont. Rep. 3482, NASA.
- [3] Leishman, J. G., 2006. *Principles of Helicopter Aerodynamics, 2nd Edition*. Cambridge University Press, Cambridge, England.
- [4] Leishman, J. G., Nguyen, K. Q., 1990. *A state-space representation of unsteady aerodynamic behavior*. AIAA Journal 28 (5), 836–845.
- [5] Theodorsen, T., 1935. *General theory of aerodynamic instability and the mechanism of flutter*. Tech. Rep. 496, NACA.

- [6] Theodorsen, T., 1942. *Nonstationary Flow About a Wing-Aileron-Tab Combination Including Aerodynamic Balance*. Tech. Rep. 736, NACA.
- [7] Brunton L. , Rowley W., 2013. *Empirical state-space representations for Theodorsen's lift model*. Journal of Fluids and Structures 38 (2013) 174–186.
- [8] Kanda A., Dowell H., 2005. *Worst-Case Gust-Response Analysis for Typical Airfoil Section with Control Surface*. Journal of Aircraft Vol. 42, No. 4, July–August 2005.
- [9] Lambie B., M. Jain, C. Tropea. *Passive Camber Change for Windturbine Load Alleviation*. AIAA Aerospace Sciences Meeting including the New Horizons Forum and Aerospace Exposition 4 - 7 January 2011, Orlando, Florida.
- [10] M. O. L Hansen. *Aerodynamics of Wind Turbines, 2nd Edition*. Published by Earthscan in the UK and USA in 2008.
- [11] C.L. Bottasso, A. Croce, *Cp-Lambda User's Manual*, Dipartimento di Scienze e Tecnologie Aerospaziali, Politecnico di Milano, 2014.
- [12] Anonymous, *Guideline for the Certification of Wind Turbines*, Germanischer Lloyd Industrial Service GmbH, Hamburg, 2010
- [13] P. Donely, C.C. Shufflebarger, *Test of a Gust-Alleviating Flap in the Gust Tunnel*, NACA Report 745, January 1940
- [14] R.L. Bielawa, *Analytic Investigation of Helicopter Rotor Blade Appended Aeroelastic Devices*, NACA Report 166525, NASA Ames Research Center, 1984
- [15] R. H. Stroub, *An Analytical Investigation of the Free-Tip Rotor for Helicopters*, NASA Technical Memorandum 81345, February 1982
- [16] Larry A. Young, *The Evaluation of a Number of Prototypes for the Free-Tip Rotor Constant-Moment Controller*, NASA Technical Memorandum 86664, February 1986
- [17] A.F. Arrieta, O. Bilgen, M. I. Friswell, P. Hagedorn, *Passive Load Alleviation Bi-Stable Morphing Concept*, AIP Advances, 2, DOI: 10.1063/1.4739412, (2012)
- [18] A.F. Arrieta, I. K. Kuder, M. Rist, T. Waeber, P. Ermanni, *Passive Load Alleviation Aerofoil Concept with Variable Stiffness Multi-Stable Composites*, Composite Structures, 116, pp. 235-242, DOI: 10.1016/j.compstruct.2014.05.016 , 2014
- [19] C.L. Bottasso, A. Croce, Y. Nam, C.E.D. Riboldi, *Power Curve Tracking in the Presence of a Tip Speed Constraint*, Renewable Energy, 40, pp. 1-12, DOI: 10.1016/j.renene.2011.07.045, 2012

4 CONCEPT 3: GEOMETRIC AND MATERIAL COUPLING CONCEPTS

4.1 Introduction

Passive control techniques able to trigger load reduction on wind turbines have been the object of academic research for several years. These methods are based on the concept of designing a structure that, when loaded, deforms so as to induce load alleviation. The main idea is to create a coupling between flapwise bending toward the tower and torsion towards feathering. This coupling has the capability to mitigate loads on the structure due to a decrease in the angle of attack. There are two different approaches to implement passive control strategies on a wind turbine blade: varying the geometry (swept blades) or material properties (fibres) of the blade.

Several studies dealing with either of these methods can be found in literature. Concerning the geometrical coupling and only mentioning investigations previously conducted by DTU, Verelst and Larsen [1] implemented a parametric study based on several swept blade configurations involving variations on both sweep curvature and sweep offset at the tip. The simulations were run using the DTU Wind Energy aeroelastic code HAWC2 [2] and the authors showed that flapwise fatigue and extreme loads can be reduced up to 10 and 15% respectively for a backward swept blade, whereas the edgewise fatigue and extreme loads can increase up to 6%. Hansen [3] investigated the aeroelastic properties of backward swept blades using the linear aero-servo-elastic model for open- and closed-loop eigenvalue and frequency-domain analysis HAWCStab2. He computed frequencies, damping and mode shapes of the aeroelastic blade modes of the NREL 5 MW [4] reference turbine. He concluded that the backward sweep creates torsion towards feathering for downwind flapwise deflection in the first flapwise bending mode. This torsional component is shown to cause the frequency of the first aeroelastic bending mode to increase compared to the corresponding structural frequency, and this increase is larger for larger sweep. Furthermore, Hansen found that the frequency response of the flapwise blade root moment from wind excitation decreases below the increased first flapwise frequency, which explains the reduced flapwise loads observed in other studies of backward swept blades.

Regarding material bend-twist coupling, at DTU an 8m section from a 23m blade from Vestas Wind Systems A/S underwent both dynamic and static tests. The original blade section was tested and then modified with four layers of UD1200 (unidirectional glass fibre, 1200 g/m²), which were laminated on the pressure and suction side of the blade with an angle of 25 degrees to the blade axis to create a measurable flapwise bend-twist coupling. The results and comparison with numerical analyses showed that a valid coupling can be easily introduced and measured by adding angled unidirectional layers on the blade section [5] [6].

Important contributions to the topic were also given by previous European projects such as the Upwind, funded under the EU's Sixth Framework Programme (FP6) that ran from 2006 to 2011 [7]. Under "Work Package 2 – Task 1 Structural Dynamics – Large Deflections and non-linear effects" [8], simulations and investigations with uniform inflow were done to estimate the significance and the effect of geometrical variations on the

blade properties on loads and stability. The analyses focused mostly on pre-bent rather than swept blades. Concerning swept blades the study concluded that fore sweep degrades stability of the blade and that an optimum sweep for the Reference Wind Turbine blade with respect to loading and stability can be found.

In light of these previous studies, it is clear that the academic research has already emphasized the potential of passive control methods. The effects generated on the wind turbine machine by the implementation of these methods on the blade structure have been extensively studied. Experimental campaigns on material coupling run by DTU and the commercialization of blades with geometrical coupling by company such as Siemens showed that, for passive control, the step from concept to technology is feasible. Although technologies based on passive control have already proven their strength, their use is still limited and their implementation is not systematic and widely embraced by the industry. The study reported on this chapter serves as an initial step to build a guideline for the practical implementation of passive control methods on real machines, with the purpose of making passive control concepts easier to turn in useful technologies and state-of art for the latest wind turbine designs.

The first paragraph is dedicated to the description of the concept. A depiction of the model used to perform the actual study is reported in the second paragraph. Results follow concluding with a section dedicated to final remarks and outlook.

4.2 Description of the concept

Today, beneficial and disadvantageous effects related to the implementation of geometrical or material bend-twist coupling are well-known, but no effort has been made yet to try to control these effects. The question is: if one can establish that the blade needs to deform in a certain fashion to mitigate particular loads rather than others, is it possible to create a structural input that forces the blade to follow the prescribed behaviour?

The idea of establishing an initial guideline to control the implementation of passive methods is the focus of the concept described in this paragraph. Following the path described by the studies conducted by DTU, the actual investigation aims to take a further act in the implementation of passive control methodologies on wind turbine blades, studying the possibility of regulating the blade deformations through passive control strategies according to need. So far, academia and industry have analysed the concept of passive control and its effects and brought it to technology without trying to discipline its implementation. Knowledge on how to regulate these control strategies is hence needed to define a stronger bridge between concept and technology, so that in the near future the use of passive control methods on wind turbines can be systematic and widely adopted.

The concept proposed involves the application of both geometrical and material bend-twist coupling, with the final purpose of varying the wind turbine blade properties in order to match a prescribed structural behaviour connected to defined load alleviations.

The analysis is articulated as follows:

- Three different swept geometries for the DTU 10 MW RWT blade are selected based on the fact that previous studies (Verelst and Larsen [1] and Hansen [3]) showed that these configurations are the best compromise between beneficial and disadvantageous effects (further details are reported in the next paragraph)
- A simple load case is applied to each of the swept blades using the nonlinear aeroelastic model HAWC2 [2]
- The angle of attack is computed along the blade length at several points
- Using an optimization framework (described below), structural input files are created in order to force straight blades to have the same angle of attack distribution under the simple load case selected
- Natural frequencies of the three configurations with geometrical bend-twist coupling and the three straight blades with material coupling are compared and discussed
- Full nonlinear aero-servo-elastic simulations are run with the six different models generated and results are compared with the baseline
- Considerations on the use of geometric and material coupling are made and eventual differences, positive and negative effects are discussed
- Benefits and drawbacks of building an “ad hoc” passively controlled blade through modifications of the stiffness matrix terms are considered

The study represents the first step in the regulation of passive control. Blade configurations that generate desirable effects on the wind turbine loads are selected and their behaviour is replicated on structures passively controlled through material bend-twist coupling. The investigation shows that these types of control can be used to force the machine to follow a prescribed behaviour. In the future, passive control methods are not going to be implemented blindly checking “a posteriori” if a favourable outcome is achieved, but they are going to follow guidelines which define clearly what a particular passive strategy can generate for certain designs and conditions.

4.3 Model Description

Software and Baseline Model

In this investigation, the in-house nonlinear aeroelastic model for response in time domain HAWC2 is used. Basic information about the software is provided in the user’s manual [2] and its validation can be found in Vorpal et al. [10], Popko et al. [11] and in Larsen et al. [12]. The structural model of the software is based on a multi-body formulation assembled using Timoshenko beam elements developed by Kim et al. [13]. The aerodynamic model, based on a BEM method, handles dynamic inflow, dynamic stall, skew inflow, shear effects on the induction and effects from large deformation.

The INNWIND version of the DTU 10 MW Reference Wind Turbine [9] is used as a baseline for the current study. The optimization framework was developed using MatLab®.

Swept Blades Geometry

As previously introduced, three different swept geometries are considered. Since previous analyses agree that fore sweep degrades the stability of the structure causing in all cases increased fatigue and extreme loads [1] [7], only backward sweeps are taken into account. All the properties of the wind turbines related to aerodynamic characteristics of the blade are kept the same for all the configurations analysed.

The sweep geometries are described by a shape function similar to the ones used by Verelst [1] and Hansen [3]:

$$s = \left\{ a \frac{z}{R_0} - b \left(\frac{z}{R_0} \right)^c, 0, z \right\}^T \quad z \in [0; R_0]$$

Where s is the elastic axis as function of the blade length, z is the coordinate along the pitch axis of the blade, $R_0 = 89.166 \text{ m}$ is the blade length in hub-coordinate system, a is a linear term for forward sweep added to compensate an otherwise large steady torque moment and b is the term for the backward sweep, which curve exponent is determined by c . The elastic axes of the blade along the span for three different swept configurations are plotted in Figure 1, whereas the parameters for the different configurations are:

- Swept Blade Level 1 : $a = 5, b = 10, c = 2$
- Swept Blade Level 2 : $a = 10, b = 20, c = 2$
- Swept Blade Level 3 : $a = 10, b = 20, c = 3$

According to Verelst and Larsen [1], a quadratic or a cubic exponent is the best compromise between reduced extreme and fatigue flapwise loading and increased extreme and fatigue edgewise loading on the blade root. Backward sweep results in reduced loadings on shaft and tower as well, touching the maximum alleviation for $c = 3$. In general, the larger the sweep the greater is the decrease or increase in extreme and fatigue loads, but to avoid negative effects on the blade root torsion a maximum value of 20 for b is considered a good compromise. Nonetheless a smaller value of the term for the backward sweep coefficient b has also been taken into account.

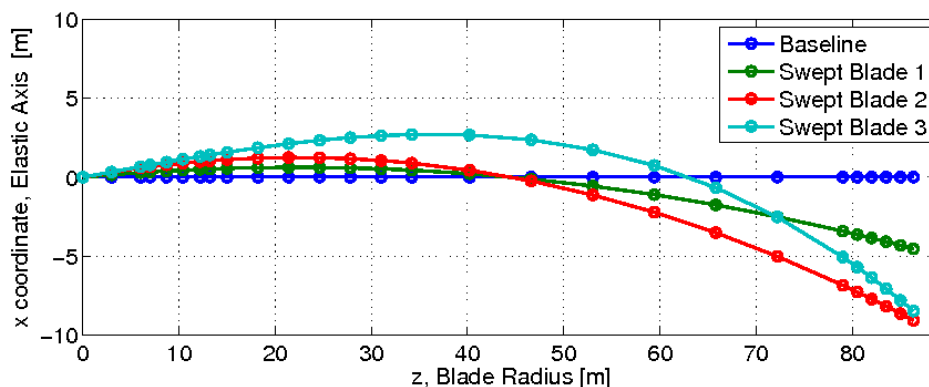
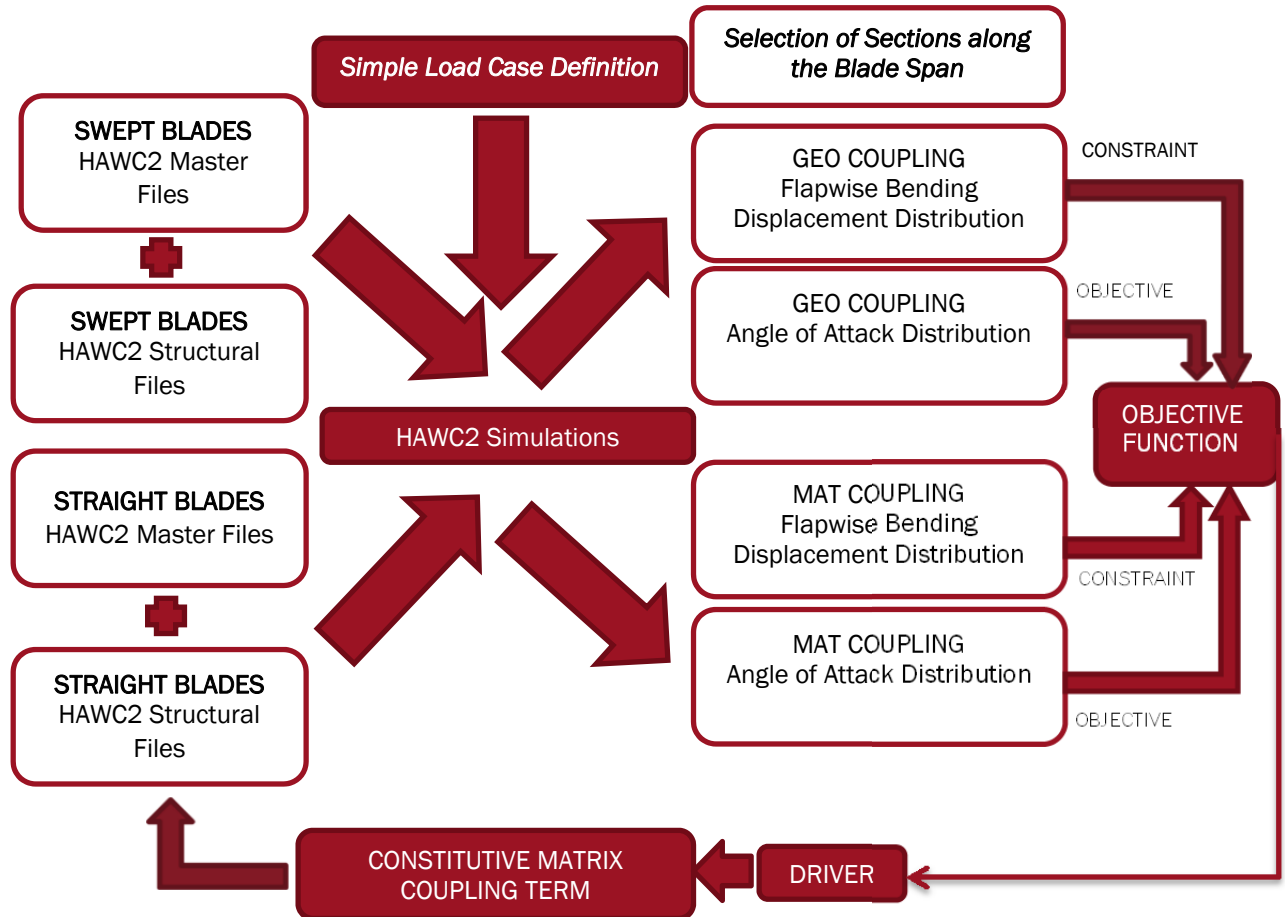


Figure 1 - Elastic axis x-coordinate for the baseline and the backward swept blades

Optimization Framework – Concept



The objective is to compare geometrical coupling with material coupling. To achieve this purpose, a brief analysis of the angle of attack along the span of the three swept blades under a simple load case is carried. The distributions of the angle of attack for the three swept configurations are registered and structural input files for three straight blades are generated. These non-swept blades are characterized by the presence of an extra term in the blade elements constitutive matrices. This extra term couples flapwise bending towards the tower with torsion towards feather, and a proper amount of coupling is selected in order to have three straight blades with material coupling that are behaving like the three swept blades under a defined load case. To perform properly the material coupling selection for each blade, an optimization scheme is used. The block diagram above shows the work flow used to generate the structural input files for the straight blades.

Before reporting the results and the conclusions on the current analysis, it is important to remark the reason why the angle of attack has been chosen has the base for the optimization framework.

In general, the angle of attack is strictly linked to the aerodynamic forces acting on the blade. Hence, it is the main factor that influences the variation of the loading on the full wind turbine structure. The analysis of the variation of the angle of attack along the blade span is therefore fundamental to understand the capability of passive controlled blades to alleviate loads.

Optimization Framework - Description

The architecture of the code is described as follows:

- Tors_Opt.m: main file, selection of the study case (swept blade parameters), initial condition for the optimization algorithm and boundaries for the optimization variable
- Parameters.m: Selection of Parameters for the HAWC2 simulations, including input-output files, calculation points for the angle of attack and boundaries for the constraints
- TorsComp.m: function driver for the workflow
 1. WRITES an .st structural input files for HAWC2
 2. RUNS the simple load case simulation in HAWC2
 3. READS results file
 4. CHECKS that the flapwise bending displacement distributions are consistent
 5. GENERATES an objective function based on the difference between the computed angles of attack along the blade, using the MatLab® built-in function patternsearch [14]
 6. patternsearch SELECTS the best coupling term α from

$$K_{46}(s) = \alpha \sqrt{EI_f(s)GJ(s)} \quad [13]$$

Where s indicates the radial position of the section along the curved length of the elastic axis of the blade, EI_f is the flapwise bending stiffness and GJ is the torsional stiffness of a section of the blade

7. The cycle starts again with a new structural file that includes the new computed terms $K_{46}(s)$, and the workflow continues until convergence is reached
- Plot_Routine_AA.m: function that plots the results obtained.

4.4 Results

Load Cases Description

The first step is to define a simple load case that can be used to run the optimization framework. As previously described, the idea is to compute the distribution of the angle of attack along a swept blade, and compare it to the one computed for a bend-twist coupled straight blade. The optimization scheme has the task of finding a coupling term for the structural input file in order to be able to match the two angle of attack distributions computed at a certain number of calculation points along the blade span.

In order to maintain the optimization problem as simple as possible, the load case chosen does not include turbulence and other effects that would add unnecessary complexity to the workflow carried by the framework. Simplicity for the load case is also a requirement to keep the computational time of each HAWC2 simulation within a reasonable limit. The optimization scheme performs several HAWC2 simulations before reaching convergence: the faster the HAWC2 simulation, the faster a local minimum is reached. The optimization scheme is based.

Table 1 contains the brief summary regarding the simple load case on which the optimization scheme is based.

Table 1 - Simple Load Case for optimization framework

1st LOAD CASE – Simple Load Case for Optimization Scheme	
SIMULATION TIME	500 [s]
MEAN WIND SPEED	7 [m s ⁻¹]
WIND FIELD ROTATION	No
WIND SHEAR	No
TOWER SHADOW	No
TURBULENCE	No
WAKE EFFECT	No
TIP-LOSS FACTOR	Yes
DYNAMIC STALL	Yes

Once the optimized straight blade configurations are obtained, the different wind turbine models are subjected to two more load cases. In order to compare the power outputs of the different configurations for deterministic wind speeds, a load case where the wind speed varies in steps of 2 m/s from 4m/s to 20 m/s is implemented. General information about the load case is reported in Table 2.

Table 2 - Load Case, Deterministic Wind Speeds

2nd LOAD CASE - Power Output Computation at different Wind Speeds	
SIMULATION TIME	1000 [s]
MEAN WIND SPEED	4-20 [m s ⁻¹] with steps of 2 [m s ⁻¹]
WIND FIELD ROTATION	No
WIND SHEAR	No
TOWER SHADOW	No
TURBULENCE	No
WAKE EFFECT	Yes
TIP-LOSS FACTOR	Yes
DYNAMIC STALL	Yes

The last load case consists of 10 minute series with turbulent wind speed from 4 m/s to 26 m/s, tower shadow and no wind shear (Table 3). This load case is used to computed extreme and fatigue loads acting on the wind turbines.

Table 3 - Load Case with Turbulent wind speeds

3rd LOAD CASE - Extreme and Fatigue Loads Computation	
SIMULATION TIME	600 [s]
MEAN WIND SPEED	4-26 [m s ⁻¹]
WIND FIELD ROTATION	No
WIND SHEAR	No
TOWER SHADOW	Yes
TURBULENCE	Yes
WAKE EFFECT	Yes
TIP-LOSS FACTOR	Yes
DYNAMIC STALL	Yes

Geometric to Material Coupling Optimization Results – 1st Load Case

Results obtained from the optimization routine implemented are showed and discussed. Figure 2, 3 and 4 show the distributions of the angle of attack along the blade lengths for each of the cases analysed. For each couple of distributions, the relative error is plotted.

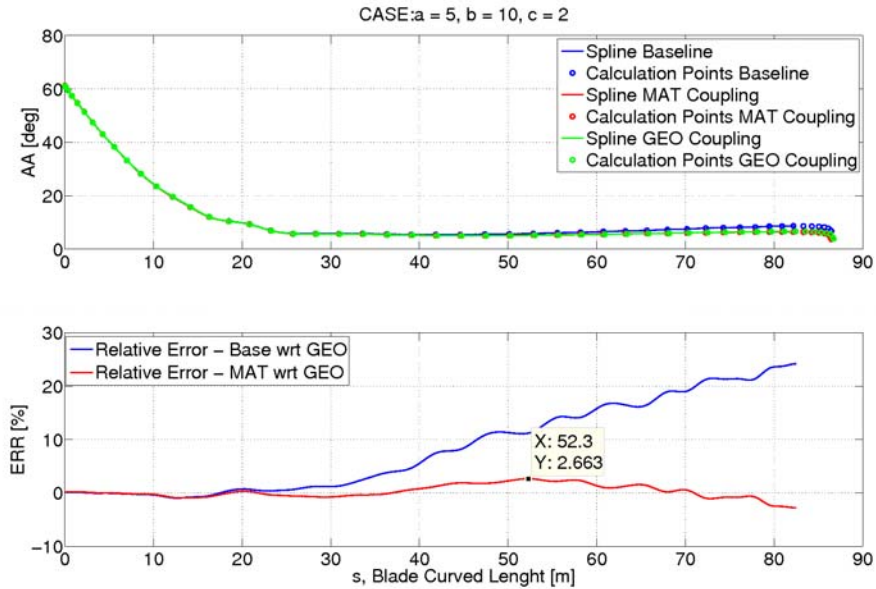


Figure 2 - Optimized Angle of Attack distribution (above) and variation with respect to the baseline and the optimized material coupled configuration - Case a = 5, b = 10, c = 2

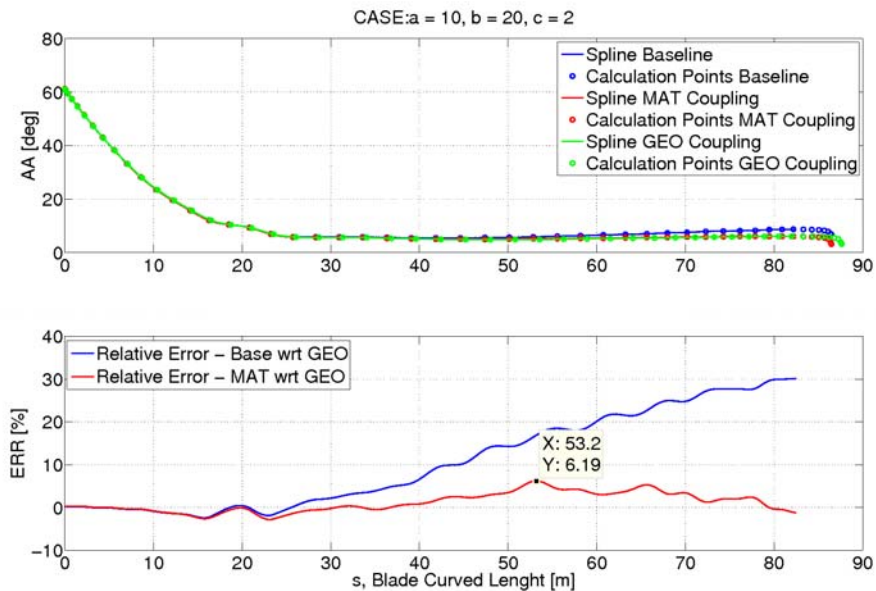


Figure 3 - Optimized Angle of Attack distribution (above) and variation with respect to the baseline and the optimized material coupled configuration - Case a = 10, b = 20, c = 2

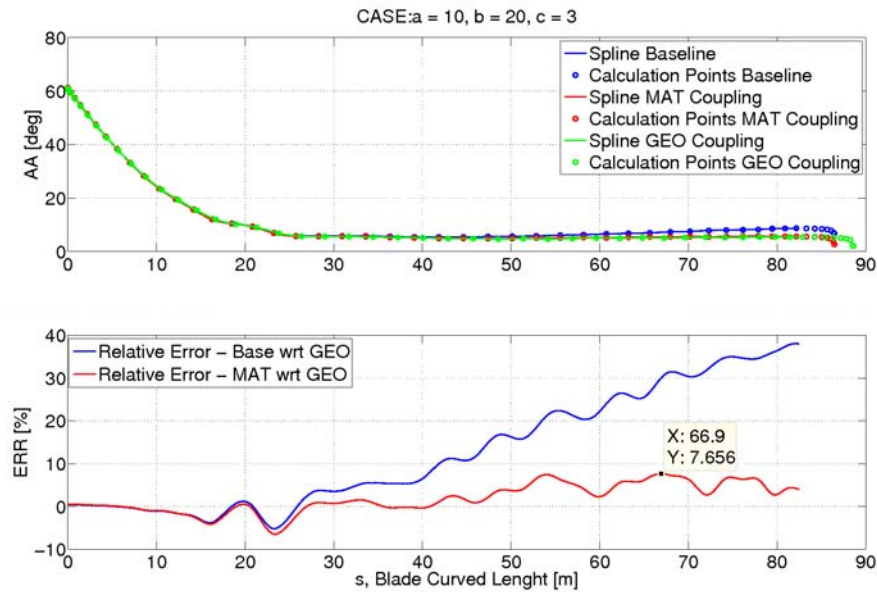


Figure 4 - Optimized Angle of Attack distribution (above) and variation with respect to the baseline and the optimized material coupled configuration - Case a = 10, b = 20, c = 3

The optimization scheme delivers satisfactory results. For the first case (Figure), a local minimum is found for a coupling term $\alpha = -0.1316$. The plot shows that the maximum relative error between the optimized distribution and the targeted swept blade angle of attacks is below 3%. When the bend-twist coupling effect increases for the “more extreme” configurations, the maximum relative error between the analyzed distributions increases:

- Second case (Figure 3), $\alpha = -0.1685$ with a maximum error around 6%
- Third case (Figure 4), $\alpha = -0.2050$ with a maximum error below 8%

The coupling term α is the same for all the sections along the blade span. Better results can be achieved if the optimization scheme could deliver an optimized coupling term for each of the sections. For the time being a single α , even though unrealistic, is considered sufficient to carry on the analysis.

Another way to compensate this difference would be to re-compute the static twist distribution along the blade span. Active pitch control can also be used to obtain a perfect match between the angle of attack evaluated at a certain wind speed. These methods and their effects are going to be exploited in future analysis.

The modification of the sectional constitutive matrices of the blade beam elements through the addition of the coupling term generates an impact on the overall stiffness of the material coupled straight blades. This effect is difficult to control, and the structural behaviour of the different configurations has to be monitored. Moreover, differences in stiffness are expected also for the swept blades, since the geometric coupled configurations are longer compared to their bend-twist coupled equivalent straight configurations. In fact, when the blade sections are geometrically shifted to create a swept blade, the sectional mass per unit length is not changed. Hence, the blade becomes longer and the mass slightly increases causing an impact on the overall blade

stiffness. Even though the angle of attack distributions of the different couples of blades are matching despite small deviations, substantial difference in the structural response of the different configurations is expected. An example is shown in Figure 5-7 where the flapwise bending displacement distributions along the curved length of the blades subject to the simple load case are plotted.

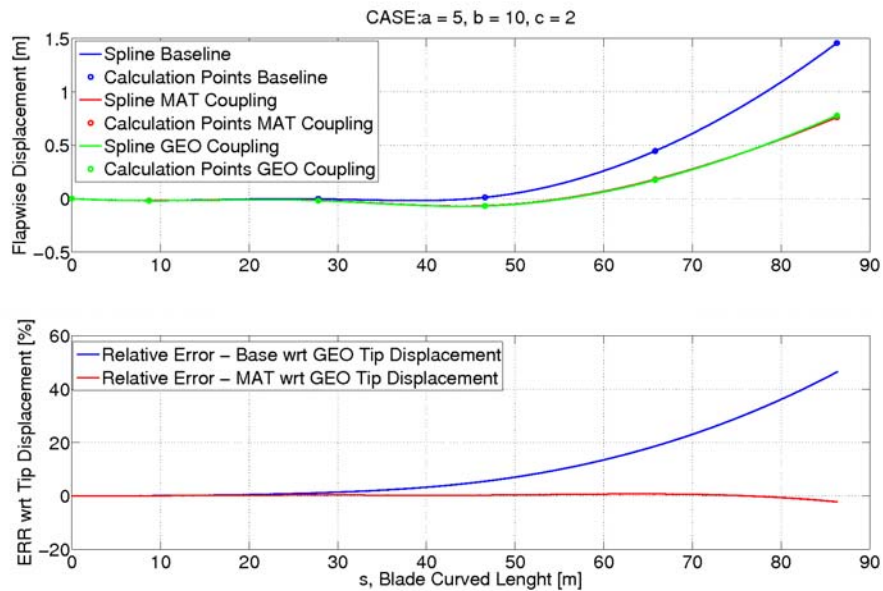


Figure 5 - Flapwise bending displacement distribution (above) and variation with respect to the baseline and the optimized material coupled configuration - Case a = 5, b = 10, c = 2

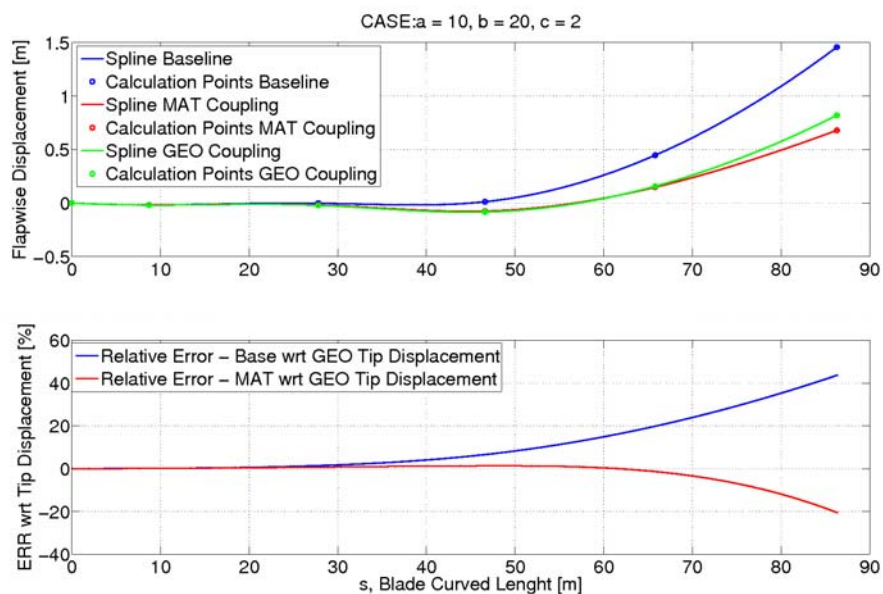


Figure 6 - Flapwise bending displacement distribution (above) and variation with respect to the baseline and the optimized material coupled configuration - Case a = 10, b = 20, c = 2

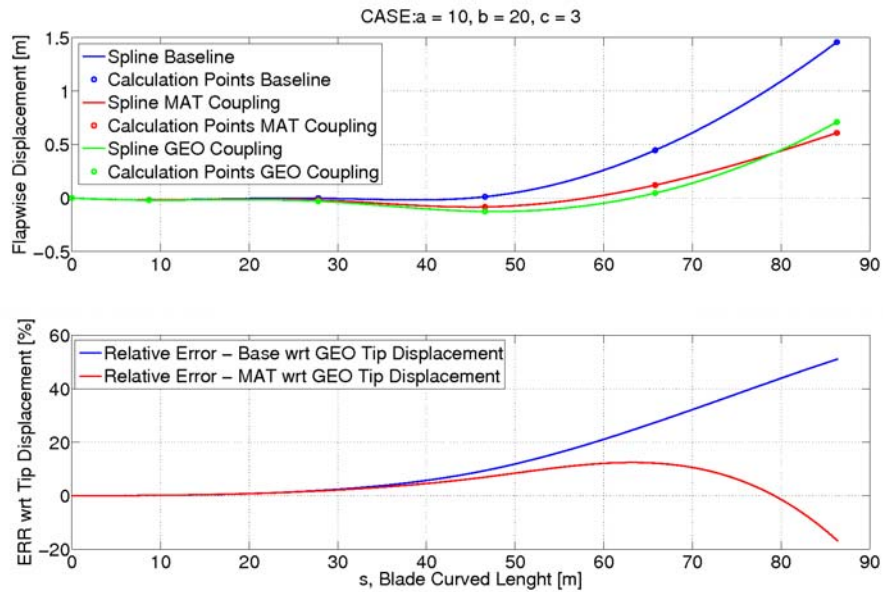


Figure 7 - Flapwise bending displacement distribution (above) and variation with respect to the baseline and the optimized material coupled configuration - Case a = 10, b = 20, c = 3

Except for the first case study with a mild material and geometric coupling (maximum error around 2%), the flapwise bending displacement distributions register a deviation of 20% with respect to the blade tip displacement. This difference between the geometric coupled blades and the material coupled blade is excessive and will produce substantial effects on the dynamic behavior of the turbines, with impacts on the extreme and fatigue loads computed. Future optimization analyses need to include more stringent restrictions on the structural behavior of the machine when large bend-twist coupling effects are considered.

Natural Frequencies Comparison

In the following paragraph, natural frequencies of the isolated blades and the full wind turbine structures are reported and discussed. Table 4 shows a comparison between the natural frequencies of the different blades configurations used for the current study.

Table 4 - Natural Frequencies comparison, isolated blades - "wrt EO" column indicates the difference in percentage between the natural frequencies of couple of blades, while below each frequency the red percentage indicates the difference with respect to the baseline

MODE	Base Line [Hz]	a = 5 b = 10 c =		wrt EO [%]	a = 10 b = 20 c = 2		wrt EO [%]	a = 10 b = 20 c = 3		wrt EO [%]
		MAT [Hz]	GEO [Hz]		MAT [Hz]	GEO [Hz]		MAT [Hz]	GEO [Hz]	
1st Flap	0.614	0.609 -0.8%	0.608 -0.9%	0.2%	0.606 -1.3%	0.594 -3.3%	2.0%	0.602 -1.9%	0.580 -5.5%	3.6%
1st Edge	0.937	0.931 -0.1%	0.925 -1.3%	0.6%	0.931 -0.6%	0.909 -3.0%	2.4%	0.931 -0.6%	0.895 -4.5%	3.9%
2nd Flap	1.732	1.730 -0.1%	1.726 -0.3%	0.2%	1.721 -0.6%	1.656 -4.4%	3.8%	1.708 -1.4%	1.566 -9.6%	8.2%
2nd Edge	2.744	2.755 +0.4%	2.739 -0.2%	0.6%	2.754 +0.4%	2.668 -2.3%	3.1%	2.753 +0.3%	2.596 -5.4%	5.7%
3rd Flap	3.555	3.557 +0.1%	3.560 +0.1%	0.1%	3.534 -0.6%	3.419 -3.8%	3.2%	3.509 -1.3%	3.283 -7.6%	6.3%
3rd Edge	5.628	5.664 +0.6%	5.653 +0.4%	0.2%	5.651 -0.6%	5.507 -2.1%	2.5%	5.642 +0.2%	5.368 -2.8%	3.0%

4th Flap	6.052	6.087 +0.6%	6.095 +0.7%	0.1%	6.055 +0.1%	5.879 -2.8%	2.9%	6.029 -0.4%	5.715 -5.6%	6.0%
1st Torsion	6.709	6.621 -1.3%	6.665 -0.7%	0.6%	6.613 -1.4%	6.727 +0.3%	1.7%	6.607 -1.5%	7.034 +4.6%	5.1%

A list of observations can be made looking at the natural frequencies of the isolated blades:

1. Natural frequencies of the straight blades with material bend twist coupling do not deviate from the natural frequencies of the baseline by more than 1.5%
2. For the case with low sweep coefficients ($a = 5$, $b = 10$, $c = 2$), natural frequencies of the geometric and material coupled blades are extremely close
3. For larger sweeps (b coefficient) and different sweeping curvature (c coefficient), the natural frequencies of the geometric coupled blades deviate both from the baseline and the respective material coupled blades; the deviations are due to the increased masses and lengths of the swept blades.

An overview of the first 10 natural frequencies of the full wind turbine configurations used for the current study is reported in Table 5.

Table 5 - Natural Frequencies comparison, full wind turbine – “wrt EO” column indicates the difference in percentage between the natural frequencies of couple of blades, while below each frequency the red percentage indicates the difference with respect to the baseline

MODE	Base Line [Hz]	a = 5 b = 10 c = 2		wrt EO [%]	a = 10 b = 20 c = 2		wrt EO [%]	a = 10 b = 20 c = 3		wrt EO [%]
		MAT [Hz]	GEO [Hz]		MAT [Hz]	GEO [Hz]		MAT [Hz]	GEO [Hz]	
1st Tower Side2Side	0.251	0.251 0.0%	0.251 0.0%	0.0%	0.251 0.0%	0.251 0.0%	0.0%	0.251 0.0%	0.250 -0.4%	0.4%
1st Tower Side2Side	0.254	0.254 0.0%	0.254 0.0%	0.0%	0.254 0.0%	0.254 0.0%	0.0%	0.254 0.0%	0.253 -0.3%	0.3%
1st Fix-Free	0.504	0.502 -0.4%	0.499 -0.9%	0.5%	0.501 -0.6%	0.495 -1.8%	1.2%	0.501 -0.6%	0.489 -3.0%	2.4%
1st Asymmetric Flap-Yaw	0.550	0.546 -0.7%	0.544 -1.0%	0.3%	0.543 -1.3%	0.534 -2.9%	1.6%	0.541 -1.6%	0.524 -4.7%	3.1%
1st Asymmetric Flap-Tilt	0.591	0.586 -0.8%	0.589 -0.3%	0.5%	0.584 -1.2%	0.572 -3.2%	2.0%	0.580 -1.9%	0.560 -5.2%	3.1%
1st Collective Flap	0.635	0.630 -0.8%	0.629 -0.9%	0.1%	0.627 -1.2%	0.614 -3.3%	2.1%	0.622 -2.0%	0.598 -5.8%	3.8%
1st Asymmetric Edge 1*	0.927	0.922 -0.5%	0.915 -1.3%	0.7%	0.922 -0.5%	0.900 -2.9%	2.4%	0.922 -0.5%	0.888 -4.2%	3.7%
1st Asymmetric Edge 2**	0.940	0.934 -0.6%	0.928 -1.2%	0.6%	0.934 -0.6%	0.913 -2.9%	2.3%	0.934 -0.6%	0.898 -4.5%	2.9%
2nd Asymmetric Flap-Yaw	1.371	1.369 -0.1%	1.366 -0.4%	0.3%	1.363 -0.6%	1.323 -3.4%	2.8%	1.357 -1.0%	1.264 -7.8%	6.8%
2nd Asymmetric Flap-Tilt	1.540	1.537 -0.2%	1.534 -0.4%	0.2%	1.531 -0.6%	1.483 -3.7%	3.1%	1.522 -1.2%	1.415 -8.1%	6.9%

*edge1: blade1 (pointing upward) is almost standstill and other two blades are asymmetrically excited mode.

**edge2: blade2 is almost standstill and other two blade are asymmetrically excited mode.

Tower modes are not affected by the different blade configurations. However, looking at higher natural frequencies of the full structure, large deviations from the baseline are registered for large sweep configurations. These differences can be again explained with the increased rotor mass and the increased length of the different swept blade configurations. A larger increment in mass and length produces larger deviations from the baseline natural frequencies.

Moreover, straight blades with material coupling have in general natural frequencies close to the baseline frequencies. Geometric coupling has a larger effect on natural frequencies than material coupling.

Aerodynamic Power, Pitch Angle and Rotational Speed Steady States – 2nd Load Case

Subjecting the 6 different configurations to a deterministic wind speed steps load case, aerodynamic power, pitch angle and rotational speed steady states are computed and discussed.

Results for the power output sensor are reported in Figure 8. Looking below rated conditions, all the configurations generate higher power at low wind speeds, especially the geometric coupled configurations. At 8 and 10 m/s, blades with high coupling lose almost 5% of the power compared to the baseline, due to the decrease in the angle of attack. This negative variation in the power curve can be compensated using the same methods reported to close the gap between the optimized angle of attack distribution and the targeted one:

1. Re-computing the static structural twist
2. Forcing the blade to actively pitch toward stall below rated wind speed

Then again, the implementation of these two methods and their effects on the different wind turbine passively controlled models will be evaluated in future works.

The controller selects lower pitch angles above rated wind speed because of the bend-twist coupling effect. The differences in the blade pitch steady states for the various configurations analyzed are plotted in Figure 9.

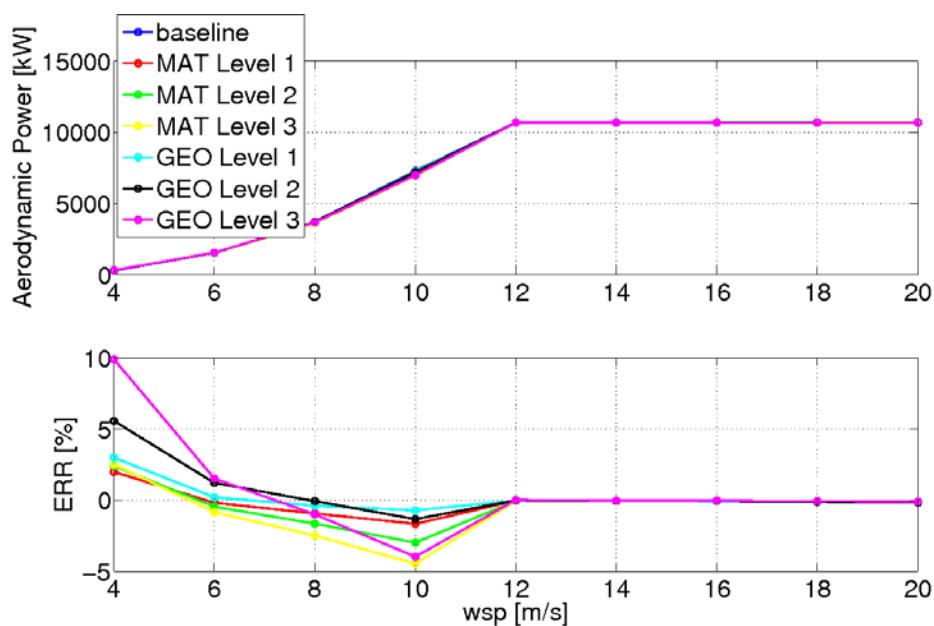


Figure 8 - Comparison of the Aerodynamic Power of the baseline and the coupled configurations - Variation plotted below

Small deviations (order of 1.5%) from the baseline are also registered for the rotational speed (Figure 10). At 8 and 10 m/s, the higher the coupling the slower is the rotor. For all the three sensors analysed in this paragraph, it is important to remark that the different couples of material-geometric coupled blades always slightly differ from each other.

In general, these differences from the baseline and between each couple of blades are going to produce deviations in the loads computed and in the beneficial reduction that they can achieve.

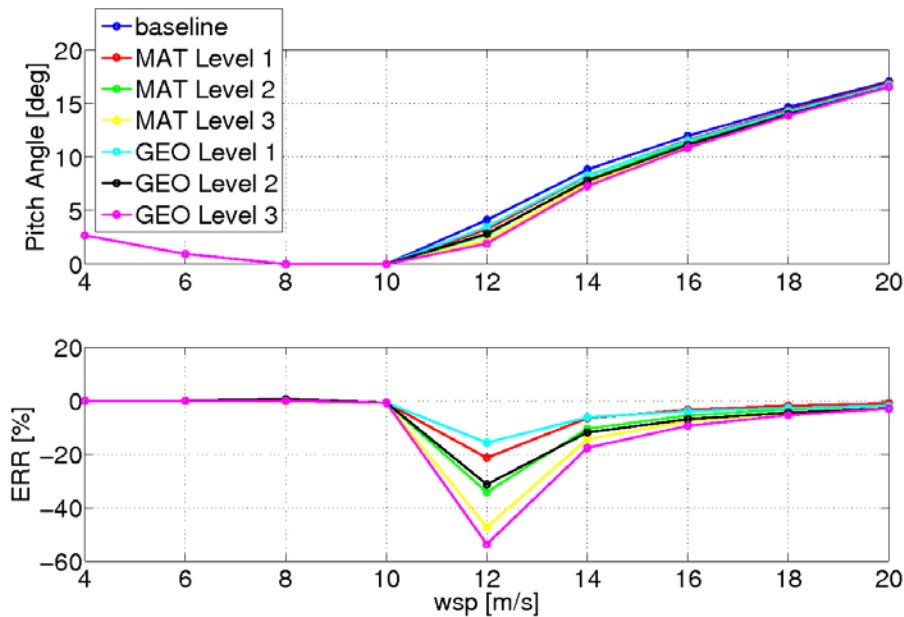


Figure 9 - Pitch angle steady states (above) and Variation compared to the baseline (below) of the different configurations

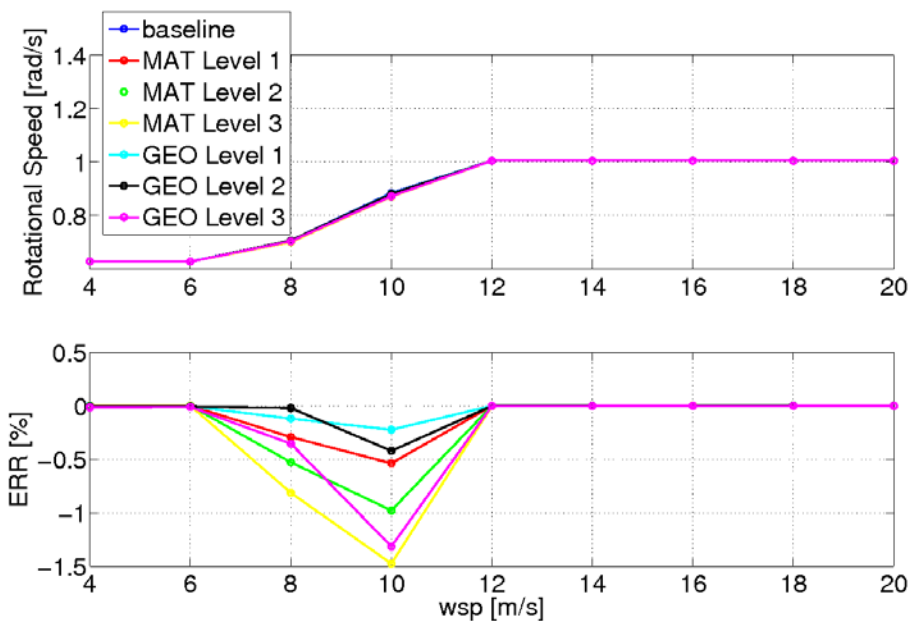


Figure 10 - Rotational Speed steady states (above) and Variation compared to the baseline (below) of the different configurations

To anticipate one the conclusions: a “fair” comparison is needed to produce a better analysis of these passive control techniques that varies according to the amount of bend-twist coupling. Different couplings generate an effect on the power output of the turbine below rated wind speed and on the dynamics of its pitch controller. Below rated wind speed, it is difficult to establish if a load reduction for a certain configuration with respect to the baseline is achieved because of a positive effect produced by the coupling or because of a loss in the power output. Moreover, if the use of bend-twist feature affects the dynamics of the controller, what will the repercussion be on fatigue loads? The wind turbine configurations need to have the same power curves and “ad hoc” controller tuning.

Extreme and Fatigue Loads – 3rd Load Case

Results in terms of extreme and fatigue loads for the 3rd load case are reported in this paragraph.

All the plots have the same outfit:

1. Main plots are listed for each sensor and each coupling level (Level 1, 2 and 3)
2. Main plots are divided in two bar subplots
3. First subplot shows the values from the sensors investigated for each wind speed and for baseline, material (MAT) and geometric (GEO) coupling
4. Bottom subplot shows the variation of MAT and GEO from the baseline for each wind speed

Damage Equivalent Load with a material exponent depending on the component of the turbine considered for reference frequency of 1Hz is plotted for the fatigue analyses. According to Verelst and Larsen [1], the most beneficial effect can be observed on the blade root flapwise bending moment for both extreme and fatigue loads. Figures 11-13 show extreme loads for the blade root flapwise bending moment. Figures 14-16 show the fatigue loads for the same sensor.

The higher the coupling levels the higher the load reduction achieved by the configurations. Couples of blades on the same level produce similar reductions on fatigue loads and with deviations at 14 m/s and above rated wind speed for coupling Level 3 on extreme loads. Maximum reduction is in the order of 20% for extreme loads and of 25% fatigue loads close to the operational wind speed. General reductions around 10% for fatigue and extreme loads are registered for the other wind speeds.

Extreme and fatigue load reductions are monitored also for blade root edgewise bending moment (extreme loads reported in Figures 17-19, fatigue loads reported in Figures 20-22). Alleviations or increases in extreme and fatigue loads for the blade root edgewise bending moment are not excessive and always below a 5% threshold. Deviations between the different types of coupling are registered, with a major difference regarding fatigue loads: while geometric coupling increases fatigue blade edgewise loads as already reported by Verelst and Larsen [1], material coupling show general load alleviation.

Figures 23-25 and Figures 26-28 show extreme and fatigue blade root torsional moment respectively. Even though the geometric coupled blades have a forward sweep term to compensate the large torsional moment on the root, large load increases from the baseline and from the MAT blades can be observed for both extreme and fatigue loads. Larger deviations in torsional moment are registered for more extreme sweeps. MAT coupling show alleviations for both extreme and fatigue loads.

Positive load alleviations are achieved for extreme shaft torsion moments (Figures 29-31) below rated wind speed with no appreciable differences above rated. Fatigue shaft torsion moments (Figures 32-34) are alleviated below 12 m/s and are increased above. The two types of coupling show similar reductions and increases for this sensor. Maximum reduction of 8% for extreme loads is registered around 10 m/s for the highest level of coupling. Below rated wind speed the fatigue loads are reduced up to 10% while they increase by 10% around rated.

Extreme and fatigue tower base fore-aft bending moments generally decrease for the different configurations along all the wind speed range, as shown in Figure 35-37 (extreme), Figures 38-40 (fatigue). An increase is registered for extreme loads at 14 m/s for all the coupling levels. The maximum of the extreme time series is near the rated wind speed for the baseline while it shifts to higher wind speeds for the bend twist coupled configurations. It is possible to generally observe similar reductions for the blades with same amount of material-geometric coupling, with minor deviations that increase for higher coupling levels. For the tower bottom fore-aft bending moment, load alleviations can touch peak of 20% for extreme loads and 10% for fatigue loads.

Large differences between the effects brought by the two couplings on extreme and fatigue loads of the tower bottom side-to-side bending can be observed looking at Figures 41-43 and Figures 44-46 respectively. No clear trend can be registered and further analysis about the effect of the bend-twist coupling on the tower side-to-side dynamic behaviour needs to be carried.

In general, the observations made thus far can be summarized as follows:

1. The computed material bend-twist coupling achieves similar load reductions (always within a range of 3%) compared to the targeted geometric coupling for blade root flapwise bending, shaft torsional and tower fore-aft base extreme and fatigue moments
2. Swept blade have large increased blade root torsional extreme and fatigue moments, even though a linear forward sweep has been added to compensate this effect
3. Qualitatively different results have been obtained for swept and material coupled straight blades for the blade root edgewise and tower base side-to-side bending moments; these loads are in close relation and the deviations registered for the blade edgewise loads explain the deviations obtained for the tower bottom side-to-side loads
4. Closer match and more accurate estimation of the different alleviations can be achieved with a fair comparison based on wind turbines with same power curves and “ad hoc” controller tuning. A reduction of the error between the angle of attack distributions in the optimization framework can definitely produce improvements in the comparison between material and geometric coupled blades with the same amount of bend-twist coupling. Further investigations need to be carried with regards to swept blade root torsional moments and blade edgewise loads

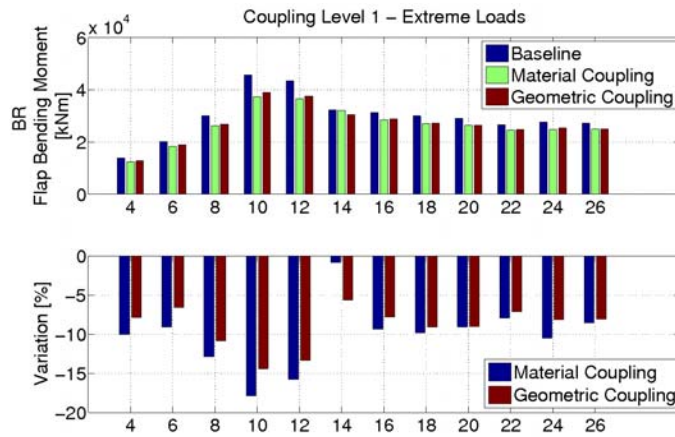


Figure 11 - Extreme - Blade Root Flapwise Bending Moment, Values and Variation with respect to baseline - Level 1 -

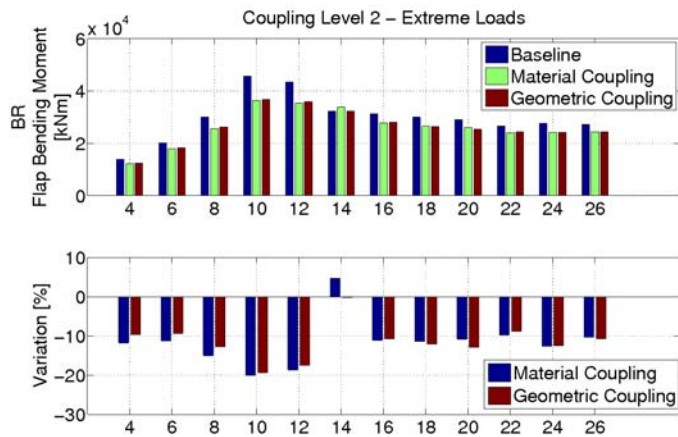


Figure 12- Extreme - Blade Root Flapwise Bending Moment, Values and Variation with respect to baseline - Level 2 -

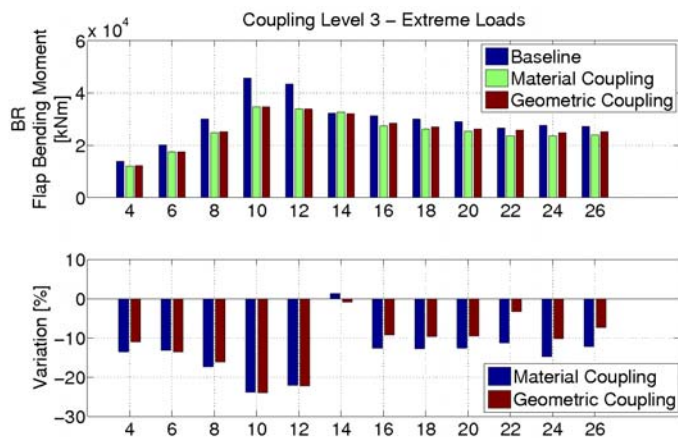


Figure 13- Extreme - Blade Root Flapwise Bending Moment, Values and Variation with respect to baseline - Level 3 -

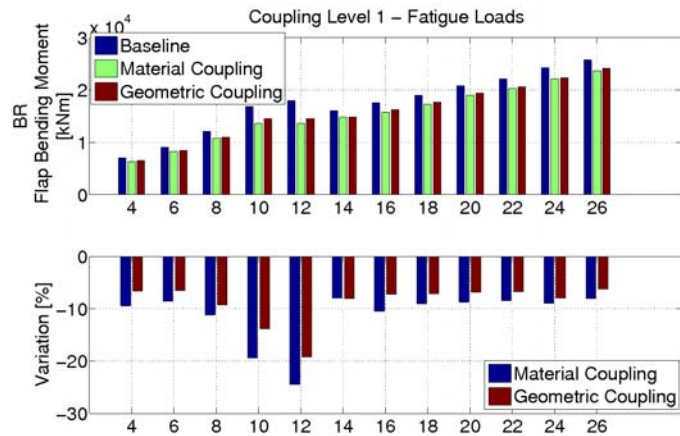


Figure 14 – Fatigue - Blade Root Flapwise Bending Moment, Values and Variation with respect to baseline - Level 1 -

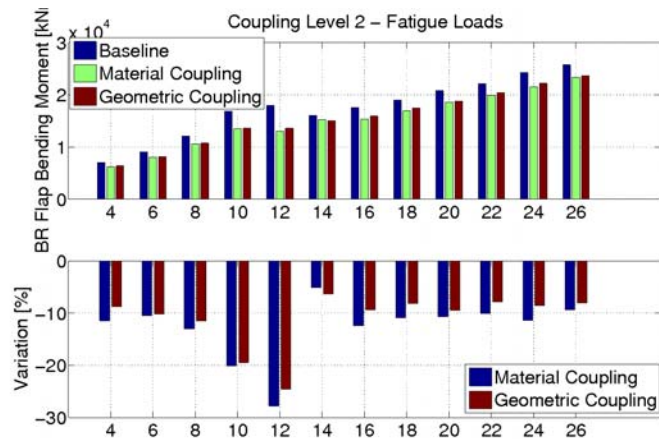


Figure 15 – Fatigue - Blade Root Flapwise Bending Moment, Values and Variation with respect to baseline - Level 2 -

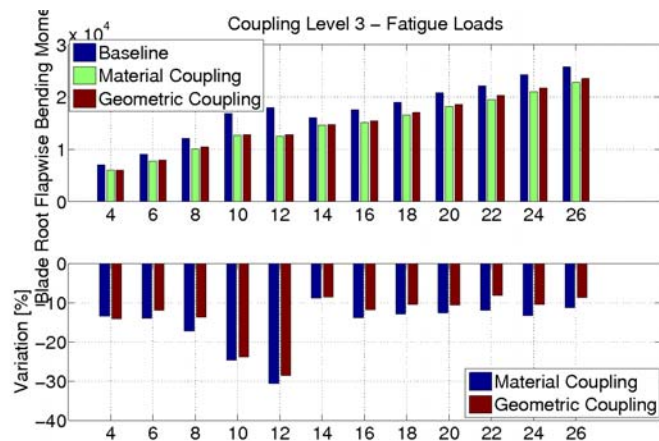


Figure 16 – Fatigue - Blade Root Flapwise Bending Moment, Values and Variation with respect to baseline - Level 3 -

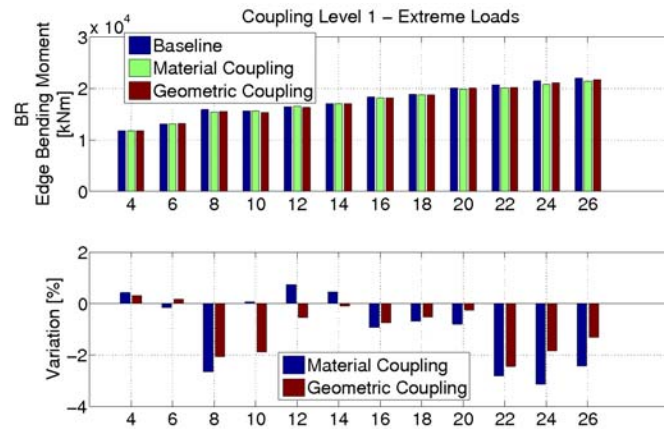


Figure 17- Extreme - Blade Root Edgewise Bending Moment, Values and Variation with respect to baseline - Level 1 -

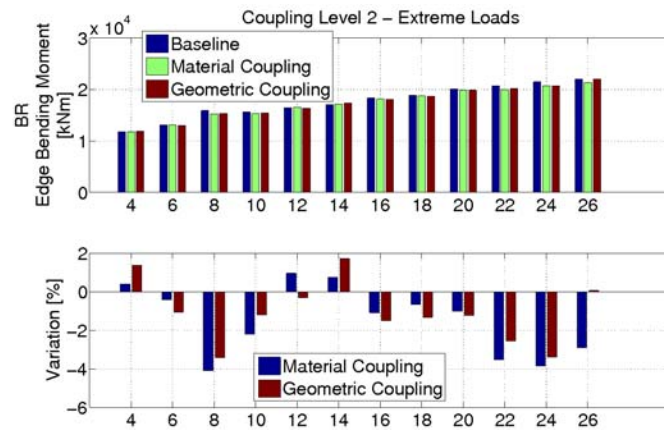


Figure 18- Extreme - Blade Root Edgewise Bending Moment, Values and Variation with respect to baseline - Level 2 -

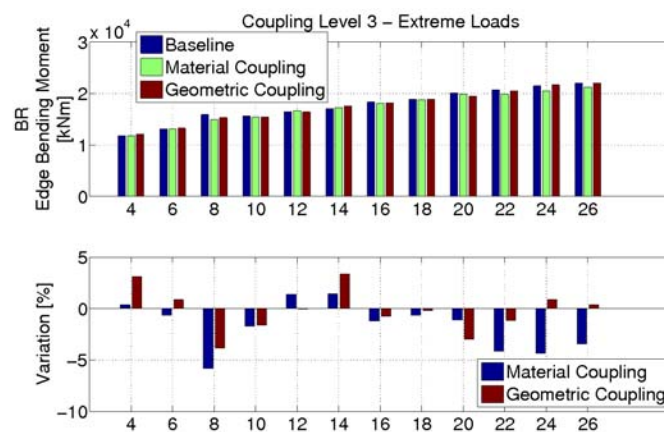


Figure 19- Extreme - Blade Root Edgewise Bending Moment, Values and Variation with respect to baseline - Level 3 -

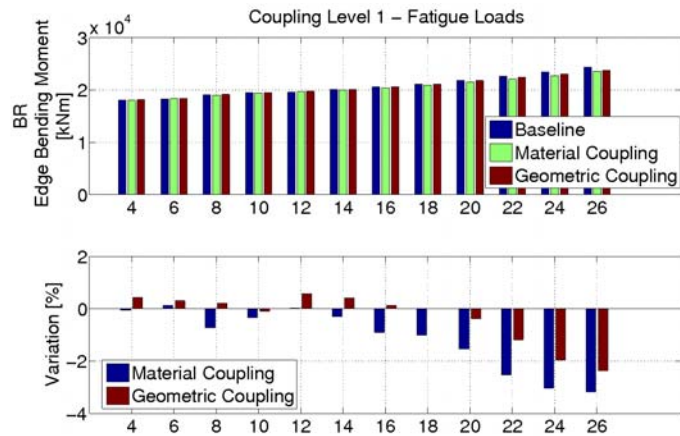


Figure 20- Fatigue - Blade Root Edgewise Bending Moment, Values and Variation with respect to baseline - Level 1 -

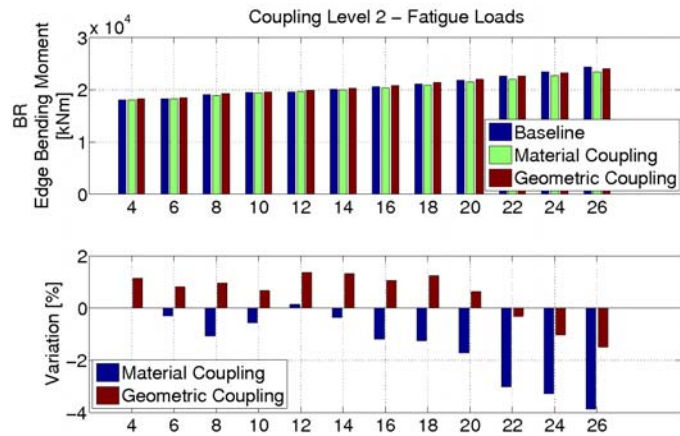


Figure 21- Fatigue - Blade Root Edgewise Bending Moment, Values and Variation with respect to baseline - Level 2 -

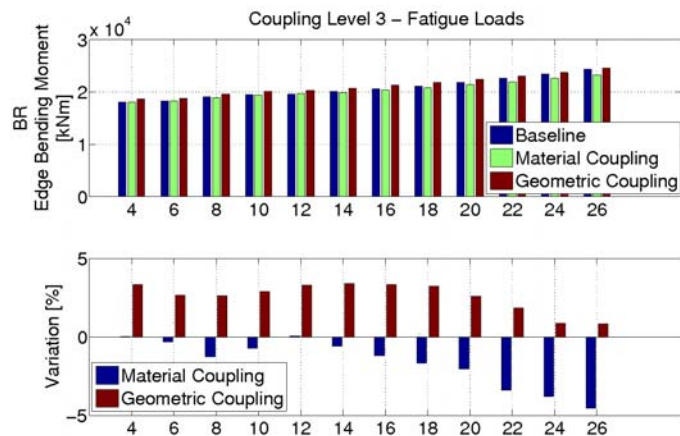


Figure 22- Fatigue - Blade Root Edgewise Bending Moment, Values and Variation with respect to baseline - Level 3 -

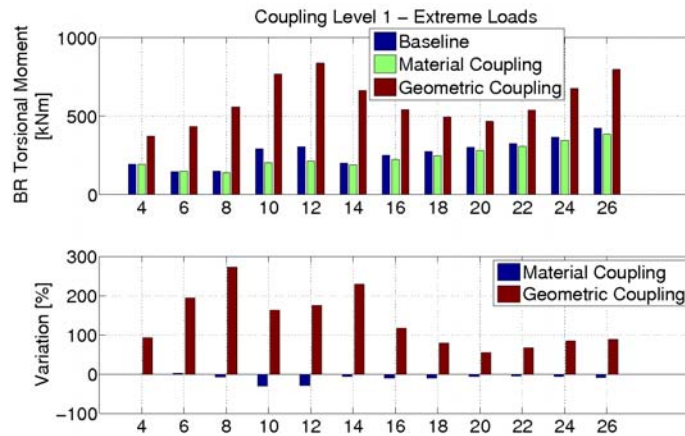


Figure 23- Extreme - Blade Root Torsional Moment, Values and Variation with respect to baseline - Level 1 -

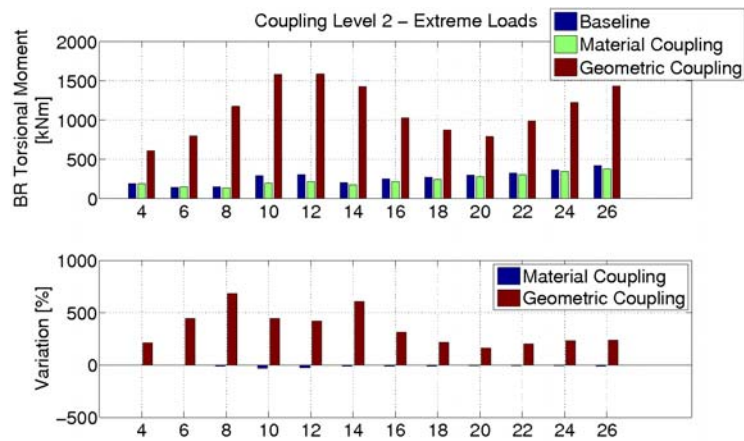


Figure 24- Extreme - Blade Root Torsional Moment, Values and Variation with respect to baseline - Level 2 -

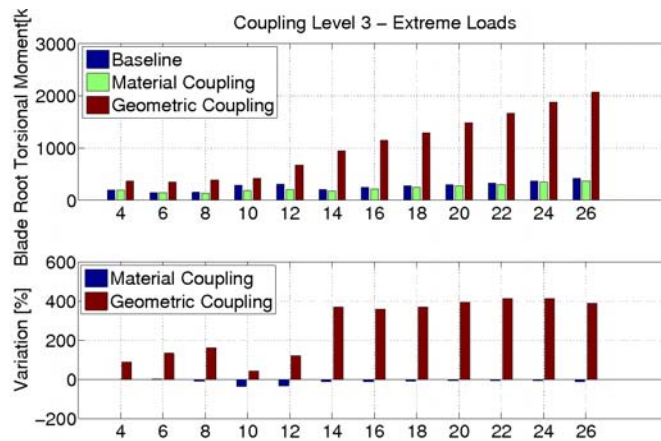


Figure 25- Extreme - Blade Root Torsional Moment, Values and Variation with respect to baseline - Level 3 -

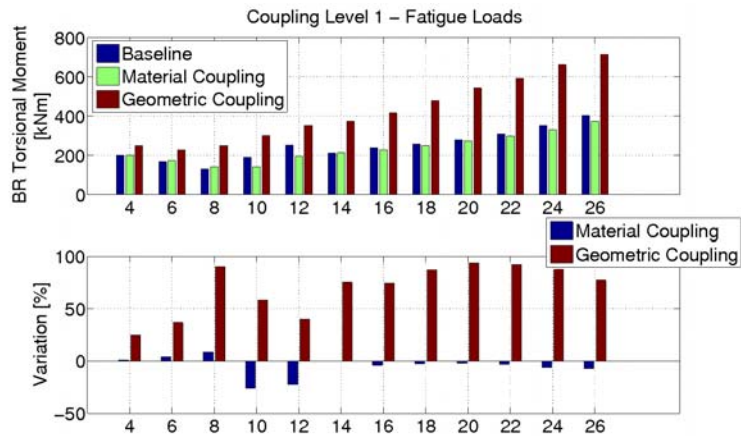


Figure 26- Fatigue - Blade Root Torsional Moment, Values and Variation with respect to baseline - Level 1 -

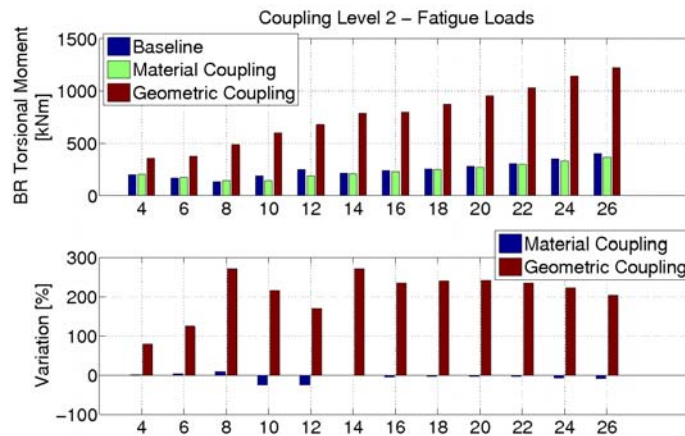


Figure 27- Fatigue - Blade Root Torsional Moment, Values and Variation with respect to baseline - Level 2 -

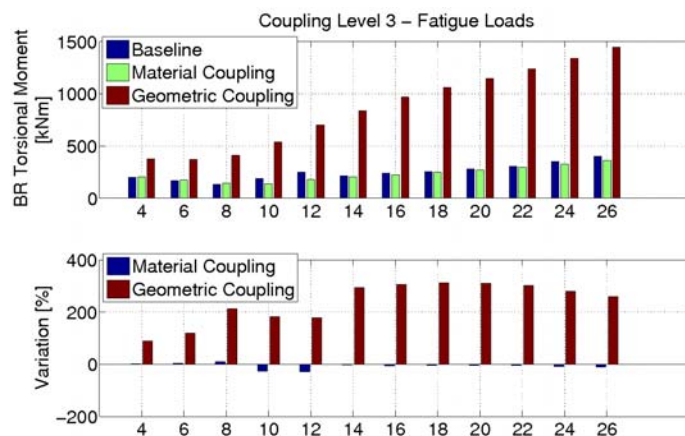


Figure 28- Fatigue - Blade Root Torsional Moment, Values and Variation with respect to baseline - Level 3 -

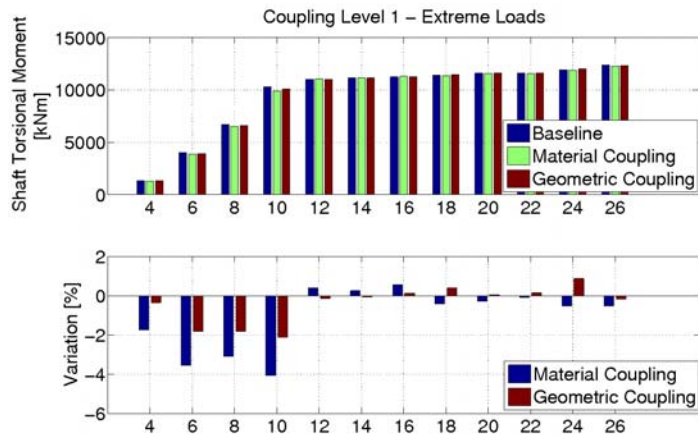


Figure29– Extreme - Shaft Torsional Moment, Values and Variation with respect to baseline - Level 1 –

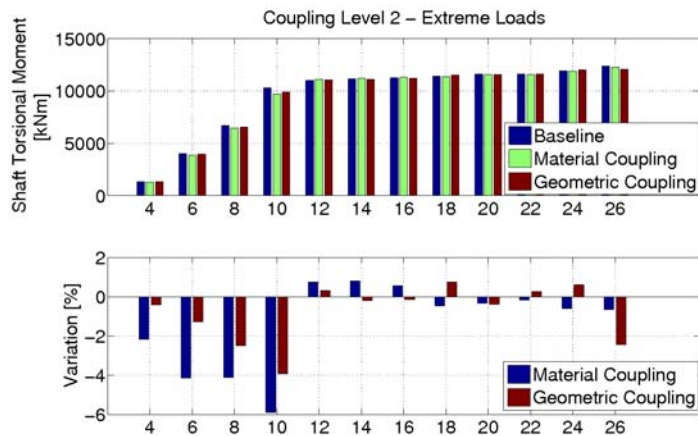


Figure 30– Extreme - Shaft Torsional Moment, Values and Variation with respect to baseline - Level 2 –

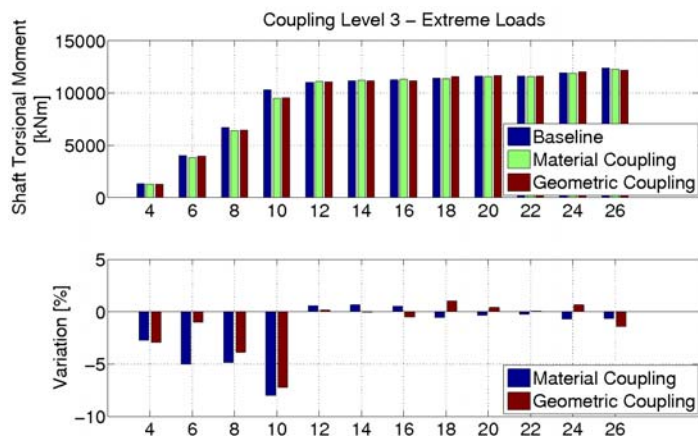


Figure 31– Extreme - Shaft Torsional Moment, Values and Variation with respect to baseline - Level 3 –

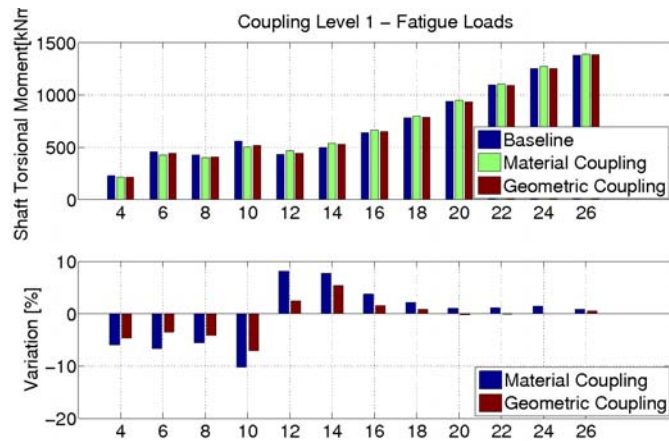


Figure 32- Fatigue - Shaft Torsional Moment, Values and Variation with respect to baseline - Level 1 -

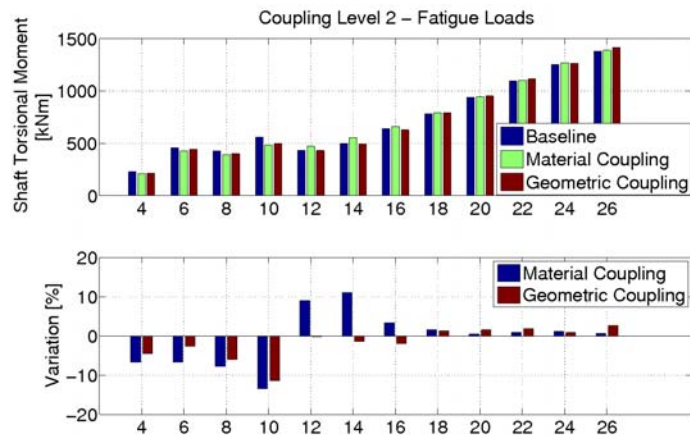


Figure 33- Fatigue - Shaft Torsional Moment, Values and Variation with respect to baseline - Level 2 -

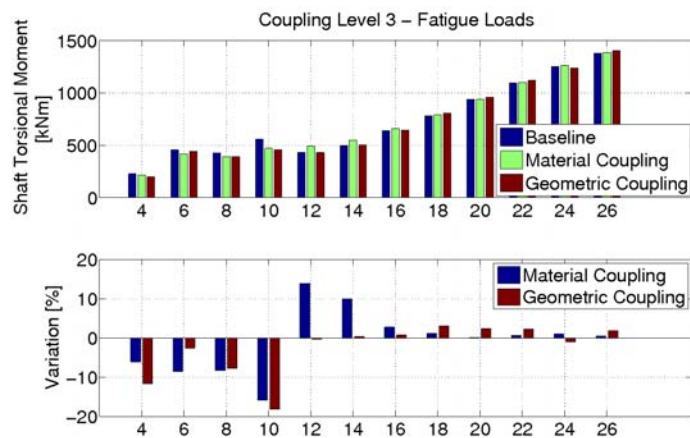


Figure 34- Fatigue - Shaft Torsional Moment, Values and Variation with respect to baseline - Level 3 -

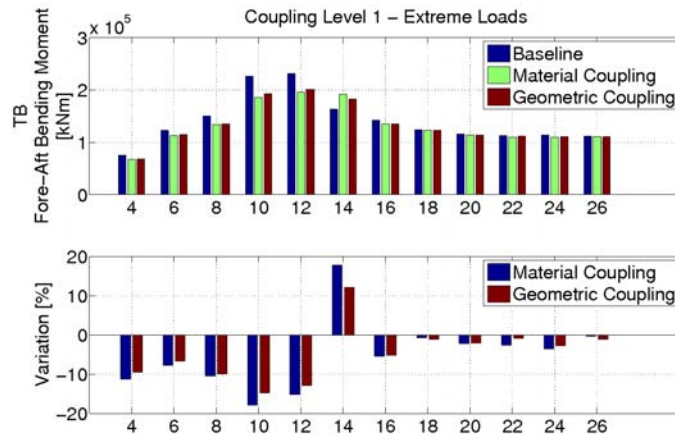


Figure 35 - Extreme - Tower Bottom Fore-Aft Bending Moment, Values and Variation with respect to baseline - Level 1 -

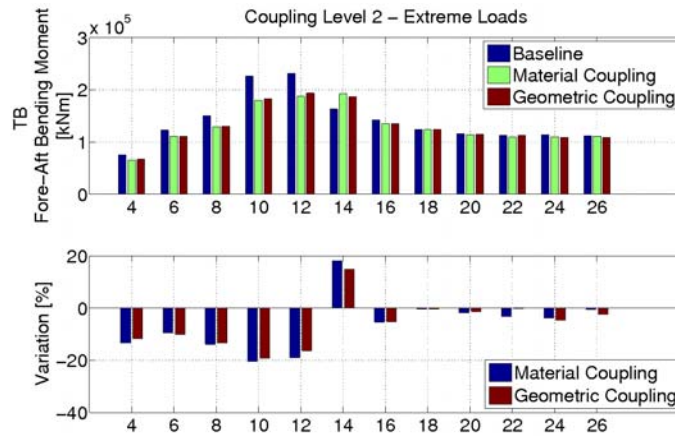


Figure 36- Extreme - Tower Bottom Fore-Aft Bending Moment, Values and Variation with respect to baseline - Level 2 -

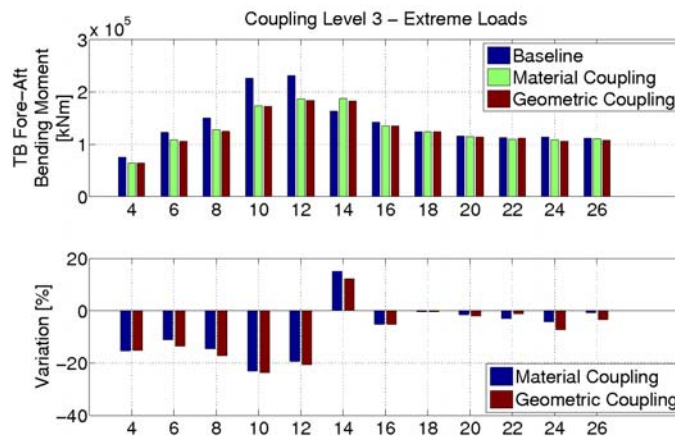


Figure 37- Extreme - Tower Bottom Fore-Aft Bending Moment, Values and Variation with respect to baseline - Level 3 -

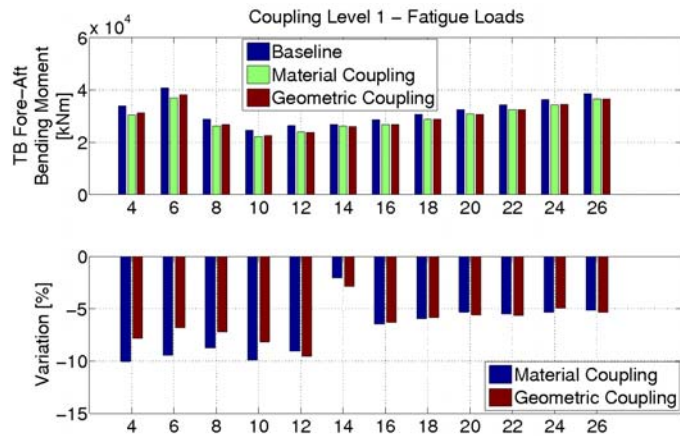


Figure 38- Fatigue - Tower Bottom Fore-Aft Bending Moment, Values and Variation with respect to baseline - Level 1 -

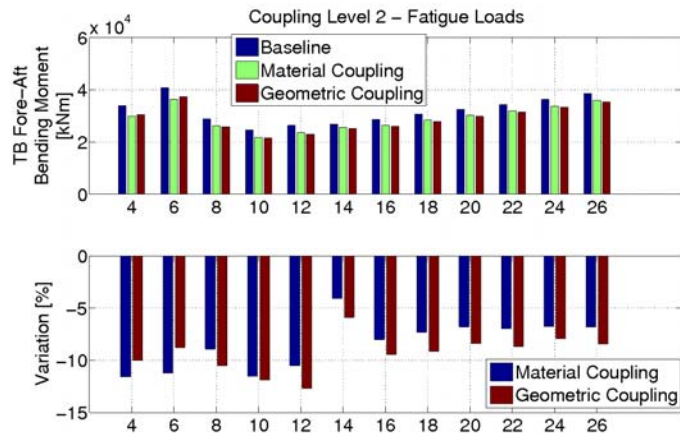


Figure 39- Fatigue - Tower Bottom Fore-Aft Bending Moment, Values and Variation with respect to baseline - Level 2 -

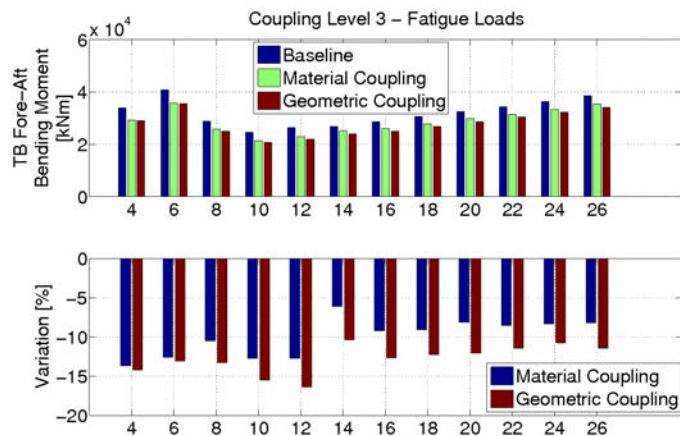


Figure 40- Fatigue - Tower Bottom Fore-Aft Bending Moment, Values and Variation with respect to baseline - Level 3 -

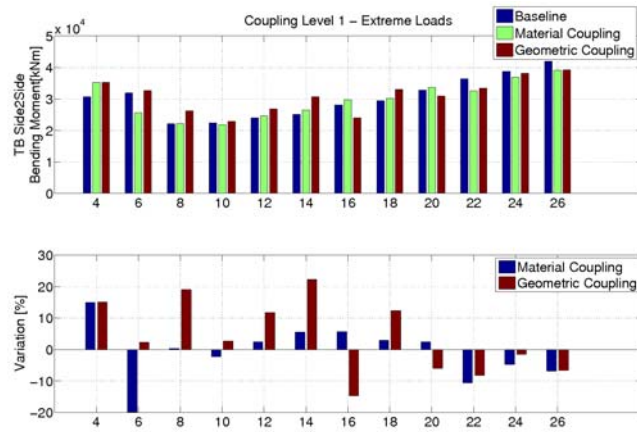


Figure 41- Extreme - Tower Bottom Side2Side Bending Moment, Values and Variation with respect to baseline - Level 1 -

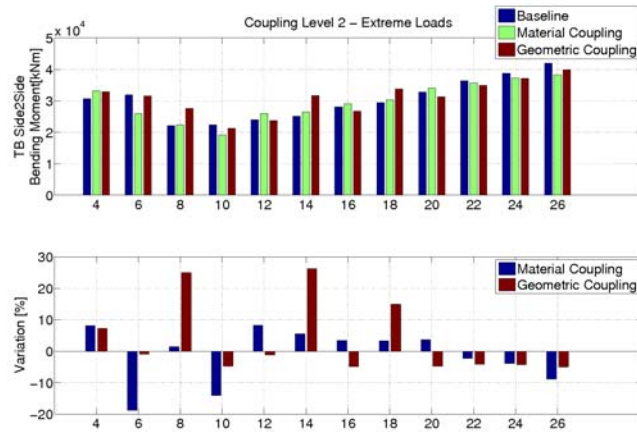


Figure 42- Extreme - Tower Bottom Side2Side Bending Moment, Values and Variation with respect to baseline - Level 2 -

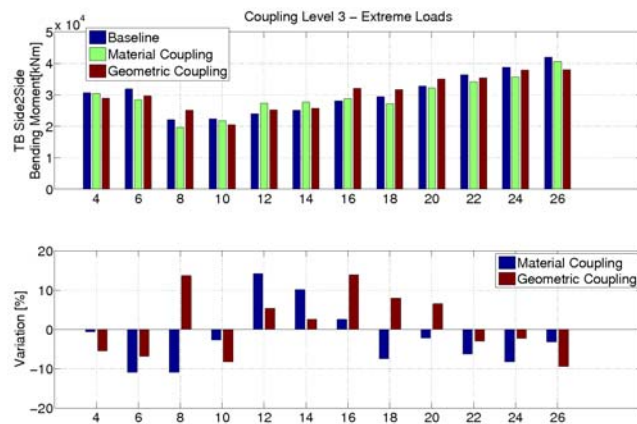


Figure 43 - Extreme - Tower Bottom Side2Side Bending Moment, Values and Variation with respect to baseline - Level 3 -

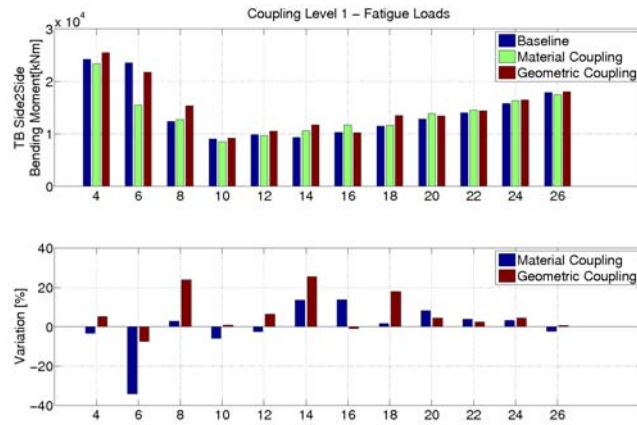


Figure 44 - Fatigue - Tower Bottom Side2Side Bending Moment, Values and Variation with respect to baseline - Level 1 -

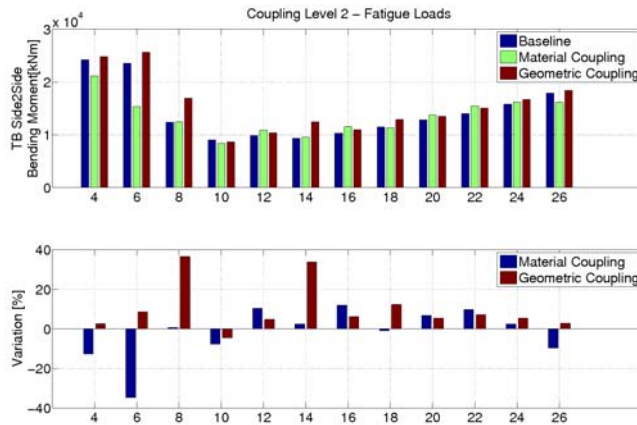


Figure 45 - Fatigue - Tower Bottom Side2Side Bending Moment, Values and Variation with respect to baseline - Level 2 -

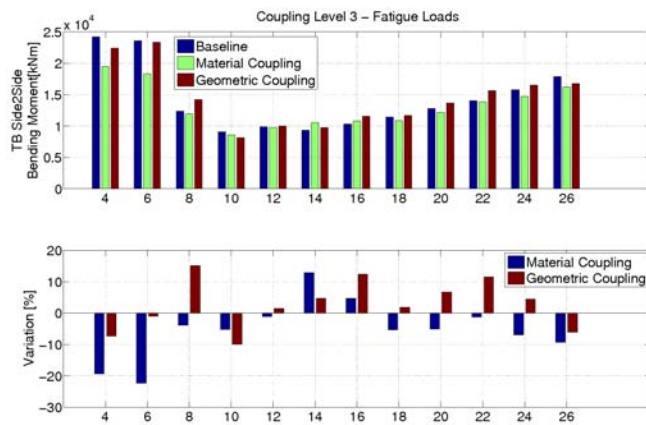


Figure 46 - Fatigue - Tower Bottom Side2Side Bending Moment, Values and Variation with respect to baseline - Level 3 -

4.5 Conclusions/Outlook

Years of research have been carried on passive control methodologies for wind turbines to prove their effectiveness and applicability on real machines. Except for rare cases, they have not been widely used by industry and systematically implemented in the blade design process. The reason is the absence of definite guidelines regarding possible regulation to achieve determined positive load alleviation effects, minimizing possible drawbacks.

The study described throughout this chapter aims at taking a first step to establish a scheme for introducing a regulated passive control so that the wind turbine can behave according to a prescribed behavior. Following the path drawn by previous analyses carried by DTU, three swept blade configurations have been selected because of the positive properties shown in terms of load alleviation effects. Three straight blades have been structurally tuned to match the distribution of the angle of attack of the swept blades chosen, through the selection of a bend-twist coupling term to plug into the constitutive matrices of the blade sections. Natural frequencies have been compared along with power curves and extreme and fatigue loads. The analysis of the load cases implemented showed that:

- A fair matching between the angle of attack distributions is achieved and better results can be obtained if instead of selecting a single coupling coefficient for all the sections along the blade span, an α for each blade section is found
- Very high and unrealistic coupling coefficients have been computed; it is important to be aware about the amount of material bend-twist coupling that can be implemented on real blades and consequentially pose constraints to the optimization problem
- Natural Frequencies of the material coupled configurations of the isolated blade and the wind turbines are close to the baseline, while the geometric coupled blades deviate the further from the baseline the higher is the coupling; these deviations are due to changes in mass and length of the blade
- Bend-twist coupled blades have a lower power production below rated wind speed due to a decrease in the angle of attack and show different dynamics of the controller; a fair comparison is needed, based on configurations with equal power curves and proper controller tuning, so that reliable observations can be made on the actual effects on the loads
- Different types of coupling show the same effects on extreme and fatigue blade flapwise, tower fore-aft and shaft torsion loads
- Swept blades largely affect blade root torsional bending moment, even though geometrical changes have been made in order to limit this effect
- Different effects on the blade edgewise bending loads produce an effect on the tower side-to-side loading; a more detailed investigation is needed to understand the difference between using geometric or material coupling on the blade edgewise behavior

To conclude: the regulation of the material coupling implemented match the target for certain loads on the structure. One of the main problems to render the procedure more general and fitted to express useful guidelines, are related to the selection of the angle of attack distribution (if a target geometric coupling is missing, how is it possible to select “ad hoc” angle of attack distributions that represent an “optimal” behavior?). The need for a fair benchmarking has also been highlighted, since the different configurations have different power curves. Hence, it is not possible to establish if the load alleviation derives

from a positive effect of the bend-twist coupling or from a power loss. Controller tuning must also be taken into account.

Future work will focus on improvements to the optimization framework in order to include constraints regarding the implementation of realistic material bend-twist coupling for each section along the blade span. At the actual state the targeted angle of attack distributions have been chosen through selection of certain blade geometries. Study will be carried in relation to the identification of angle of attack distributions that can generate prescribed load alleviations limiting the negative consequences. Research on fair comparisons based on matching power curves and controller tuning of bend-twist coupled blades are being carried at the moment.

4.6 References

- [1] D.R.S. Verelst, T.J. Larsen, "Load Consequences when Sweeping Blades - A Case Study of a 5 MW Pitch Controlled Wind Turbine," Risø-R-1724(EN), Risø DTU, August 2010.
- [2] T.J.Larsen, A.M.Hansen, *How 2 HAWC2, the user's manual*, Roskilde, Denmark: June 2013, June 2013.
- [3] M.H.Hansen, "Aeroelastic properties of backward swept blades," in *49th AIAA Aerospace Sciences Meeting*, Orlando, Florida, 4-7 January 2011.
- [4] J. Jonkman, S. Butterfield, W. Musial and G. Scott, "Definition of a 5MW Reference Wind Turbine for Offshore System Development," NREL/TP-500-38060, Golden, Colorado 80401-3393, February 2009.
- [5] P.Berring, K.Branner, C. Berggreen, H.W.Knudsen, "Torsional Performance of wind turbine blades - Part 1: Experimental Investigation," in *International conference on composite materials (ICCM-16)*, Kyoto, Japan, 2007.
- [6] Branner K., Berring P., C. Berggreen, HW, Knudsen, "Torsional Performance of wind turbine blades - Part 2: Experimental Investigation," in *International Conference on composite materials (ICCM-16)*, Kyoto, Japan, 2007.
- [7] "UpWind, Design limits and solutions for very large wind turbines," EUPD - Sixth Framework Programme, March 2011.
- [8] P. H. Jensen, "UpWind Activity Report year 4," EUPD - Sixth Framework Programme, 28th February 2010.
- [9] C. Bak, F. Zahle, R. Bitsche, T. Kim, A. Yde, L.C. Henriksen, A. Natarajan, M.H. Hansen, "Description of the 10 MW Reference Wind Turbine," DTU Wind Energy Report-I-0092, Roskilde, Denmark, July 2013.
- [10] F. Vorpahl, M. Strobel, M. Jonkman, T.J.Larsen, P. Passon, "Verification of aeroelastic offshore wind turbine design codes under IEA wind task XXIII," *Journal of Wind Energy*, no. doi:10.1002/we.1588, 2013.
- [11] Popko, W., Vorpahl, F., Zuga, A., Kohlmeier, M., Jonkman, J., Robertson, A., Larsen, T.J., Yde, A., Stertr, K., Okstad, K.M., et al., "Offshore code comparison collaboration continuation (OC4), PHASE I - results of coupled simulations of an offshore wind turbine with jacket support structure," in *Proceedings of the International Offshore and Polar Engineering Conference*, 2012;337-346, 2012.
- [12] Larsen, T.J., Aagard Madsen, H., Larsen, G.C. and Hansen, K.S., "Validation of the dynamic wake meander model for loads and power production in the Egmond Aan Zee wind farm," *Journal of Wind Energy*, vol. 16(4), no. doi:10.1002/we.1563, pp. 605-624, 2013.
- [13] Kim, T., Hansen, A.M., and Branner, K., "Development of an Anisotropic Beam Finite Element for Composite Wind Turbine Blades in Multibody System," *Journal of Renewable Energy*, vol. doi:10.1016/j.renene.2013.03.033, pp. 59:172-183, 2013.
- [14] M. -. Matlab, *Optimization Toolbox - User's Guide R2014a*, Natick, MA: The MathWorks, Inc., March 2014.

5 CONCLUSIONS

In this report different concepts have been presented to control the load along the span of the blade. Some of the concepts have been introduced in previous EU projects and national project (e.g. UPWIND). However, the objective of this deliverable was to look at the technical feasibility and readiness of the different concepts. We can conclude that for the different concepts different readiness levels can be identified.

If we look at the SMA morphing wing concept we can conclude that the technical feasibility is promising. In this deliverable technical solutions have been proposed to increase the fatigue life-time and the bandwidth of the SMA actuator, which are critical technical breakthroughs to make this concept feasible.

For the passive flap concept we can conclude that this is a novel concept by itself and the preliminary analysis conducted so far on a simplified model shows potential in the reduction of the loads on the rotor. High-fidelity simulations have to be performed to fully proof the concept and one or more technical solutions have to be found to develop a working prototype.

Material and geometric coupling concepts have already shown their potential as a concept. In this deliverable technical design guidelines are introduced to enhance the technical readiness. The analysis carried out confirmed the potential of this passive control strategy. Improvements to the optimization framework and to the comparison between the different configurations of the wind turbine used for the simulations must be introduced to further mature the concept.

Although the load reduction capabilities of the first three concepts seem to be promising it is believed that a combination of the different concepts will further increase the design space to shape the loads. In the upcoming years high fidelity simulations will be performed of several different combinations such as:

- Morphing+Individual Pitch Control
- Geometric coupling +Individual Pitch Control
- Material coupling + Individual Pitch Control

The results of that study will be reported in D. 2.3.2 and the most promising concepts will be tested on wind tunnel proto-types.

